PASSIVE HAPTIC ROBOTIC ARM DESIGN

A THESIS SUBMITTED TO

THE GRADUATE SCHOOL OF NATURAL AND APPLIED SCIENCES
OF
MIDDLE EAST TECHNICAL UNIVERSITY

BY

SERTER YILMAZ

IN PARTIAL FULFILLMENT OF THE REQUIREMENTS
FOR
THE DEGREE OF MASTER OF SCIENCE
IN
MECHANICAL ENGINEERING

SEPTEMBER 2010

Approval of the thesis:

PASSIVE HAPTIC ROBOTIC ARM DESIGN

submitted by **SERTER YILMAZ** in partial fulfillment of the requirements for the degree of **Master of Science in Mechanical Engineering Department, Middle East Technical University** by,

Prof. Dr. Canan Özgen
Dean, Graduate School of **Natural and Applied Sciences**   _____

Prof. Dr. Süha Oral
Head of Department, **Mechanical Engineering**   _____

Asst. Prof. Dr. E. İlhan Konukseven
Supervisor, **Mechanical Engineering Dept., METU**   _____

Assoc. Prof. Dr. Hakan Gürocak
Co-Supervisor, **Mechanical Engineering Dept.,**
Washington State University Vancouver, USA   _____

Examining Committee Members:

Prof. Dr. Tuna Balkan
Mechanical Engineering Dept., METU   _____

Asst. Prof. Dr. E. İlhan Konukseven
Mechanical Engineering Dept., METU   _____

Prof. Dr. Kemal İder
Mechanical Engineering Dept., METU   _____

Asst. Prof. Dr. Buğra Koku
Mechanical Engineering Dept., METU   _____

Asst. Prof. Dr. Afşar Saranlı
Electrical and Electronics Engineering Dept., METU   _____

Date: 17.09.2010

I hereby declare that all information in this document has been obtained and presented in accordance with academic rules and ethical conduct. I also declare that, as required by these rules and conduct, I have fully cited and referenced all material and results that are not original to this work.

Name, Last name: Serter YILMAZ

Signature:

ABSTRACT

PASSIVE HAPTIC ROBOTIC ARM DESIGN

Yılmaz, Serter

M.S., Department of Mechanical Engineering

Supervisor: Asst. Prof. Dr. E. İlhan Konukseven

Co-Supervisor: Assoc. Prof. Dr. Hakan Gürocak

September 2010, 159 pages

The implant surgery replaces missing tooth to regain functionality and look of the normal tooth after dental operation. Improper placement of implant increases recuperation periods and reduces functionality. The aim of this thesis is to design a passive haptic robotic arm to guide dentist during the implant surgery.

In this thesis, the optimum design of the 6R passive haptic robotic arm is achieved. The methodology used in optimization problem involves minimization of end-effector side parasitic forces/torques while maximizing transparency of the haptic device. The transparency of haptic device is defined as realism of forces generated by device in real world compared to forces in virtual world. The multivariable objective function including dynamic equations of 6R robotic arm is derived and the constraints are determined using kinematic equations. The optimization problem is solved using SQP and GA. The link lengths and other relevant parameters along with the location of tool path are optimized. The end-effector parasitic torques/forces are significantly minimized. The results of two optimization techniques have proven to be nearly the same, thus a global optimum solution has been found in the search space. Main contribution of this study is to take spatial nonlinear dynamics into consideration to reduce parasitic torques.

Also, a mechanical brake is designed as a passive actuator. The mechanical brake includes a cone based braking system actuated by DC motor. Three different prototypes are manufactured to test performance of the mechanical brake. The final design indicates that the mechanical brake can be used as passive actuators.

Keywords: Dental implant surgery, optimum design of 6R robotic arm, transparency maximization, passive actuator, mechanical brake design.

ÖZ

PASİF HAPTİK ROBOT KOL TASARIMI

Yılmaz, Serter

Yüksek Lisans, Makine Mühendisliği Bölümü

Tez Yöneticisi: Yar. Doç. Dr. E. İlhan Konukseven

Ortak Tez Yöneticisi: Doç. Dr. Hakan Gürocak

Eylül 2010, 159 sayfa

Implant ameliyatı, hastaların eksik dişlerinin yerine aynı görünüşe ve fonksiyonelliğe sahip dişin eklenmesidir. Implantın yanlış yerleştirilmesi tedavi sürecinin uzamasına ve bazı fonksiyon bozukluklarına yolaçabilmektedir. Bu tezde amaç, implant operasyonu sırasında diş hekimine operasyon boyunca klavuzluk edebilecek pasif haptik robot kol tasarımı yapmaktır.

Bu tezde kapsamında, altı dönel eksenli robot kolunun en iyilenmiş tasarımı elde edilmiştir. En iyileme probleminde kullanılan yöntemde, haptik cihazın şeffalığı arttırılırken, robot kolun ucunda oluşan istenmeyen kuvvet ve torklar azaltılmıştır. Haptik cihazın şeffaflığı kısaca sanal ortamda yaratılan kuvvetlerin asıl ortamda hissedilirken ki gerçekliğidir. Çok değişkenli amaç fonksiyonu, uzaysal altı dönel eksenli robot dinamik denklemleri kullanılarak ifade edilmiş olup, sınırlar ise kinematik denklemlerden elde edilmiştir. En iyileme problemi SQP ve GA kullanılarak çözülmüştür. Çubuk uzunlukları ve çubuk uzunlukları ile ilişkilendirilen kütle ve atalet elemanları ile operasyon yolunun konumu da en iyilendirilmiştir. Robot kolun ucunda oluşan istenmeyen kuvvet ve torklar önemli ölçüde azaltılmıştır. Araştırma kapsamında, iki farklı en iyileme çözüm yolu kullanılmış ve sonuçlar birbirine çok yakın bulunmuştur. Bu da arama alanında en

iyilenmiş tasarımın bulunduğunu göstermektedir. Bu çalışmanın ana katkısı parazit torkları azaltmak için uzaysal dinamik denklemlerin lineerleştirilmeden kullanmasıdır.

Bu tez kapsamında ayrıca, haptik cihazlarda pasif eyleyici olarak kullanılmak üzere mekanik fren tasarımı yapılmıştır. Mekanik fren tasarımı, DC motor yardımıyla harekete geçirilen konik tabanlı fren sistemleri içermektedir. Üç farklı fren örneği üretilerek, performansı test edilmiştir. Yapılan en son tasarım, mekanik frenin pasif eyleyici olarak kullanılabileceğini göstermiştir.

Anahtar Kelimeler: Dental implant ameliyatı, altı dönel eksenli robotun en iyilendirilmiş tasarımı, şeffaflığın azamileştirilmesi, pasif eyleyici, mekanik fren tasarımı.

Dedicated to My family, who have always shown unconditional love and support at every single moment in my life…

ACKNOWLEDGEMENTS

TABLE OF CONTENTS

LIST OF FIGURES

FIGURES

LIST OF TABLES

TABLES

LIST OF SYMBOLS

a	Linear acceleration matrix
a_i	Effective link lengths
$\bar{a}_i$	Acceleration of the i_{th} link's origin
$\bar{a}_{ci}$	Acceleration of mass center of the i_{th} link
A_i	Auxiliary point
$\hat{C}$	Orientation matrix
$\hat{C}_{AB}$	Orientation matrix about $\overrightarrow{AB}$
d_i	Joint offsets
d_m	The mean diameter of the screw
$e^{\tilde{u}_i \theta_i}$	Exponential rotation matrix of joint variable i around unit vector $\vec{u}_i$
$\mathcal{F}_i$	Reference frame of the ith link
$\bar{F}^{(i)}$	Force acting on the mass center of the i_{th} link
$\vec{F}_{(i-1)i}$	Force acting on the proximal neighbor
$\vec{F}_{(i+1)i}$	Force acting on the distal neighbor
f_{tot}	Objective function
F_{act}	Activation force of the conical surface
F_{brake}	Force acting on braking pads
F_{user}	Force applied by the user
$\bar{g}^{(i)}$	Gravitational acceleration in the i_{th} frame
$\boldsymbol{g}(\theta)$	Gravitational force matrix in joint space
$\boldsymbol{G}$	Gravitational force matrix in Cartesian space
$\hat{J}_c^i$	Inertia tensor of the ith link
$\bar{J}_{ri}, \bar{J}_{ai}$	Components of the Jacobian matrix
$\hat{J}_p$	Jacobian matrix with respect to the tip point

$\dot{J}_p$	Time derivative of the Jacobian
L_{pad}	The contact length of the braking pads
$\bar{M}_c^i$	Moment acting on the mass center of the i_{th} link
$\vec{M}_{(i-1)i}$	Moment acting on the proximal neighbor
$\vec{M}_{(i+1)i}$	Moment acting on the distal neighbor
$\boldsymbol{m}(\theta)$	Mass matrix in joint space
$\mathbf{M}$	Mass matrix in Cartesian space
$m(l)$	Mass of the link
N_f	Number of the forces acting on the braking pads
N_p	Number of the braking pads
O_i	Origin of the $\mathcal{F}_i$
p	Applied pressure
p_{max}	Maximum pressure
$\vec{p}$	Position of the end-effector's tip point in vector form
$\bar{p}$	Position of the end-effector's tip point in matrix form
$\bar{P}_i$	Position of the i_{th} link origin's
$\bar{P}_{ci}$	Mass center position of the i_{th} link
P_{rise}	Force for rising the load by screw
$\vec{r}$	Position of the wrist point in vector form
$\bar{r}$	Position of the wrist point in matrix form
R_{pad}	Radius of the contact point to the hub
$\bar{T}_i$	Actuation torque of the i_{th} link
T	Torque produced by the braking pads
T_{screw}	Torque for rising the load by screw
$\vec{u}_1$	Unit vector along X axis
$\vec{u}_2$	Unit vector along Y axis
$\vec{u}_3$	Unit vector along Z axis
$\bar{u}_{1,}\bar{u}_{2,},\bar{u}_3$	Unit vectors in matrix form
$\bar{V}_i$	Velocity of the link origin of the i_{th} link

$\bar{V}_{ci}$	Velocity of the mass centers of the i_{th} link
$\boldsymbol{v}(\theta,\dot{\theta})$	Nonlinear velocity matrix
$\boldsymbol{V}$	Nonlinear velocity matrix in Cartesian Space
α_i	Twist angles
$\bar{\alpha}_i$	Angular acceleration of the i_{th} link
δ	Amount of worn
λ	Lead angle of the screw
μ_{brake}	The coefficient of friction at the braking surface
μ_{cone}	The coefficient of friction at the conical surface
μ_{screw}	The coefficient of friction at the screw
θ_i	Joint variables
$\ddot{\theta}$	Angular acceleration matrix
$\vec{\rho}'_i$	Vector from center of mass of the link to the proximal neighbor
$\vec{\rho}_i$	Vector from center of mass of the link to the distal neighbor
σ_i	Uncertainty coefficient
τ'	Torque matrix in joint space
τ	Torque matrix in Cartesian space
$\widehat{\Phi}_i$	Orientation of the links
ψ	Helix angle of the screw
$\bar{\omega}_i$	Angular velocity of the i_{th} link

LIST OF ABBREVIATIONS

CT   Computed Tomography

D-H   Denavit & Hartenberg

DMB   Developed Mechanical Brake

DOF   Degree of Freedom

ER   Electrorheological

FMB   First Mechanical Brake

GA   Genetic Algorithm

IAN   Inferior alveolar nerve

MR   Magnetorheological

MRI   Magnetic Resonance Imaging

SMB   Second Mechanical Brake

SQP   Sequential Quadratic Programming

CHAPTER 1

INTRODUCTION

In recent years, robotic surgery has been used widely in the surgical operations. It was first in 1985 that the PUMA 560 robotic arm successfully achieved the needle placing operation for brain biopsy through CT guidance [1]. Since then, further researches were conducted about the robotic surgery applications for different parts of the human body. After thousands of successful robot-assisted cases, it is concluded that surgical robotics will be the main assistant of the surgeons or even take the role of the surgeons in the future [2]. The developments in the robotic surgery have resulted in more precision, stability, and dexterity in robot-assisted surgical operations [3]. With the usage of computed tomography (CT) and magnetic resonance imaging (MRI) in the image guided systems, the accuracy of the operations has increased. The image guided systems also have brought new control algorithms and user interfaces for operation procedures that help the surgeon during the operation. In the remote surgery, robot is teleoperated by the surgeon sitting at a remote console at the one side of the operation room and controlling the motion of the robotic arms that acts on the patient at the surgical side. A very popular example of the remotely controlled robots is the "da Vinci system" which is commonly used at minimally invasive surgery, urology, and cardiology operations. In the da Vinci system, the surgeon does the operation via the master control handles using a stereoscopic visual display which helps the surgeon to see the movements of the slave instruments inside the patient's body [2, 4]. However; the robots in the surgical operation cannot be left alone during the operation as done in the industrial applications [1].

1
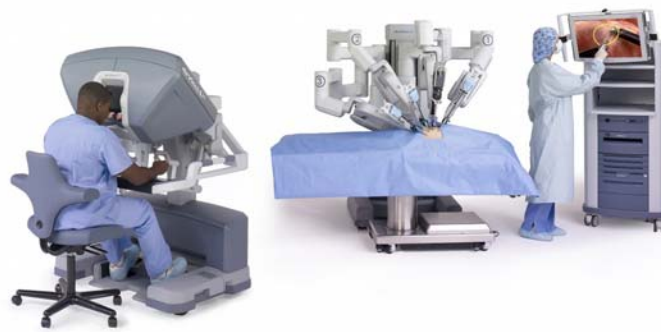
Figure 1.1: The da Vinci System [4]

1.1. MOTIVATION

In prosthetic dentistry, robot-assisted surgery has started to be used actively. Dental implants have become one of the application areas commonly used in prosthetic dentistry. Roughly, dental implant surgery replaces missing or damaged tooth with an artificial tooth root which functions like the real one. Dental implants are perfect choices for patients who lost their tooth as a result of an accident, unsuccessful periodontal treatment or any other causes. Dental implants allow patients to have a chance to gain the full functionality of the missing tooth like the natural one. Dental implants result to regain same natural-looking, feeling and functioning as the original tooth, hence they prevent the aesthetics problems of the patients occurred when they smile or speak. If the dental implant is placed by a specialized periodontist under proper conditions, the implant functions over a lifetime.
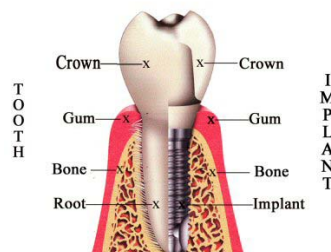
Figure 1.2: Anatomy of the Implant [5]

As shown in Figure 1.2, a natural tooth has root bonded to the jaw and crown placed on it. The dental implant, basically, replaces the root with an artificial one and then puts a prosthetic crown on it. To introduce an implant operation, some basic illustrations are demonstrated in the Figure 1.3.
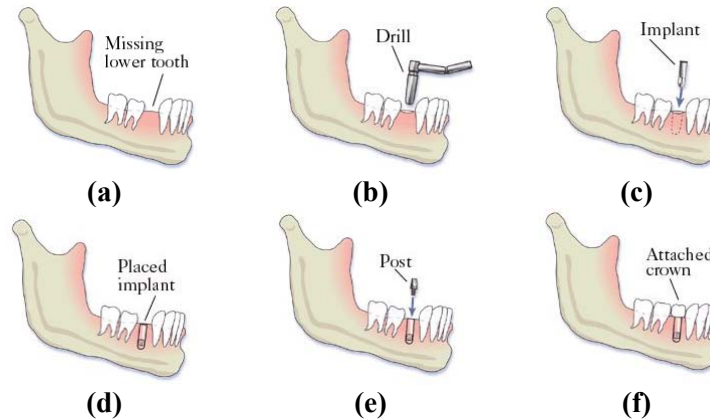
Figure 1.3: Steps of the Implant Procedure [6]

In the Figure 1.3 (a), patient with the missing tooth is prepared for implant operation. The candidate has to be healthy to overcome this procedure. The gum tissue covering the tooth is opened to drill the bone at the lower jaw (mandible) and to place the implant. Before starting to the operation the jaw structure of the patient has to be examined carefully. Once it is decided that the quality and quantity of the bone material is enough to place the implant, a special drill creates a hole on the bone as illustrated in the Figure 1.3 (b).

After drilling operation, the implant is placed to the hole to act as an artificial root and the gum tissue is sutured as in the Figure 1.3 (c) and (d). Following, providing the patient the missing tooth, the difficult part of the implant operation appears as healing process. About three to six months, the implant starts to become a part of the jaw and the bone bonds the implant which is called as osseointegration. After that, the gum tissue is opened one more time and a post is attached to the implant to support the new crown as in the Figure 1.3 (e). Before opening the gum tissue for

the first time, impressions are taken to produce the crown and to match with your existing teeth. Finally, the crown puts onto the post and looks like the natural tooth as in the Figure 1.3 (f) [6]. However, despite being easy to talk about the implant procedure; in fact it is a painful and bloody process as presented in the Figure 1.4.

Figure 1.4: Photo from the Implant Operation

Even though the implant operation is widely used throughout the world, failures and any other complications may arise. The proper applications of the implant operation result to biologically osseointegration with the bone and meet the prosthetic requirements, both functional and aesthetic [7]. In order to achieve a properly placed implant, position of the implant hole has to be determined carefully. The hole should not approach to the mandibular nerve in the lower jaw and scheiderian membrane of the maxillary sinus in the upper jaw. The improper placement of the implant causes an irreparable damage at mandibular nerve, including the inferior alveolar, mental and lingual nerves [8, 9]. A damage to the mandibular nerve results to permanent damage such as paresthesia of the gum, lip, and chin [10]. Also, the shape and resistance of the bone structure have to be investigated carefully [11]. The aesthetic replacement of the implant is an important issue to achieve the desired aesthetic effect. The implant cannot be placed to the appropriate position because of the insufficient bone thickness and this effect the crown placed on the top of the implant. This results to an improperly aligned crown and function disorders [12, 13].

4

In order to prevent complications of the implant operation, systems for the proper positioning of the implant are developed. Basic one among these systems is to use drill guides. Nevertheless, help of these fabricated templates is very limited. They do not give information about the anatomic structure of the bone and the thickness of the mucosa. Also, stabilization problems occur during the operation because of the production techniques [14]. To overcome these problems, templates based on volume image data are developed [15]. Being supported by the mucosa, tooth and bone, the developed templates increase the accuracy of the implant placed into the right position at the bone of the patient. Although using high production techniques, the drill guides can be manufactured after paying high costs and requirement of a new template for every change makes the drill templates not preferable [14,16].

Consequently, instead of drill guides, computer-assistance has been taken into consideration. The complex implant operation can also be achieved using computer-assisted imaging techniques [17, 18]. The developed system brings a new approach to the implant operation.

In this system, the surgical drill tool is tracked and animated on the radiological image of the surgical site. Infrared optical emitter is placed on trackable handpiece, marked with "a" in the Figure 1.5, and used to drill the implant hole. Also, the patient is equipped with an optical tracker, marked as "b" in the Figure 1.5 which continuously projects the position of the patient and the progress of the drilling. Thus, the position of the handpiece can be controlled [18].
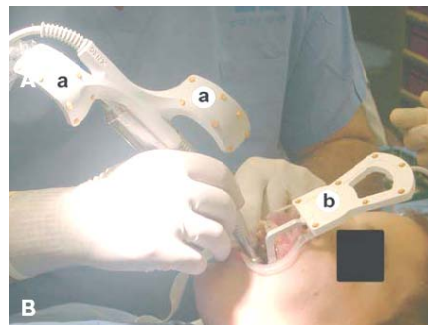
Figure 1.5: Image Guided Implantology [18]

The usage of image-guidance systems increases the safety of the operation [19-22]. However, there are still problems about the accuracy, positioning and angulations; despite the image guidance systems are used. The desired implant hole should be at least 2 mm away from the inferior alveolar nerve (IAN) and the jaw bone. The misalignment between the desired and the actual hole has to be less than 0.3 mm. The desired system must have an accuracy of at least 0.5 mm. Yet, on average the image guided systems provide 0.9 mm accuracy [23]. Thus, the operation is still up to the experience of the dentist.

The first active robot system, "OTTO" is developed to be used in maxillofacial surgery. The robot achieves the interactively programmed tasks under the control of the surgeon [24]. A haptic device is also used in the bone drilling operation "virtually". The system has been designed by Kusumoto et. al. and uses a PHANTOM Haptic Device [25] to acquire force feedback during the oral implant surgery [26]. The system is design to be used in the education of the training of the dental surgeons.

1.2. THE PROPOSED SYSTEM

Due to the problems occurred in the implant operation, a low cost surgical aid system which guides the surgeon especially during the complex implant operation is aimed to be designed. The system, as shown in the Figure 1.7, consists of 4 main parts. A tracking system which would track the surgeon's hand-piece and the patient, a graphical user interface which provides visual feedback to the surgeon, a control software which controls the overall operation and supplies the surgeon haptic feedback in real time, and a passive haptic robotic arm which is moved by surgeon guiding him during the operation for accurately positioning of the implant hole. The working schema is demonstrated in the Figure 1.6.
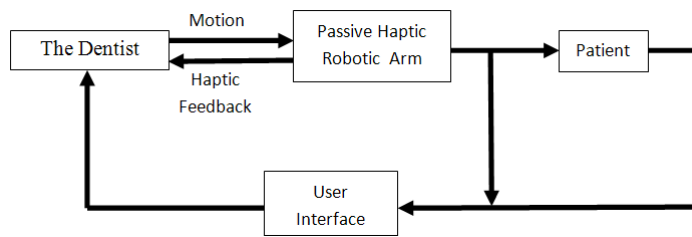
Figure 1.6: Working Schema of the Proposed System
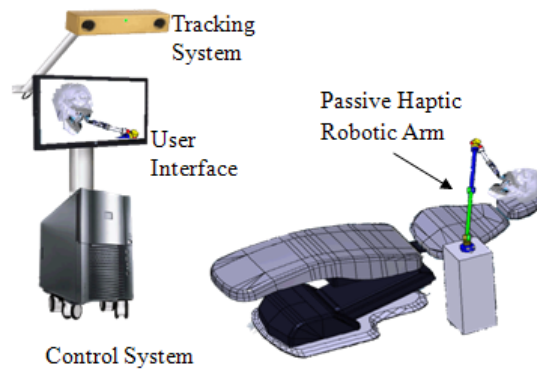
Figure 1.7: The Proposed System

The guidance in the proposed system can be explained by giving information about the actuation system. In general, most robots with active feedback can reach to the desired position using given programmed task. On the other hand, passive feedback only restricts the motion of the manipulator given by the user. Basically, the proposed system works like that: At first, the position of the desired implant hole is given to the control system. Then, the dentist takes the robotic arm, on which the drilling tool is attached, and moves it towards the target hole from the initial position. During the process the control system checks whether the dentist is getting closer to the target position or not. Moreover, when the tip point of the robotic arm enters into the range of the control system, it forces the dentist to reach to target position with correct angulation by supplying passive feedback. The passive brakes at the joints of the robotic arm work simultaneously and provide different braking torques to the joints helping the dentist to locate the implant hole accurately. When

the dentist reaches to desired implant hole, the control system regulates the braking torques and let the dentist do the drilling operation without losing the position of the hole. The control system also checks the depth of the implant hole in real time and when the desired depth is reached, it locks the robotic arm by supplying maximum torque to the passive brakes. As a result, the complications arising from drilling of IAN and misalignment of the hole can be prevented.

Taking into consideration the usage of haptic feedback in the guidance of the surgeon reduces the dependence on the surgeon's skills and experience for accurate implant positioning and improves the overall safety of the implant procedure. The main goal of our research team is to develop the passive haptic robotic arm as part of the dental surgical aid system. This research also explores the design of a passive haptic interface by employing mechanical brakes to be used as actuators in the robot.

In this thesis, the passive haptic robotic arm is going to be designed. The kinematic parameters of the passive haptic robot are going to be optimized using the appropriate objective function to achieve the implant hole drilling operation. The objective function is derived from the dynamic equations which are torques and forces in the Cartesian space. The aim of the optimization process is to obtain utmost lightweight mechanism with maximum transparency while consuming minimum energy [27]. The transparency is an important parameter for the haptic devices. The quality of the haptic devices is decided due to their transparency characteristics [28]. In this thesis, a methodology introduced to optimize the kinematic parameters of the passive haptic robotic arm mainly determines the optimum link lengths and other parameters associated with link lengths including mass and inertia elements. The presented methodology finds the maximum transparency as seen from the user side along the implant operation path after the optimization process. The methodology allows determination of the optimum link lengths together with the tool path. Finally, the optimization problem is aimed to be

solved by using Sequential Quadratic Programming (SQP) and Genetic Algorithms (GA).

After the optimization process, a mechanical brake is introduced to be used in the actuation of the passive haptic robotic arm to supply necessary braking torques to the joints. The design, calculations and development of the mechanical brake is achieved and the brake itself is produced to test whether it is applicable to be used as a passive actuator or not.

1.3. OUTLINE OF THE THESIS

In the chapter 2, the literature survey is given to discuss the optimum design problem of the passive haptic robotic arm.

In the chapter 3, the kinematics and dynamics of the passive haptic robotic arm is explored and a path is generated to simulate a simple implant operation. After that the objective function to maximize the transparency is determined. Jacobian and its time derivative are developed to transfer the joint torques to the Cartesian Space. The objective function is put into the MATLAB's Optimization Toolbox and using the mentioned optimization algorithms, the kinematic parameters of the passive haptic robotic arm are computed. The results are presented and discussed.

In the chapter 4, design of a mechanical brake is introduced. First, the information about actuators used in the robotic systems is given and afterward the active and passive actuation systems are discussed. The examples of the passive actuation are explored and subsequently the design of the mechanical brake is achieved. The calculations and working principle are given in detail while the developments and the experimental results are presented as well.

In chapter 5, discussion, conclusion and future work are given.

CHAPTER 2

LITERATURE SURVEY

The designing stage of a robotic manipulator starts with decision of number of the links and the types of the joints (revolute, prismatic etc.). After that the dimensioning the links becomes to correspond the performance requirements. The lengths of the links determine the workspace volume and shape of the robotic manipulator. In spite of the developments in the robot kinematics area, a methodology to determine length of the links of a manipulator is still not available. Not taking into consideration the shape of the links at first, the determination of the dimensions of the manipulator links is still confusing. Recently it has become popular to express the different design aspects using formulations to generate optimization problems which can be solved by using well-developed optimization algorithms in the commercial software packages.

Vijaykumar et. al. suggests determining the orientation structure of a six-degrees of freedom manipulator using straightforward geometric arguments. They use the spherical counterpart of the Grashof's theorem to show that the orientation structure has an optimum geometry. Two different methods are proposed. One of them is "the concept of the dexterous workspace, which is a portion of the workspace within which the hand can assume any orientation" and the other is "to trace the portion of the workspace within which the hand can assume a specified orientation". The formulation used includes the geometric conditions for the existence of a dexterous workspace. It is obtained that for an optimal geometry, the singularities can be eliminated with a slight reduction at motion ranges of the joints [29].

Paden et. al. states in their study that there is a close relationship between the kinematic performance and design of 6R manipulators. Moreover, they have developed the notions which are length of a manipulator, work-volume, maximal work-volume, well-connected workspace, and kinematic inverse. They also define the optimality condition for a manipulator as having maximal work-volume and well-connected workspace. Thus, using these defined notions, they conclude that a 6R manipulator can only reach to the maximal work-volume and well-connected workspace, if the inverse kinematic is same as an elbow manipulator [30].

The design of the workspace of a manipulator has great importance in the dimensioning of the link lengths. Bergamaschi et. al. have formulated an optimization problem to establish the optimal geometric parameters of the manipulator. The objective is to maximize the working volume where the constraint is taken as the regular boundary of the workspace. The optimization problem has been solved using sequential minimization techniques [31]. Furthermore, they also have tried to solve the optimization problem using different optimization techniques which includes sequential quadratic programming, genetic algorithms, differential evolution and particle swarm optimization. Finally, they stated that the SQP is faster than the other three metaheuristic techniques which cannot compete with SQP in the consumed computational time. It has also been observed that SQP is more sensitive to the initial values rather than the other techniques. Regarding the computational time, metaheuristic techniques supply good solutions, despite the existence of many local optimum solutions in the search space. At the end, they have offered that SQP can be combined with the metaheuristic techniques to obtain a final solution [32].

Ceccarelli et. al. have stated that the workspace requirements have to be analyzed carefully in the designing stage of the manipulators which are evaluated due to their workspace capabilities. Following, they have formulated a multi-objective optimization problem by taking the workspace volume and robot dimensions as the objective functions where the workspace limits are taken as constraints. The

optimization problem is solved to obtain maximum workspace of a 3R manipulator [33].

Later on, Ceccarelli et. al. has extended the research for an optimum design of the serial and parallel manipulators. They have taken basic characteristics of manipulation purposes into consideration which are workspace, stiffness and singularities. Thus, a multi-objective optimization problem is constructed with an objective function employing the position and orientation of the workspace, the Jacobian matrix, and linear and angular compliant displacements. The Jacobian matrix is taken into the objective function to identify the singularities. The linear and angular compliant displacements are chosen to evaluate the static behavior of the manipulator. Numerical examples are conducted on a 3 DOF parallel manipulator and a 6R serial manipulator. The optimization problem is solved using SQP algorithm in the MATLAB Optimization Toolbox. Due to the complexity of the design algorithm it takes longer computational times. Finally, they have reported that the numerical results are satisfactory for the proposed design [34].

Another important point at the design of the robotic manipulator is the determination of the base location. In order to achieve the given tasks, the manipulator has to be placed to the correct location. Mitsi et. al. have worked on the optimal placement of the robot base to acquire the given tasks. They have proposed a new formulation to form a multi-objective optimization problem using the prescribed end-effector positions. The aim of the objective function is to maximize the manipulability while considering the joint limits. They have combined a genetic algorithm with a hill climbing method and a constraint handling method. The aim of this combination has been set to eliminate the disadvantages of each method and to utilize from the advantages. The proposed algorithm is used at the six cases of a 6-DOF manipulator. The results have shown that the proposed algorithm gives better results than the simple GA. Finally, they have reported that the manipulability greatly increases when the optimal placement of the robot base location is computed [35].

The energy performance is also an important criterion at the designing stage of any mechanical device especially for the robot manipulators. The energy consumption affects the selection of the actuators and may result to large actuators to be used. The optimization of link masses and inertias decreases the torques at the joints of a manipulator and improves the energy consumption. Kucuk et. al. have optimized the link masses of a manipulator with three links to acquire minimum energy consumption. They have derived the dynamic equations using energy based method which is Lagrange-Euler. A trajectory is generated by using a 5th order polynomial. The time derivatives of the trajectory are used for determination of the velocity and acceleration. Omitting the Coriolis, centrifugal and gravitational effects from the dynamic equations of the manipulator, they only have minimized the inertia matrix using GA. By changing the parameters of GA, they have tried to find best optimum link masses. The optimum link masses have been determined by checking the values of the kinetic energy. Finally, it has been concluded that, the link masses are important parameters for energy consumption of a manipulator. Moreover, the effects of the GA parameters on the mass optimization also have been analyzed. At the end, GA has been reported to be an exceptionally appropriate optimization technique at the design of the robotic manipulators [36].

Millman et. al. have extended the research of torque consumption to the force-reflecting devices. They have determined the performance features of a force-reflecting device as low inertia, low friction, high stiffness, backdriveabilitiy, high output force capabilities, multi degrees of freedom, and the sizeable range of motion. They have designed a four degree of freedom device to acquire the above features. They have defined a force/torque workspace within which the desired endpoint torques and forces have to be supplied using actuators with limited output. The kinematic parameters have been decided after evaluating 500 designs at which the actuator torques have been calculated to overcome the torque requirements of endpoint loads within the specified operation volume. The final design, consequently, meets the requirements with the minimum actuator and mechanism size [37].

Khatib et. al. have investigated the dynamic performance of a parallel mechanism to choose the design parameters efficiently. They have evaluated the dynamic performance of a manipulator by using the inertial and acceleration properties of the end-effector. First, they have formed models for characterization of the inertial and acceleration properties. Later, they have obtained the objective function to minimize the norms and condition numbers of the mass, inertia, and the acceleration characteristics. They have reported the results that indicate the inertial properties are improved significantly but the acceleration capability is reduced for better mass properties [38].

Papakostas et. al. have developed a technique to obtain a dynamically optimal robotic manipulator. The task-based technique has been used to optimize the dynamic performance using GA. They have emphasized the importance of the inertial properties in the dynamic behavior of the manipulators. They have indicated that using a suitable objective function the inertia-induced forces and torques have to be minimized. The objective function has been chosen as the mean-squared values of the forces and moments acting to the ground while the manipulator is moving over a trajectory. They have applied the dynamic optimization procedure to a planar R-R manipulator. They have acquired significant improvements for the forces and moments acting on the ground. They also have mentioned about the important of the constraint in the optimization procedure. The choice of the constraints affects results of the optimization problem and so as the design process [39].

Vlachos et. al. have designed a haptic device to be used at the training of the urological operations. The haptic device consists of 2 DOF, 5-bar linkage and 3 DOF spherical joint. The device applies small forces and moments in the virtual environment using five active actuators which are mounted to base and the motion is transferred using capstan drives. At first, they have mentioned about the designing process and implementation of the 5 DOF haptic device [40-42]. The implementation of the haptic device has been completed and successful results have

been obtained at applications in the virtual environment. After that, they worked on optimization of the haptic device. In 2004, they formed a multi-objective objective function to minimize the mass, inertia and joint friction. They optimized the haptic device along an operation path rather than a workspace. The objective functions were formed using the mass/inertia properties and joint frictions. They have taken the kinematic and operational constraints into consideration and using the MATLAB Optimization Toolbox, the multi-objective optimization problem is solved. The optimization results reduced the lengths of the links and diagonal terms of the mass matrix [43]. Furthermore, they advanced their research to the minimization of the forces and torques as seen from the user side and declare that the user has to feel the forces generated in the virtual environment. Therefore, the haptic device has to reflect these forces to the user as transparent as possible. By transparency it is concluded that the user only feels the appropriate forces/torques but nothing else. Thus, the mechanism induced parasitic torques and forces have to be minimized. They have developed an objective function including mass/inertia properties of the haptic device as seen from the user side. The results show that a significant improvement is obtained with respect to their previous designs [44].

Finally, Vlachos has presented a methodology to maximize the transparency of the haptic devices. The methodology does not only optimize the dimensions of the mechanism, but also the all relevant design parameters including the position of the end point relative to the path location. The dynamic equations for the mechanism have been derived using LE method. Then using the Jacobian matrix, the dynamic equations have been transferred to the user side. The objective function includes the norm of the parasitic forces and torques at the user side. The objective function has been calculated over the operation path. Using the kinematic and operational constraints, the optimization problem has been solved by the MATLAB Optimization Toolbox. They have reported that the dimensions of the mechanism are reduced by 60% relative to the existing designs. Using the results, they have constructed a new 5-DOF haptic device and stated that an important improvement is achieved [28].

In this thesis, the methodology developed by the Vlachos is applied to the design of a passive haptic robotic arm with six revolute joints. The main contribution in this part of the study is that the proposed robotic arm is working in spatial coordinates instead of the one developed by Vlachos which is operating in XY coordinates. The aim is to optimize the kinematic parameters of the passive haptic robotic arm while maximizing the transparency which indicates the reality of the feeling when touching the virtual objects in the virtual environment. Using the developed methodology, the link dimensions together with mass and inertia elements, which can parameterized by the link lengths, are optimized. Also, it is aimed that the location of the implant operation path with respect to the base position has to be optimized to achieve the energy consumption requirements. In the solution of the optimization problem two different algorithms are used which are SQP and GA. These algorithms use different techniques to solve the optimization problems. Thus, due to the results of the optimization process, it is observed whether the global optimum solution found in the search space or not.

CHAPTER 3

OPTIMUM DESIGN OF 6R ROBOTIC ARM

3.1. INTRODUCTION

One of the goals of this research is to determine the link lengths of a passive haptic robotic arm using appropriate objective functions to maximize transparency of the robotic arm. The transparency of a haptic device can roughly be summarized as the reliability of the operators' feelings at the virtual environment when using the haptic robotic arm. The transparency of the passive haptic robotic arm is very important issue since haptic devices are qualified in accordance with their transparency characteristics. The optimization methodology used in this study aims to optimize the link lengths of the robot arm and the location of the tool path. In accordance, the methodology is also aimed to maximize haptic device transparency as felt by the user side using an objective function which includes end-effector parasitic torques/forces during its motion, such as mass/inertia, gravitational forces, and friction [28]. A lightweight mechanism is obtained with maximum transparency while consuming minimum energy after optimization procedure. To maximize the transparency of the haptic device, an objective function based on spatial dynamic equations is needed to be developed. Necessary constraints to solve the optimization problem are obtained by using kinematic equations derived from Denavit & Hartenberg (D-H) convention.

In order to manipulate a robotic arm in space, kinematic equations are required to determine the end-effector's position and orientation using a set of mathematical expression. Using the kinematics of the manipulators, the position of the

17

manipulator can be described and using the derivatives of the kinematic equations the velocity and acceleration of the robotic arm can be defined. After obtaining position and orientation of the end effector, computation of the joint variables become the main concern of the inverse kinematics [46].

In this chapter, first forward and inverse kinematics of the proposed robotic arm is presented. A sample path is generated using the kinematic expression that simulates the implant operation and it is used in the optimization problem. After presentation of kinematic equations and the path, the necessary objective functions are developed. The objective function includes dynamic equations which are torques and forces acting to the end effector in the Cartesian space; hence dynamics equations have to be derived. Then, using dynamics equations, objective function is defined and the constraints are determined through kinematic equations. The optimization problem is solved using SQP and GA. Finally, application of the methodology, solutions, and performance of these optimization techniques are discussed and presented.

3.2. KINEMATICS OF THE PASSIVE HAPTIC ROBOTIC ARM

Passive haptic robotic arm configuration is selected as Unimation PUMA 560, which has six degrees of freedom with rotary joints, to overcome necessary design considerations. With the help of the six degrees of freedom, a desired position can be reached in any orientation. Thus, to accurately locate the position of the implant hole under the guidance of the passive haptic robot, the robotic arm has to approach to the position of the target hole in any orientation. Unimation PUMA 560's kinematic structure can easily be defined and inverse kinematic solution can be calculated algebraically [46]. The links and the joints of the PUMA are illustrated in the Figure 3.1. In PUMA 560, as in many other industrial robots, the last three joint axes, intersect at a common point like a spherical wrist, and this point of intersection is coincident with the origin of frames 4, 5, and 6 [46]. This geometry helps us to analyze the inverse kinematics of the robotic arm. Furthermore, using the kinematic model of the PUMA 560 robot arm, the position and orientation of

the haptic robotic arm can easily be defined with forward kinematics. Inverse kinematic equations calculate the necessary joint variables in any given position and orientation of the hand tool.
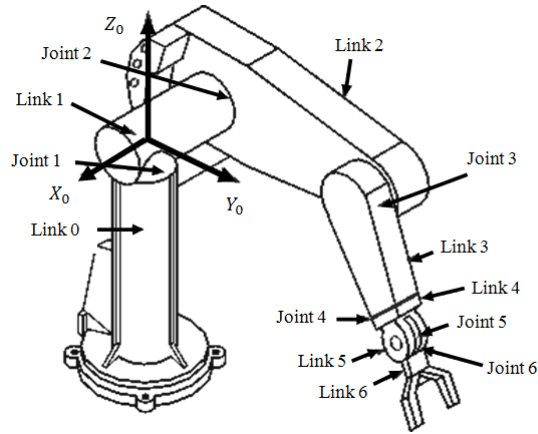
Figure 3.1: PUMA 560 Manipulator

3.2.1.FORWARD KINEMATICS OF THE ROBOTIC ARM

The exponential rotation matrices are used to express kinematic equations due to their simplicity [48 - 50].The frames are attached to the links and the joint and link parameters are determined due to D-H convention. All parameters are listed in the Table 3.1. The kinematic model of the passive haptic robotic arm including the frame attachments with link parameters are given in the Figure 3.2 where α_i, θ_i, d_i, a_i represent the twist angles, the joint variables, the link offsets, and the effective link lengths, respectively.

19
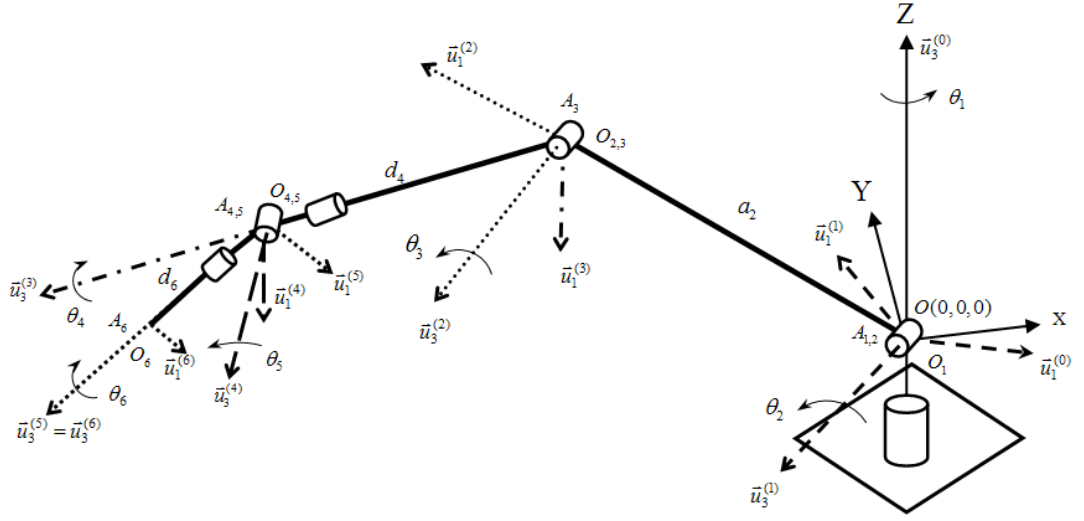
Figure 3.2: 6R Robotic Arm with Kinematic Model

Using rotation matrices for six links, the orientation of the tip point with respect to the base frame is given as,

$$\hat{C}^{(0,6)} = e^{\tilde{u}_3 \theta_1} e^{\tilde{u}_2 \theta_{23}} e^{\tilde{u}_3 \theta_4} e^{\tilde{u}_2 \theta_5} e^{\tilde{u}_3 \theta_6} \qquad (3.1)$$

The position of the end-effector's tip point can be expressed as,

$$\vec{p} = a_2 \vec{u}_1^{(2)} + d_4 \vec{u}_3^{(3)} + d_6 \vec{u}_1^{(6)} \qquad (3.2a)$$

The position of the wrist point can be expressed in vector from as,

$$\vec{r} = a_2 \vec{u}_1^{(2)} + d_4 \vec{u}_3^{(3)} \qquad (3.2b)$$

Finally, the position and orientation of the end-effector is obtained in the terms of the joint variables using forward kinematic equations based on D-H convention. The details of the calculation of the forward kinematics are given in the Appendix A.1.

20

Table 3.1: Kinematic Parameters of 6R Robotic Arm

i^{th} link	α_i	a_i	d_i	θ_i
1	$-\pi/2$	0	0	θ_1
2	0	a_2	d_2	θ_2
3	$\pi/2$	0	0	θ_3
4	$-\pi/2$	0	d_4	θ_4
5	$\pi/2$	0	0	θ_5
6	0	0	d_6	θ_6

3.2.2.INVERSE KINEMATICS OF THE ROBOTIC ARM

Forward kinematics enables to determine the position and orientation of the end-effector with respect to base frame in the Cartesian coordinates using given joint variables. In order to reach a goal position which has specified position and orientation values, joint variables can be determined using inverse kinematic equations. Using the position and orientation matrix of the end-effector, analytical inverse kinematic solution of the 6R can be calculated easily. For a 6R robotic arm with a spherical wrist, the first three degrees of freedom determines the positioning stage of the wrist and the last three degrees of freedom where intersect at a common point determines the orientation of the wrist [46, 51]. The derivation of the inverse kinematics equations is given in the Appendix A.2. The calculation of the joint variables and illustrations of the singularities are discussed in detail.

Up to now, forward kinematic equations are represented, then for the given orientation and position matrices, the derivation of the joint variables using inverse kinematic equations is achieved. Using MATLAB®, the kinematic equations are verified. The position and orientation of the wrist point are computed using forward kinematics. Then the calculated position and orientation matrices are put into inverse kinematic equations and the joint variables are calculated reversely as the

given ones. In order to avoid singularities, critical values of the joint variables are taken into consideration in the MATLAB program. Therefore while moving within the workspace, if manipulator reaches to a point that requires a change in the arm configuration, the program stops and warns the user about singularity error. In the Appendix B, some case studies are performed in order to show the behavior of the MATLAB program when the robotic arm enters to a singular position.

In order to verify the kinematic equations a graphical study is also presented. In order to simulate the 6R robotic arm in the virtual environment, a simple robotic arm is constructed using bodies in the SimMechanics® software, a mechanical simulation program which is a part of Simulink®. In the model, lines represent the links. Link parameters are identified by means of the D-H convention into the SimMechanics blocks. Link lengths and link orientations are defined in the blocks and mass and inertia of the links are set. Links are connected using revolute joints. To actuate the joints necessary variables such as position and velocity are defined. Appropriate sensors are placed to measure position and orientation of the links especially of the wrist and tip points. The model formed using SimMechanics is given in the Figure 3.3.
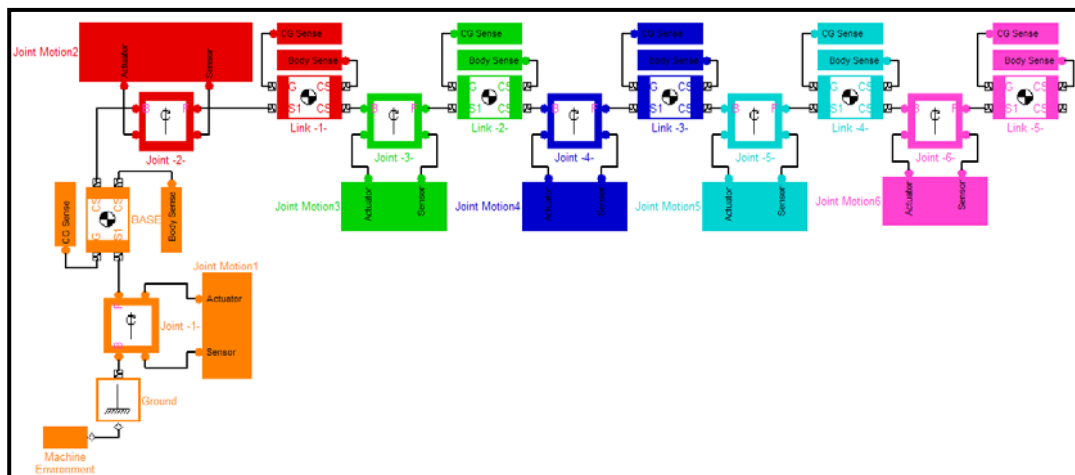
Figure 3.3: SimMechanics Model for 6R Robotic Arm

Taking the link lengths, link offsets and joint variables as given below, the model demonstrate the manipulator as in the Figure 3.4.

$$a_2 = 0.5\ m,\ d_2 = 0,\ d_4 = 0.4\ m,\ d_6 = 0.3\ m,$$
$$\theta_1 = 0,\ \theta_2 = 0,\ \theta_3 = 0,\ \theta_4 = 0,\ \theta_5 = 0,\ \theta_6 = 0.$$

In the Figure 3.4, green line represents the "a_2" parameter, blue line represents the "d_4" parameter and yellow line represents the "d_6" parameter. Of course, due to the singularity, θ_5 is not taken zero, but to show the initial position of the manipulator, it is taken close to the zero as an initial condition.
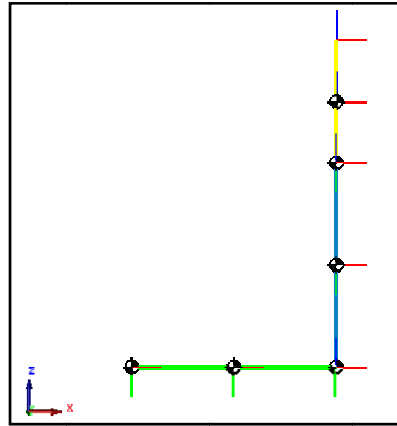
Figure 3.4: Illustration of 6R Robotic Arm with Given Parameters

Kinematic equations are verified using both MATLAB programs and SimMechanics model. For the given link lengths, joint offsets and joint variables position and orientation of the wrist and tip point are calculated and then using them reversely, joint variables are computed. In the Appendix B.1, the verification of the kinematic equations is presented.

3.3. THE PATH GENERATION

The proposed haptic device in this study is planned to use in dental implant surgery. In order to reach any tooth in the mouth of the patient in any orientation, a 6R

robotic arm is chosen, providing the dentist to accomplish the drilling operation for any tooth. First three degrees of freedom is used for positioning and the orientation of the drilling tool is set using the last three degrees of freedom. In a dental implant operation, the dentist first reaches to the target tooth, and then starts to drilling operation. Here, as mentioned previously, drilling is the most important process of the implant operation. The dentist has to drill very carefully to avoid implant complications. The drilling tool has to be perpendicular relative to the upper surface of the tooth. Also, the dentist is able to reach to the target tooth either from right and left side. In the light of this information, a simple dental implant operation can be summarized as follows; first the dentist reaches to the tooth, starts to drilling operation while turns the drilling tool from right side to left side. In order to design a haptic robotic arm which is used in dental implant operations, the dentists are observed during the real implant operations and many videos about dental implantology have been watched. Consequently, in accordance with the help of the dentists, the required operation path has been determined.

In the lights of the ideas of the dentist, a CAD model is constituted to demonstrate the dental implant operation using Solidworks®. The CAD model was built based upon the typical dimensions of a dentist chair while the patient is modeled as a skull head as shown in the Figure 3.5.
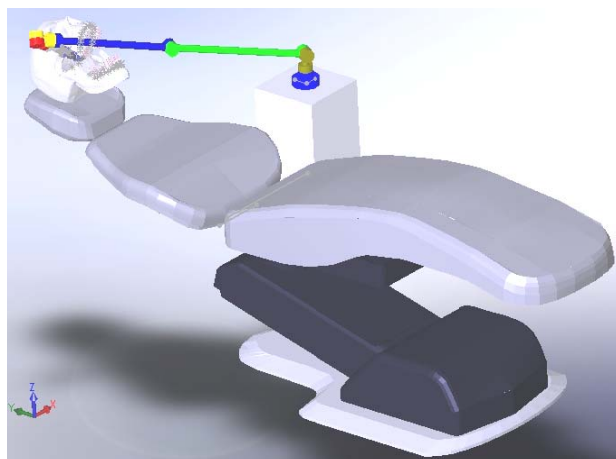
Figure 3.5: Demonstration of Dental Implant Operation

A simple 6R robotic arm is constructed using the circular bars and joints are added to links. The manipulator's tip point is extended to the furthest tooth in the mouth to obtain the position and orientation of the manipulator's wrist point. In the Figure 3.6, the manipulator is shown with the rotation axes of joints. Reference frames are also attached to the joints but they are not shown in the figure to avoid the complexity of the figure.
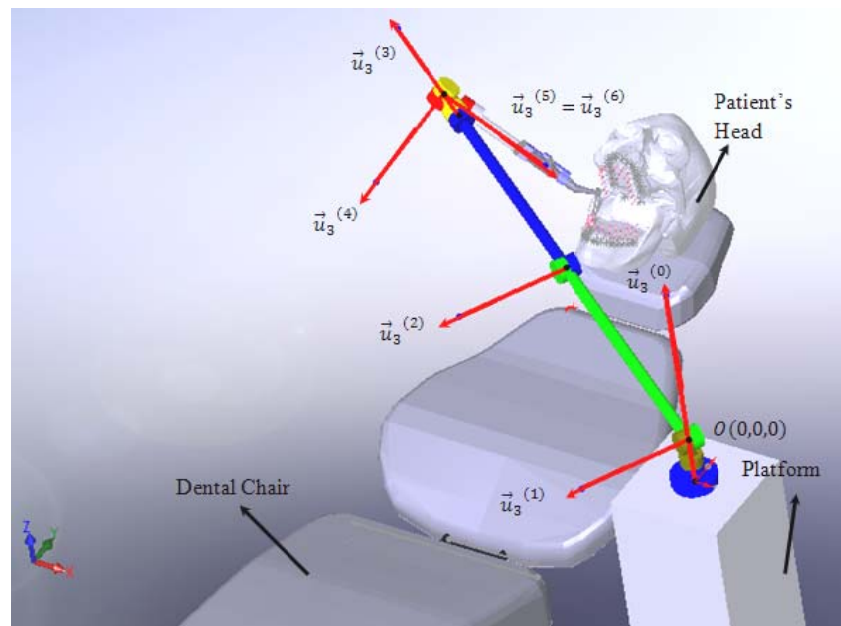
Figure 3.6: The CAD Model with Rotation Axes

Now, the position and orientation of the wrist point of the manipulator is obtained from the generated CAD model. In the Figure 3.7, the points are placed to indicate the position of the lines with respect to base frame. Using vector calculations, starting from the tip point of the manipulator, one can reach to the wrist point's position.

25
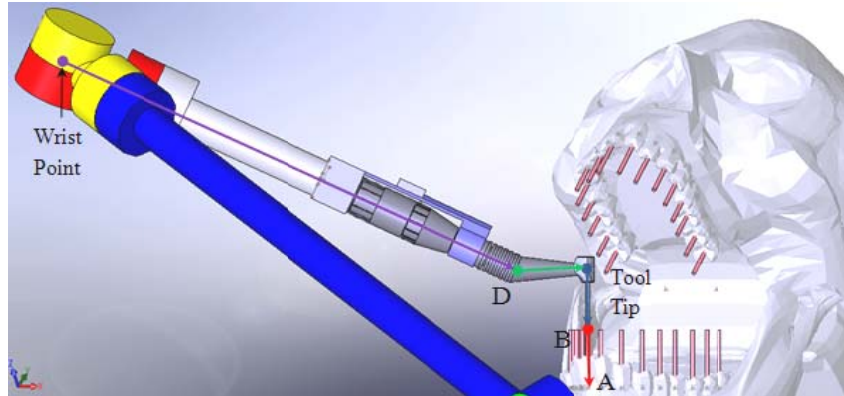
Figure 3.7: Vectors for Wrist Point Calculations

Taking the coordinates of the points A and B from the constructed CAD model and using the specified length of the dental operation tool, the coordinates of the wrist point can be calculated. In the Figure 3.8 and Figure 3.9, the position of the wrist point is calculated starting from tip point's position and then proved by checking the coordinates of the wrist point taken from the CAD model. There is also an offset at the origin and this is taken into consideration and necessary points are revised due to this offset. The vectors are given in the matrix form where first three rows represent the coordinates of the vector and the last row represents the length of the vector.

```
The coordinates of points taken from CAD model
PNT_A =
        -422.1        414.57        102.67
PNT_B =
        -422.08       397.38        76.88
PNT_Tool_Tip =
        -422.11       432.32        129.3
PNT_D =
        -456.76       417.43        139.21
PNT_W =
        -669.54       387.94        292.92
PNT_Org =
        0      0      90
The calculated of vectors
vector_AB =
    0.00064529
       -0.55463
       -0.8321
        30.994
```

Figure 3.8: Calculation of the Coordinates of the Wrist Point (Con'd)

```
vector_A_Tool_Tip =
    0.00031247
      -0.55463
       -0.8321
        32.003
vector_Tool_Tip_D_Ref =
        0.8886
        0.38185
       -0.25414
        38.994
The calculated of points using the vectors
PNT_Tool_Tip_New =
       -422.11
        432.32
          39.3
PNT_D_New =
       -456.76
        417.43
         49.21
x =
          0
The coordinates of the wrist point
POS_vec =
       -669.54
        387.94
        202.92
****************************************************************
```

Figure 3.9: Calculation of the Coordinates of the Wrist Point

"*PNT_W*" represents the coordinates of the wrist point which is taken from the CAD model and "*POS_vec*" shows the calculated coordinates of the wrist point and both are the same. All units in the calculations are in the unit of "*mm*".

To calculate the necessary orientation matrix, direction cosine matrix is used. The *cosine* of the angles between the frame of the wrist point and the base frame is computed and put into 3x3 matrix form as,

$$\hat{C}^{(a,b)} = \begin{bmatrix} C_{11}^{(a,b)} & C_{12}^{(a,b)} & C_{13}^{(a,b)} \\ C_{21}^{(a,b)} & C_{22}^{(a,b)} & C_{23}^{(a,b)} \\ C_{31}^{(a,b)} & C_{32}^{(a,b)} & C_{33}^{(a,b)} \end{bmatrix} \tag{3.3}$$

where

$$\hat{C}_{ij}^{(a,b)} = \cos \theta_{ij} \tag{3.4}$$

27

The position and orientation of the wrist point is acquired using the CAD model. Using the kinematic equations derived previously, the joint variables can be computed to reach to this position. In order to use the kinematic equations, link lengths and link offsets also have to be determined. They can be measured from the CAD model using the frames attached to links. The measured links lengths are,

$$a_2 = 0.4\ m, d_2 = 0, d_4 = 0.4\ m, d_6 = 0.26414\ m$$

```
TRANSFORMATION_MATRIX =
      -0.58558      -0.090497       0.80555       -669.54
             0        0.99375       0.11164        387.94
      -0.81061       0.065374      -0.58192        202.92
             0              0             0             1
JOINT_VARIABLES =
        149.91         -14.21        89.032        -51.802        140.45        115.76
TRANS_MAT_CALC =
      -0.58558      -0.090497       0.80555       -669.54
     7.8534e-010      0.99375       0.11164        387.94
      -0.81061       0.065374      -0.58192        202.92
             0              0             0             1
*************************************************************
```

Figure 3.10: Calculation of the Joint Variables for Given Position of the Wrist

The orientation and the position of the wrist point are put in the MATLAB program and the output of the program is shown in the Figure 3.10. Using the kinematic equations, the joint variables of the manipulator are computed. First, the position is acquired using the vector computations and the orientation of the wrist point is calculated using equation 3.3. They put all together in a transformation matrix. Then, they are given into the inverse kinematic equations; hence the joint variables are determined. After that, the computed joint variables are put into forward kinematic equations and the given transformation matrix is obtained. In order to prove the correctness of the joint variables, the values of the angles is checked from the CAD model, measuring the angles by using the attached coordinate frames. In the Figure 3.11, the CAD model shows the values of six angles.
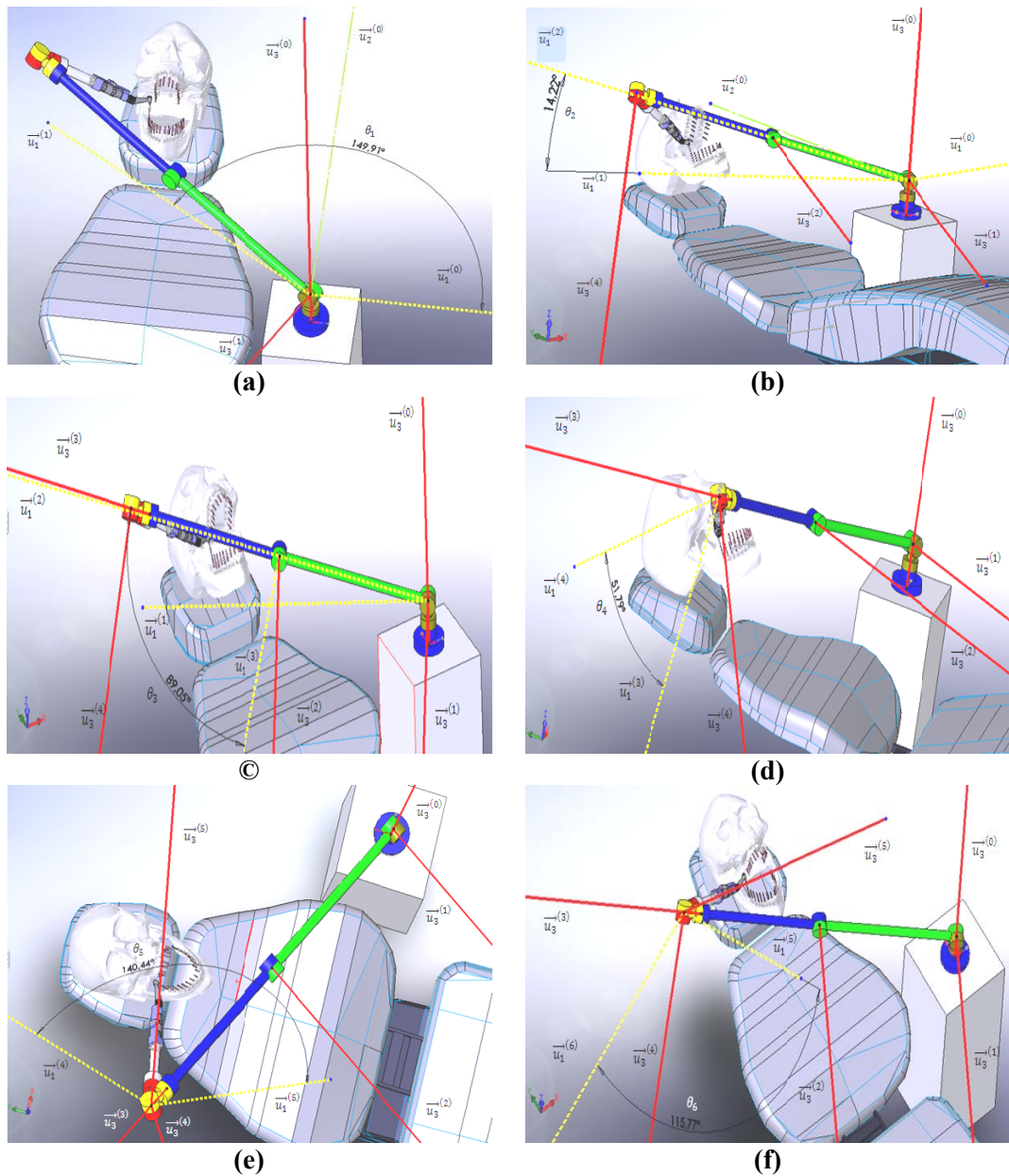
Figure 3.11: Values of the Joint Variables from the CAD Model, (a) θ_1, (b) θ_2, (c) θ_3, (d) θ_4, (e) θ_5 ,(f) θ_6.

As indicated in the Figure 3.11, the inverse kinematic equations supply the values of the joint variables accurately. Also, the CAD model is transferred to a SimMechanics block diagram model using the appropriate software. The "mates"

defined in the Solidworks are transferred to the SimMechanics model as joints and links are transferred as bodies.
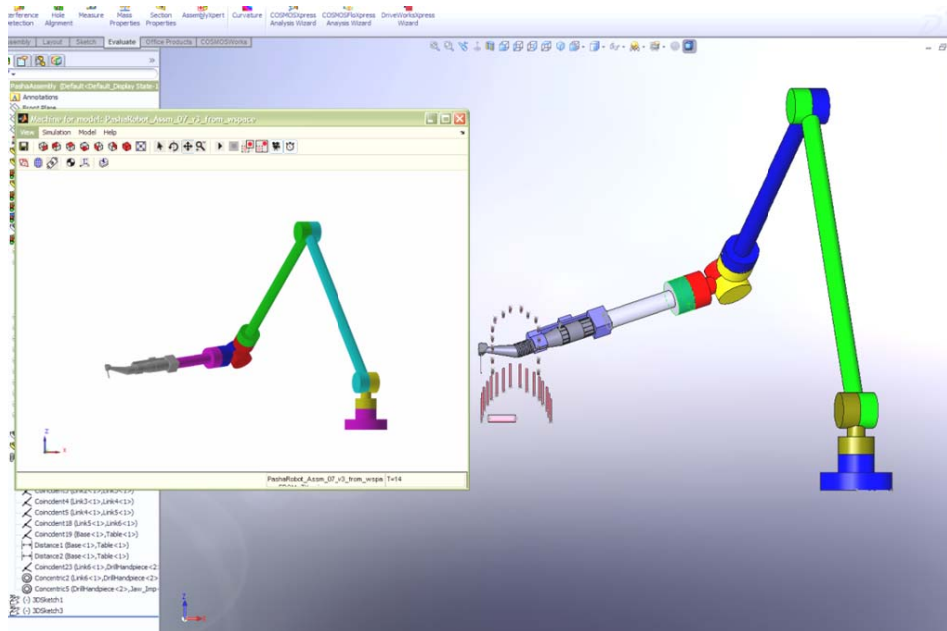
Figure 3.12: The CAD Model and SimMechanics Model Obtained from the CAD Model

The joint variables, which are calculated using the inverse kinematic equations, are applied to the SimMechanics model to manipulate the robotic arm to the target position. As seen in the Figure 3.12, the SimMechanics model reaches to the same location exactly as the CAD model where the position and orientation data is taken. In addition to this figure, main 6R robotic simulator with lines can be used to show the position and orientation of the robotic arm as illustrated in the Figure 3.13. As a result, the kinematic equations are proven and they are now able to be used in the optimization procedure.
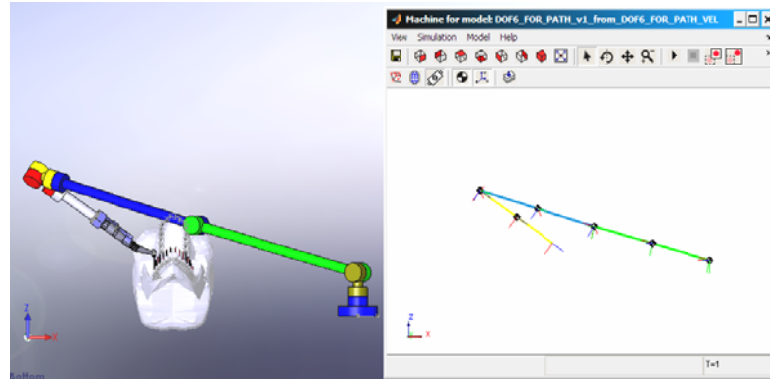
(a)
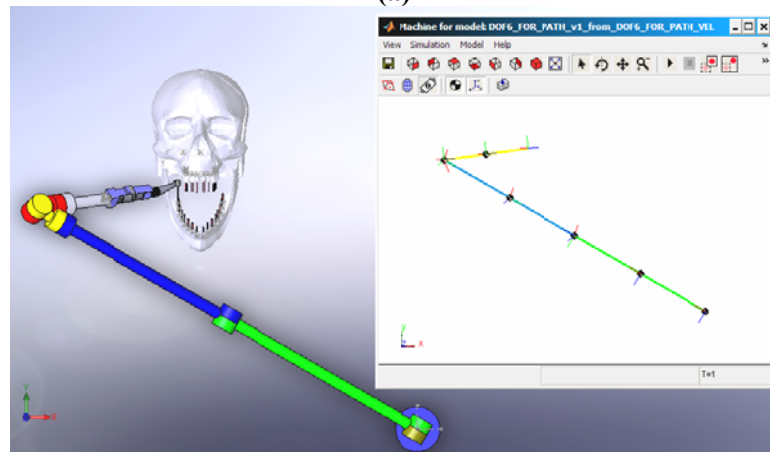
(b)

Figure 3.13: The CAD Model with 6R SimMechanics Model (a) From ZX (b) From YX

In the implant operation, also a drilling process occurs. In order to simulate the drilling process in the operation path, the position and orientation of the tool' tip point have to be included in the kinematic equations. During the drilling process, the tip point of the dental tool drives through the tooth. While the drilling operation occurs, the length of the $\overrightarrow{AB}$ starts to decrease and finally reaches to zero.

When the tip point of the dental tool starts to move inside the tooth, the dentist turns the dental tool along the axis of $\overrightarrow{AB}$. Therefore, besides the drilling process, there is also a turning process. To mathematically model the turning process, Rodrigues formula is introduced.
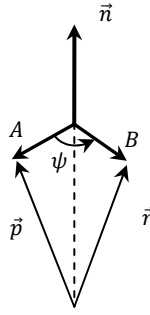
Figure 3.14: Rotation about a Specified Axis

In the Figure 3.14, $\vec{n}$ is the unit vector along the axis of rotation and ψ is the angle of rotation. The $\vec{p}$ rotates about $\vec{n}$ to $\vec{r}$. To formulate this operation Rogrigues formula is used as,

$$\bar{r} = \left[\hat{I}\cos\psi + \tilde{n}\sin\psi + \bar{n}\bar{n}^t(1-\cos\psi)\right]\bar{p} \tag{3.5}$$

Thus, the total orientation matrix is also being multiplied with the orientation matrix of the turning process calculated at equation 3.5 as,

$$\hat{C}_{TOT} = \hat{C}^{(0,6)}\hat{C}_{AB} \tag{3.6}$$
$$\hat{C}_{AB} = \hat{I}\cos\psi + \tilde{n}\sin\psi + \bar{n}\bar{n}^t(1-\cos\psi) \tag{3.7}$$

The turning process occurs around the axis of "$\overrightarrow{AB}$" about "180°". In order to calculate the required position matrix again, starting from point "A" and using vector calculations, one can reach the position of the wrist point. To simulate the drilling and turning processes mathematically, the changes in the values of the turning angle "ψ" in equation 3.7 and the length of the vector "A_Tool_Tip" in the Figure 3.9 are tabulated in the Table 3.2.

Table 3.2: Changes in Angle "ψ" and the Vector "A_Tool_Tip"

Step	The value of the angle ψ (degree)	The lengths of the Vector A_Tool_Tip (mm)
1	0	32
2	30	27
3	60	22
4	90	17
5	120	12
6	150	7
7	180	0

In the lights of the given information above, during a simple implant operation, the dentist takes the dental tool from the initial positions, extends the manipulator's tip point to the furthest tooth, and then starts to the drilling process while turning the dental tool side by side and finally stops at the final position. To generate the necessary path that is used during the optimization process, the furthest tooth is chosen for final position in order to enlarge the workspace volume and to reach to closer teeth easily. The generated path is a simple path to simulate the implant operation and is acquired from the ideas of the many dentists and can be applicable to different patients. While the manipulator moves along the generated path, the kinematic configuration of the manipulator has to be kept constant during the implant operation. As stated in the inverse kinematics section in the Appendix A.2, due to the sign ambiguities, the signs of some of the joint variables have to be determined before applying the inverse kinematic equations. Due to the fact that, the sign of "σ_1" for the angle "θ_1" is chosen as "+1", so that left shouldered configuration is used. The sign of "σ_2" for the angle "θ_3" is taken as "-1", so that elbow up configuration is applied. The sign of "σ_5" for the angle "θ_5" is selected as "+1", so that wrist up configuration is preferred. Finally the generated path is demonstrated in the Figure 3.15.
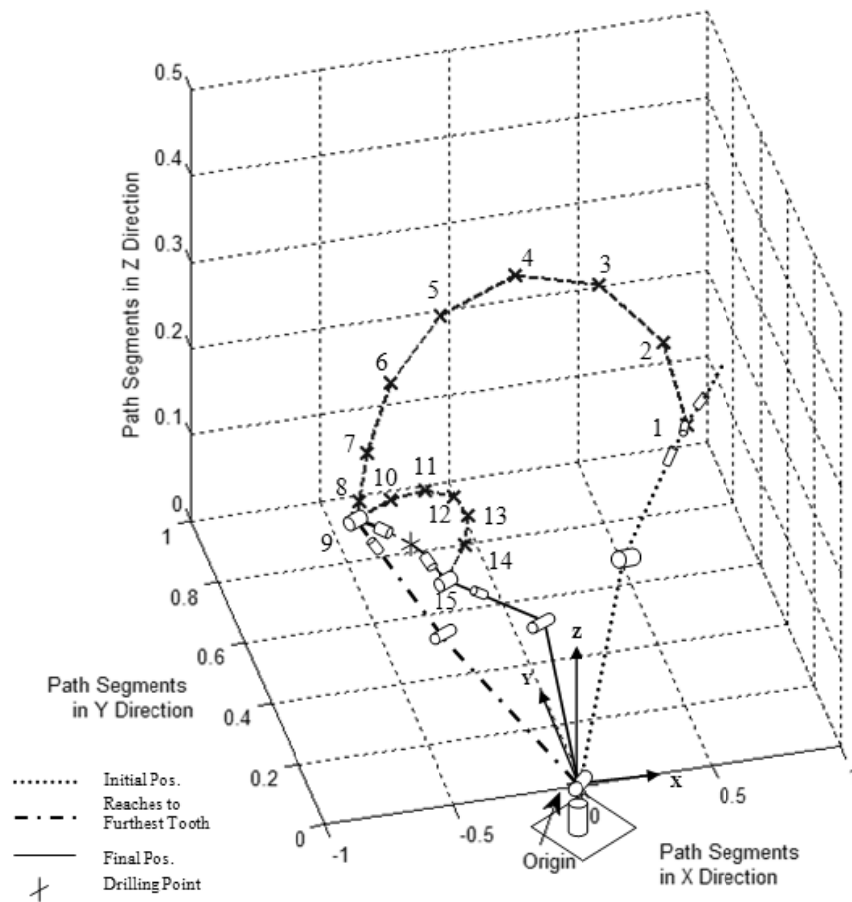
Figure 3.15: The Generated Path ("Reaches to Furthest Tooth" Position Is Same As in the CAD Model.)

3.4. DYNAMICS OF THE PASSIVE HAPTIC ROBOTIC ARM

In this thesis, the main purpose of the optimization process is to improve the transparency of the passive haptic robotic arm while minimizing the energy consumption. In order to achieve this aim, minimizing the end-effector's torque values at the user side has to be investigated. The end-effector's parasitic forces/torques consists of mass/inertia elements, gravity forces, and friction and they occurs during the manipulator's motion [28, 53] Therefore, to calculate the end-effector torque values at the user side a motion analysis has to be performed

using the dynamics equations of the manipulator. As a result, dynamic equations of the passive haptic robotic arm have to be derived.

Dynamics equations, besides being a bit complex to derive, are required to simulate the motion of the manipulator and to design different control algorithms [45]. Derivation of the dynamic equations helps the designer to test control algorithms and to perform different motion planning techniques without constructing a physically available system. By computing the necessary forces and torques in the joint space allow user to choose appropriate actuators and transmission elements. Main fact about dynamic equations is that the derivation of the dynamic equations is highly complicated. There are many different approaches to derive the manipulator dynamics in the joint space. The most popular among them are Lagrange-Euler [54] and Newton-Euler [55] methods. The Newton-Euler method which is used in this study, allow designer to obtain the equations in a recursive form, and it is computationally more efficient than the Lagrange-Euler method [45] Using the recursive Newton-Euler formulation, one can compute the joint torque values in the vector form when necessary motion variables such as the joint angles, θ, the joint velocities, $\dot{\theta}$, and the joint accelerations, $\ddot{\theta}$ are supplied. To determine the joint variables in position, velocity and acceleration levels, first the recursive formulation is used in kinematic equations. Then forces and torques of the joints are derived [45, 46, 51].

3.4.1.NEWTON-EULER EQUATIONS

To apply the Newton-Euler equations to a manipulator, each link has to be accepted as a rigid body. If the position of the center of mass and inertia tensor of the link are known, then the forces and moments acting on the link can be computed. In order to move the manipulator, a motion has to be applied to the joints. The forces are function of the link accelerations and mass distribution. Newton's equation deals with the forces and Euler's equations describe the interactions of the inertias using moment equation [46].

35

3.4.1.1.NEWTON'S EQUATION

Newton's equation describes the forces acting on the center of mass of the link which is accelerating with $\bar{a}_{ci}$. Derivation of the acceleration of the mass center, $\bar{a}_{ci}$ is given in the Appendix C. The necessary force to actuate the link with the acceleration $\bar{a}_{ci}$ is calculated by using the Newton's equation as,

$$\bar{F}^{(i)} = m\bar{a}_{ci} \tag{3.8}$$

for $i = 1,2, \dots , n$ where "m" is the total mass of the body.

3.4.1.2.EULER'S EQUATION

In order to compute the moment acting on the link which is rotating with the angular velocity "ω" and angular acceleration "α", Euler's equation can be used as,

$$\bar{M}_c^i = \hat{J}_c^i \bar{\alpha}^i + \widetilde{\omega}^i \hat{J}_c^i \bar{\omega}^i \tag{3.9}$$

for $i = 1,2, \dots , n$ where "$\hat{J}_c^i$" represents the inertia tensor of the link written in frame "$\vec{C}$" which is located at the center of the mass. Another important point of the N-E equations is that the angular velocities, angular accelerations and mass center accelerations are computed with respect to inertial frame to take the time derivatives easily. Therefore, because of the computation of the inertia tensor in body frame, they have to be transferred to the body frames again using necessary orientation matrices introduced in the forward kinematics section as equation A.5 in order to be used in the N-E equations.

3.4.2.ACTUATION FORCES AND TORQUES

There are two types of dynamic problems. In forward or direct dynamics, the forces and moments acting at the end-effector is known and the resultant motion has to be computed to correspond the acting forces and moments. In inverse dynamics, the desired motion is specified and actuation forces and torques are expected to be

found. In order to find these forces and torques acting on the link, the joint torques are needed to be calculated. This can be done by writing the force and moment balance equations of the each link. Each link has forces and moments acting on it by its proximal neighbor and distal neighbor. In the Figure 3.16, the forces and moments acting on a link are represented.
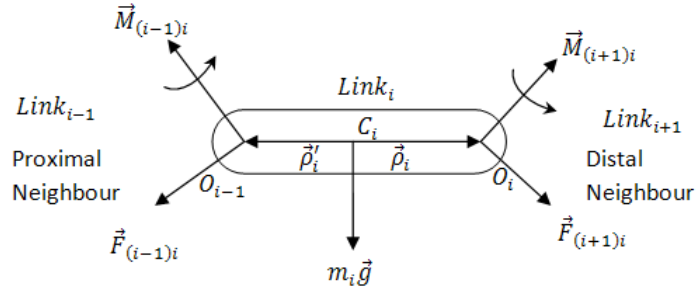
Figure 3.16: The Forces and Moments Acting on a Link

In the Figure 3.16, "$\vec{F}_{(i-1)i}$" represents the force acting to link (i) from the proximal link and "$\vec{F}_{(i+1)i}$" represents the forces acting from the link (i) to the distal neighbor. "$\vec{M}_{(i-1)i}$" is the moment acting on the proximal neighbor and "$\vec{M}_{(i+1)i}$" is the moment acting on the distal link. "$\vec{\rho}_i'$" and "$\vec{\rho}_i$" are vectors from center of mass of the link to the proximal and distal neighbor, respectively. "$m_i\vec{g}$" represents the gravitational force acting on center of mass of the link. The force equation can be shown as,

$$m_i\vec{a}_{ci} = m_i\vec{g} + \vec{F}_{(i-1)i} + \vec{F}_{(i+1)i} \tag{3.10}$$

The moment equilibrium can be represented as,

$$\breve{J}_{ci} \cdot \vec{\alpha}_i + \vec{\omega}_i \times \breve{J}_{ci} \cdot \vec{\omega}_i = \vec{M}_{(i-1)i} + \vec{M}_{(i+1)i} + \vec{\rho}_i \times \vec{F}_{(i+1)i} + \vec{\rho}_i' \times \vec{F}_{(i-1)i} \tag{3.11}$$

The motion is given to the manipulator, thus the acceleration of the center of mass "$\vec{a}_{ci}$", angular acceleration of the link "$\vec{\alpha}_i$", and the angular velocity of the link "$\vec{\omega}_i$" are all known. The derivation of the recursive kinematic equations is discussed in the Appendix C. If the forces found by using Newton's equation at equation 3.8 and the moments found by using Euler's equation at equation 3.9 are put into the equation 3.10 and 3.11, respectively, the forces and moments applied to the joints can be calculated in recursive matrix form as,

$$\bar{F}^{(i)}_{(i-1)i} = \hat{C}^{(i,i+1)} \bar{F}^{(i+1)}_{i(i+1)} - \bar{F}^{(i)}_i - m_i \bar{g}_i \tag{3.12}$$

$$\bar{M}^{(i)}_{(i-1)i} = \hat{C}^{(i,i+1)} M^{(i+1)}_{i(i+1)} + \tilde{\rho}_i \hat{C}^{(i,i+1)} \bar{F}^{(i+1)}_{i(i+1)} - \tilde{\rho}'_i \bar{F}^{(i)}_{(i-1)i} + \vec{M}^{(i)}_i \tag{3.13}$$

In contrast to the recursive kinematic equations, recursion, now, starts from the last link, "n", and goes to the first link. The gravitational acceleration can be transferred using the appropriate orientation matrix as,

$$\bar{g}^{(i)} = \hat{C}^{(i,0)} \bar{g}^{(0)} \tag{3.14}$$

where

$$\bar{g}^{(0)} = -g\bar{u}_3 \tag{3.15}$$

Finally, the moments and forces acting on the links are computed using the recursive Newton-Euler method. Now, necessary actuation torques can be calculated using the equation 3.13 and the orientation matrices as,

$$\bar{T}_i = \bar{u}^t_3 \hat{C}^{(i-1,i)} \bar{M}^{(i)}_{(i-1)i} \tag{3.16}$$

3.4.3. THE STATE SPACE EQUATION

In order to express the dynamic equations of a manipulator in a more compact form instead of writing long and complicated equations, Newton-Euler equations can be evaluated symbolically in joint space using state space equation form [46] as,

$$\boldsymbol{\tau'} = \boldsymbol{m}(\theta)\ddot{\theta} + \boldsymbol{v}(\theta,\dot{\theta}) + \boldsymbol{g}(\theta) \qquad (3.17)$$

where "$\boldsymbol{m}$" denotes the $n \; x \; n$ mass matrix of the manipulator, "$\ddot{\boldsymbol{\theta}}$" is the $n \; x \; 1$ angular acceleration vector, "$\boldsymbol{v}$" is the $n \; x \; 1$ nonlinear velocity matrix, and "$\boldsymbol{g}$" is the $n \; x \; 1$ gravity force matrix. Mass matrix and gravitational force matrix are depended only on "$\theta's$" whereas the nonlinear velocity matrix is more complex which includes elements, both the functions of "θ" and "$\dot{\theta}$". By using this representation, the joint torque values are calculated in the joint space.

3.4.4. THE JACOBIAN AND ITS TIME DERIVATIVE

The derived dynamics equations up to now represent the manipulator dynamics in joint space, in other words the torque values are derived using the values and time derivatives of the manipulator's joint angles in equation 3.15. The aim of the study is declared as the maximization of the transparency of the haptic device. In order to maximize the transparency, the parasitic torques and forces, felt by the user, have to be minimized. In order to reduce this parasitic forces and torques, the torques calculated in the joint space using recursive method have to be transferred to the Cartesian space. Thus the forces and torques felt by the user can be minimized. Transferring the torque values calculated in the joint space can be acquired with the usage of the Jacobian matrix and its time derivative.

There are two ways to compute the Jacobian of any manipulator. One of them is to use recursive kinematic formulation. In the recursive kinematic method, at every calculation step starting from the orientation of the links, the angular and linear velocities of the link are computed while in each step one of the "$\dot{\theta}'s$" is taken one

and the others are taken zero for "$i = 1,2, \ldots, n$". Finally, the recursive formulation gives the "$n \times n$" Jacobian matrix of the manipulator. This recursive formulation was embedded into the dynamic equations and has been used to prove the Jacobian matrix found using the second way. Also, the computational time of this way is a bit longer than the second way.

Second way of the calculation of the Jacobian is to use equations that are derived in the forward kinematics section which are equations A.3 and A.9. The orientation matrix is found in the equation A.3 and the position of the wrist point is calculated in the equation A.9. First using the equation A.9 and taking the partial derivative with respect to the joint variables gives as,

$$\bar{J}_{ri} = \frac{\partial \bar{r}}{\partial \theta_i} \tag{3.18}$$

Using the equation 3.18 and applying for six joint variables results to,

$$\bar{J}_{r1} = \frac{\partial \bar{r}}{\partial \theta_1} = e^{\tilde{u}_3 \theta_1}[-\bar{u}_1 d_2 + \bar{u}_2(a_2 \cos \theta_2 + d_4 \sin \theta_{23})] \tag{3.19}$$

$$\bar{J}_{r2} = \frac{\partial \bar{r}}{\partial \theta_2}$$

$$= e^{\tilde{u}_3 \theta_1}[\bar{u}_1(-a_2 \sin \theta_2 + d_4 \cos \theta_{23}) + (-a_2 \cos \theta_2 - d_4 \sin \theta_{23})\bar{u}_3] \tag{3.20}$$

$$\bar{J}_{r3} = \frac{\partial \bar{r}}{\partial \theta_3} = e^{\tilde{u}_3 \theta_1}[d_4 \cos \theta_{23}\bar{u}_1 - d_4 \sin \theta_{23}\bar{u}_3] \tag{3.21}$$

$$\bar{J}_{r4} = \bar{J}_{r5} = \bar{J}_{r6} = 0 \tag{3.22}$$

Then, the orientation matrix from equation A.3 is used to determine the angular velocity influence coefficient as,

$$\bar{J}_{ai} = col\left[\frac{\partial \hat{C}}{\partial \theta_i} \hat{C}^t\right] \tag{3.23}$$

The equation 3.23 is calculated for six joint variables,

$$\bar{J}_{a1} = col\left[\frac{\partial \hat{C}}{\partial \theta_1} \hat{C}^t\right] =$$

$$col\left[\left(\tilde{u}_3 e^{\tilde{u}_3 \theta_1} e^{\tilde{u}_2 \theta_{23}} e^{\tilde{u}_3 \theta_4} e^{\tilde{u}_2 \theta_5} e^{\tilde{u}_3 \theta_6}\right)\left(e^{-\tilde{u}_3 \theta_1} e^{-\tilde{u}_2 \theta_{23}} e^{-\tilde{u}_3 \theta_4} e^{-\tilde{u}_2 \theta_5} e^{-\tilde{u}_3 \theta_6}\right)\right] =$$

$$col[\tilde{u}_3] = \bar{u}_3 \tag{3.24}$$

$$\bar{J}_{a2} = e^{\tilde{u}_3 \theta_1} \bar{u}_2 \tag{3.25}$$

$$\bar{J}_{a3} = e^{\tilde{u}_3 \theta_1} \bar{u}_2 \tag{3.26}$$

$$\bar{J}_{a4} = e^{\tilde{u}_3 \theta_1} e^{\tilde{u}_2 \theta_{23}} \bar{u}_3 \tag{3.27}$$

$$\bar{J}_{a5} = e^{\tilde{u}_3 \theta_1} e^{\tilde{u}_2 \theta_{23}} e^{\tilde{u}_3 \theta_4} \bar{u}_2 \tag{3.28}$$

$$\bar{J}_{a6} = e^{\tilde{u}_3 \theta_1} e^{\tilde{u}_2 \theta_{23}} e^{\tilde{u}_3 \theta_4} e^{\tilde{u}_2 \theta_5} \bar{u}_3 \tag{3.29}$$

The Jacobian matrix is found at the wrist point of the manipulator and have to be transferred to the tip point using orientation matrices as,

$$\bar{J}_{p1} = \bar{J}_{r1} + d_6 \tilde{J}_{a1} \hat{C} \bar{u}_3 \tag{3.30}$$

$$\bar{J}_{p2} = \bar{J}_{r2} + d_6 \tilde{J}_{a2} \hat{C} \bar{u}_3 \tag{3.31}$$

$$\bar{J}_{p3} = \bar{J}_{r3} + d_6 \tilde{J}_{a6} \hat{C} \bar{u}_3 \tag{3.32}$$

$$\bar{J}_{p4} = d_6 \tilde{J}_{a4} \hat{C} \bar{u}_3 \tag{3.33}$$

$$\bar{J}_{p5} = d_6 \tilde{J}_{a5} \hat{C} \bar{u}_3 \tag{3.34}$$

$$\bar{J}_{p6} = d_6 \tilde{J}_{a6} \hat{C} \bar{u}_3 \tag{3.35}$$

Using the derived equations, the Jacobian matrix at the tip point can be formed as,

$$\hat{J}_p = \begin{bmatrix} \bar{J}_{p1} & \bar{J}_{p2} & \bar{J}_{p3} & \bar{J}_{p4} & \bar{J}_{p5} & \bar{J}_{p6} \\ \bar{J}_{a1} & \bar{J}_{a2} & \bar{J}_{a3} & \bar{J}_{a4} & \bar{J}_{a5} & \bar{J}_{a6} \end{bmatrix} \tag{3.36}$$

After obtaining the Jacobian matrix, time derivate of it can be found easily as,

$$\dot{\hat{J}}_p = \frac{\partial J_p}{\partial \theta_i} \dot{\theta}_\iota \tag{3.37}$$

The Jacobian and time derivative of the Jacobian matrix are computed to be used in order to transfer of the torque values to the Cartesian space.

3.4.5. THE FORCES AND TORQUES AT CARTESIAN SPACE

In the equation 3.17, the torque values are computed at the joint space using joint angles and its time derivatives. This equation helps to determine the necessary torque values for the specified motion, but in order to examine the Cartesian forces and moments acting on the manipulator causing from the accelerations acting on the end-effector, the torque values have to be transformed into the Cartesian space using the Jacobian and its time derivative [46].

$$\tau = J^t(\boldsymbol{M} \cdot \mathbf{a} + \boldsymbol{V} + \boldsymbol{G}) \tag{3.38}$$

where "$\mathbf{M}$" denotes the Cartesian mass matrix of the manipulator, "$\mathbf{a}$" is the linear acceleration vector, "$\mathbf{V}$" is the nonlinear velocity matrix in the Cartesian space, and "$\mathbf{G}$" is the vector of gravity terms in Cartesian space. "$\mathbf{a}$" is the linear acceleration vector written in the tip point's frame. The derivation of the torque values from joint space to Cartesian space can be handled using the Jacobian and differential Jacobian as,

$$J^{-t}\boldsymbol{\tau}' = J^{-t}\boldsymbol{m}(\theta)\ddot{\theta} + J^{-t}\boldsymbol{v}(\theta,\dot{\theta}) + J^{-t}\boldsymbol{g}(\theta) \tag{3.39}$$

$$\tau = J^{-t}\boldsymbol{m}(\theta)\ddot{\theta} + J^{-t}\boldsymbol{v}(\theta,\dot{\theta}) + J^{-t}\boldsymbol{g}(\theta) \tag{3.40}$$

Now, a relationship between the joint angles and time derivatives and Cartesian acceleration is conducted, starting from the definition of the Jacobian matrix,

$$\boldsymbol{v} = J\dot{\theta} \tag{3.41}$$

where "v" is the lineer velocity of the manipulator and "J" is the Jacobian matrix which is multiplied by the angular velocity "$\dot{\theta}$". The equation 3.41 is differentiated with respect to the time,

$$\mathbf{a} = J\ddot{\theta} + \dot{J}\dot{\theta} \tag{3.42}$$

and solving equation 3.42 to obtain the joint space acceleration gives us,

$$\ddot{\theta} = J^{-1}\mathbf{a} - J^{-1}\dot{J}\dot{\theta} \tag{3.43}$$

Substituting equation 3.43 into equation 3.40 results to,

$$\tau = J^{-t}\boldsymbol{m}(\theta)(J^{-1}\mathbf{a} - J^{-1}\dot{J}\dot{\theta}) + J^{-t}\boldsymbol{v}(\theta,\dot{\theta}) + J^{-t}\boldsymbol{g}(\theta) \tag{3.44}$$

$$\tau = J^{-t}\boldsymbol{m}(\theta)J^{-1}\mathbf{a} - J^{-t}\boldsymbol{m}(\theta)J^{-1}\dot{J}\dot{\theta} + J^{-t}\boldsymbol{v}(\theta,\dot{\theta}) + J^{-t}\boldsymbol{g}(\theta) \tag{3.45}$$

Using the terms in equation 3.45, the terms in the equation 3.38 can be expressed as,

$$\boldsymbol{M} = J^{-t}\boldsymbol{m}(\theta)J^{-1}\mathbf{a} \tag{3.46}$$

$$\boldsymbol{V} = -J^{-t}\boldsymbol{m}(\theta)J^{-1}\dot{J}\dot{\theta} + J^{-t}\boldsymbol{v}(\theta,\dot{\theta}) \tag{3.47}$$

$$\boldsymbol{G} = J^{-t}\boldsymbol{g}(\theta) \tag{3.48}$$

Now, the torque values are computed in the Cartesian space and later on are used in the objective function of the optimization problem.

3.5. THE OBJECTIVE FUNCTION FOR MAXIMUM TRANSPARENCY

In the beginning of the dynamics section, the main aim of this study is mentioned as to maximize the transparency of the passive haptic robotic arm. Therefore, parasitic torques as seen from the user side have to be minimized to achieve this problem. First joint torque values are computed in joint space and then using the Jacobian

matrices, they are transferred into the Cartesian space. The calculated values are the parasitic forces/torques as seen from the user and have to be ideally zero. As a result, the objective function to be minimized was selected as the norm of the sum of the parasitic terms as in [28]

$$f = Norm(\boldsymbol{M} \cdot \mathbf{a} + \boldsymbol{V} + \boldsymbol{G}) \tag{3.49}$$

The operation path includes 15 segments to simulate a simple implant operation and to acquire a smooth path and obtain the optimization results accurately. Since the generated implant operation path is divided into 15 segments, the overall objective function is developed by a weighted sum of the Norm computed in each segment,

$$f_{tot} = \sum_{i=1}^{j} w_i Norm(\boldsymbol{M} \cdot \mathbf{a} + \boldsymbol{V} + \boldsymbol{G}) \tag{3.50}$$

Here, w_i represents the contribution of the each path segment to the optimization results. The initial 8 segments in the implant operation path correspond to approach to the implant hole and their effect at the implant operation is less than the other segments, hence they are taken lower than $w_i = 1$ in order to reduce the effect to the optimization results.

3.6. DESIGN PARAMETERS AND CONSTRAINTS

The objective function to maximize the transparency derived in equation 3.50 includes the design parameters of an optimum 6R passive haptic robotic arm. The methodology that is used in the optimization problem deals with the size and shape of the manipulator's links and the position of the operation path with respect to the base position. Since the shape of operation path in addition to the velocity and acceleration of the tip point along the path can vary with characteristics of the dental operations, they are taken into consideration [28].

Mass matrix computed in equation 3.46 includes elements which are functions of link masses, link lengths, and link moments of inertia. Link masses and link

moments of inertia can be parameterized as functions of link lengths. If the links are accepted as cylinders, the mass can be defined as,

$$m(l) = \rho \frac{\pi}{4} (b^2 - a^2)l \tag{3.51}$$

where "ρ" is the density of the cylinder's material, "a" is the inner diameter, "b" is the outer diameter, and "l" is taken as the length of the link. Likewise, the inertia of the links can be defined as,

$$\hat{J}_c = \begin{bmatrix} J_1 & 0 & 0 \\ 0 & J_2 & 0 \\ 0 & 0 & J_3 \end{bmatrix} \tag{3.52}$$

where

$$J_1 = m(l) \frac{\left(\frac{b}{2}\right)^2 + \left(\frac{a}{2}\right)^2}{2} \tag{3.53}$$

$$J_2 = J_3 = m(l) \left(3 \left(\frac{b}{2}\right)^2 + 3 \left(\frac{a}{2}\right)^2 + l^2 \right) / 12 \tag{3.54}$$

Here, as mentioned before when the "$\hat{J}_c$" is added to the dynamic equations, most of the time "$\hat{J}_c$" is taken in the principal body frame because it appears as a diagonal matrix. Also, nonlinear velocity and the gravity terms are the functions of link lengths. As a result, the link lengths can be chosen as design parameters for the objective function, then minimization of the torque values at the joints result to optimum link lengths.

Determination of position of the operation path with respect to base frame of the robotic arm is one of the design problems possibly an important one since the size and the configuration of the manipulator depend on operation path. As stated in the generation of the path, at first, position and orientation of the tool's tip point moving along the operation path is given to the inverse kinematic equations. Then,

45

in each optimization step, the joint variables, θ_i's, are determined using inverse kinematic equations accepting the link lengths which are computed by the optimization algorithm. To introduce the coordinates of the base frame into the optimization problem, in each optimization step the coordinates of the base frame have to be embedded in the position definition of the generated operation path so that the optimization problem includes the coordinates of the base frame. Consequently, the link lengths (a_2, d_4, d_6) and the coordinates of the base frame (X, Y, Z) are chosen as design parameters of the optimization process.

Determination of constraints is the one of important part of the optimization process. With the usage of optimization constraints the search space of the optimization process can be narrowed and thus the global optimum solution can be found more easily within the search space. The designed passive haptic robotic arm is expected to be placed in the dental operation room and is aimed to be mounted and demounted onto a special table without changing regular order of the dentists. After interviewing with many dentists, it is recovered that most of the dentists are right handed; therefore dental tools are preferred to be situated at the right hand side of the dentist. Hence, the base position of the arm, due to that the dimensions of the table, which the robotic arm is going to be mounted, cannot be determined arbitrarily. Also, the face, lips, and cheeks of the patient make a blockage to the dentist which limits the movements of the dentist's hand. Therefore, the constraints of the optimization problem have to be determined in light of this information.

Moreover, singularities have to be concerned as stated before since they prevent motion and cause loss of control. To avoid singularities, necessary implantation is embedded into the optimization problem and the constraints are determined according to this. Also, the longest path from the base position to the furthest tooth is taken as a constraint so that the dentist can move the tip of the manipulator freely within the workspace. As the inequality constraints, the position of tool tip point of the robotic arm has to be checked in each path segments if it is in the allowable workspace. Equation 3.55 describes the necessary constraints which control

whether the manipulator is in the allowable workspace and the solution of the inverse kinematic equations exists for the entire operation path or not:

$$(a_2 - d_4) \le \sqrt{x_i^2 + y_i^2 + z_i^2} \le (a_2 - d_4) \qquad (3.55)$$

where x_i, y_i, z_i are the coordinates of the tip point calculated at each operation path segments.

In addition to the equation 3.55, the joint variables, θ_i's, are bounded to avoid singularities and to stay fixed in the determined configuration. Lower and upper bounds for the joint variables are defined and tabulated in the Table 3.3 [51]. The robotic arm can move freely within the determined workspace bounded by different lower and upper limits defined for each joint variable. Defined limits are assumed to be comprehended through hard-limits. Though defining these boundaries, the manipulator is prevented to enter the singularities. The lower limit of θ_5 is taken as 0.1 because it causes singularity when it becomes 0.

Table 3.3: Lower and Upper Bounds of the Joint Variables

Joint Variables (degree)	Lower Bounds	Upper Bounds
θ_1	0	160
θ_2	-225	45
θ_3	90	225
θ_4	-180	225
θ_5	0.1	175
θ_6	-266	266

Not only the joint variables are bounded, but also the links lengths and links offsets are bounded, because the torque values can be found really minimized outside the bounds but the optimized link lengths are physically unavailable to construct.

Table 3.4: Lower and Upper Bounds for the Design Parameters

Parameter	a_2 (mm)	d_4 (mm)	d_6 (mm)	X (mm)	Y (mm)	Z (mm)
Lower Bound	100	100	10	-120	-150	-500
Upper Bound	600	600	250	150	100	500

The upper and lower limits of the design parameters are listed in the Table 3.4. The limits of the coordinates of the base frame are taken from the CAD model and the limits represent the maximum dimensions of the table on where the manipulator is mounted. Finally, a relationship between the link lengths and link offsets is defined as,

$$a_2 \geq d_4 \tag{3.56}$$

$$a_2 \geq 1.1 d_6 \tag{3.57}$$

$$a_2 \geq 1.25 d_6 \tag{3.58}$$

As a final point to this section, the objective function is defined in equation 3.50, the constraints to narrow the search space are in the equations 3.55 to 3.58, and the boundaries are listed in Table 3.3 and 3.4. These equations represent a constrained nonlinear optimization problem because the problem has a nonlinear objective function with equality and inequality constraints, upper and lower limits for design parameters [27].

3.7. OPTIMIZATION RESULTS

The constrained nonlinear optimization problem, which is constructed up to now, can be solved using two different optimization algorithms: Sequential Quadratic Programming (SQP) [56] and Genetic Algorithms (GA) [57]. The dynamic equations for objective function and the kinematic equations defining the motion and the constraints are programmed using MATLAB. Hence MATLAB® Optimization Toolbox is used to solve the optimization problem.

In general, SQP is the most successful method to solve nonlinear constrained optimization problems. SQP is an iterative method that at first models the nonlinear problem at a given approximation and then develops a quadratic sub problem. At each iteration, a new iterative is generated in the search direction using the solution of the quadratic sub problem. Then this iterative is used to construct a better approximation. This process continues until the approximation converges to a solution that satisfies given constraints.

The GA in principle is a random search algorithm inspired by natural evolution. The GA starts with the random production of a population of chromosomes. Then, the reproduction of a new population according to their objection function values, also called fitness function, starts where chromosomes with higher fitness values have probability of contributing to next generation. Crossover selects two individuals from the population and exchanges their genetic material. Mutation is a rare event that randomly changes a gene of a chromosome. Both crossover and mutation are used to enlarge the search space.

Some studies should be examined in detail in order to get more information about the optimization algorithms, their properties, determination of the constraints, construction of the objective functions, selection of the appropriate initial guess [56 - 61].

In the MATLAB program, dynamic equations are embedded into the objective function and the constraints are constructed using the kinematic equations. While using SQP at the solution of the optimization problem, termination tolerances on constraint violation and function value are increased to get optimum results. Population sizes, crossover, and mutation function are set to 20, 0.8, and adaptive feasible, respectively for using GA. These are default values in the Optimization Toolbox for GA. Different GA parameters are tried out but the optimization results have not changed remarkably. Instead of taking mutation rates as uniform, in the

constrained optimization problem adaptive feasible mutation function is preferred which generates directions adaptively in the feasible region [57].

Table 3.5 lists the initial guesses for the link sizes and base frame position. The initial configuration in Table 3.5 represents the link lengths that are obtained from the CAD model and used in the generation of the operation path. However, the initial guess in Table 3.5, which is used as the starting parameter of the optimization process for both SQP and GA, is chosen to be a bit different from the initial configuration. Instead of using the parameters of initial configuration, choosing different parameters leads to the optimization algorithm to find the global optimum solution in the defined search space. The parameters of initial configuration satisfy all the constraints and cause the optimization algorithms to stop.

Before starting to optimization process, the objective function is computed by using the values of parameters of initial configuration. As seen from the Figure 3.17, initial configuration results to very high parasitic torques as seen from the user side at some segments of the path. The reason of the high parasitic forces can be discovered if the CAD model is examined in detail. The value of the θ_3 is very close to singular position at the given operation path. Values of the θ_3 being very close to the singularity causes very high parasitic forces and this is expected to be eliminated after the optimization process.
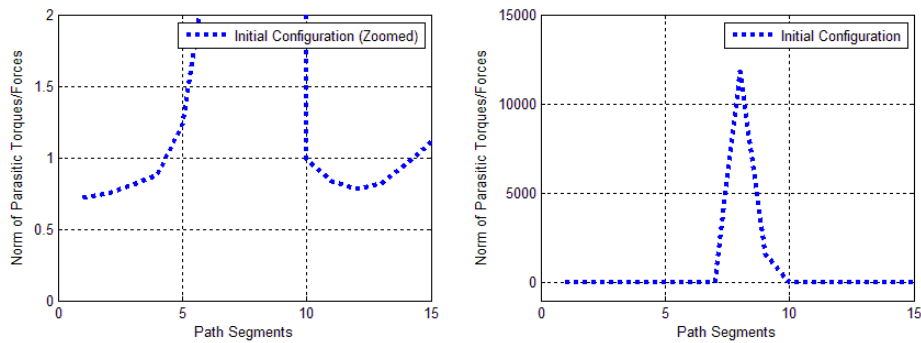
Figure 3.17: Objective Function Calculated using Initial Configuration with Zoomed Part

Table 3.5: Initial Guess and Optimization Results

Optimization Results	a_2(mm)	d_4(mm)	d_6(mm)	X(mm)	Y(mm)	Z (mm)
Initial Configuration	400.00	400.00	264.14	0.00	0.00	0.00
Initial Guess	450	400	200	25	25	75
SQP	599.86	599.86	16.45	-27.50	53.59	-389.58
GA	598.24	597.42	11.98	-119.82	99.62	-313.44

The optimization results computed both using SQP and GA presented in Table 3.5 satisfy all constraints. In the Figure 3.18, norm of the parasitic forces/torques that are computed using the optimized links lengths and base frame coordinates, is found lower than norm of the parasitic forces/toques calculated using the initial configuration.
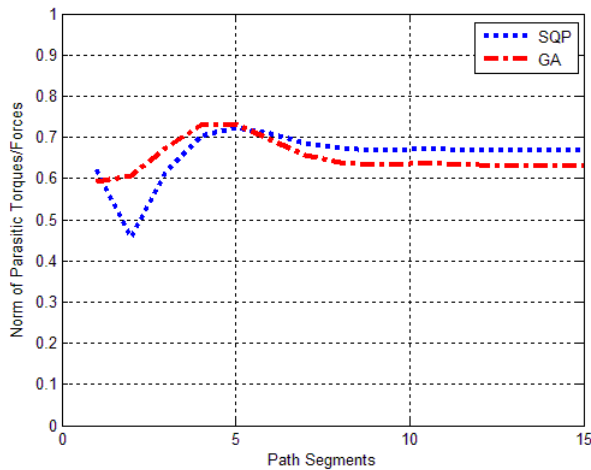
Figure 3.18: Optimization Results

In order to compare the results of the optimization process with results of the initial configuration, the objective functions are calculated using the solutions and represented in the Figure 3.19 together. As stated above, initial configuration results to very high torque values at some segments of the path due to the singularity. However, the results of the optimization process are really very low against the results of initial configuration as shown in the Figure 3.19. By using the

51

optimization process, it is aimed that the manipulator is kept away from the singular positions. From the results it can be understood that one of the aims is achieved. After the optimization process, the minimization of the parasitic forces/torques is achieved as well. GA results are slightly lower than the SQP results. Since the search space is limited, the initial guess helps to find a global optimum solution.
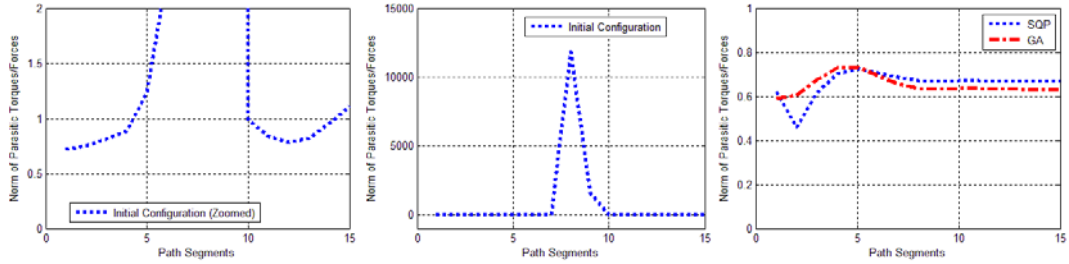
Figure 3.19: Optimization Results with Initial Configuration

The behavior of the objective function during the optimization process is illustrated in the Figure 3.20. The objective function starts from very high values and stops at optimum results. The reduction of the objective function is nearly 50% when using SQP. On the other hand, GA reduces the objective function more than SQP, even though the initial population computes very high function value.

(a)   (b)
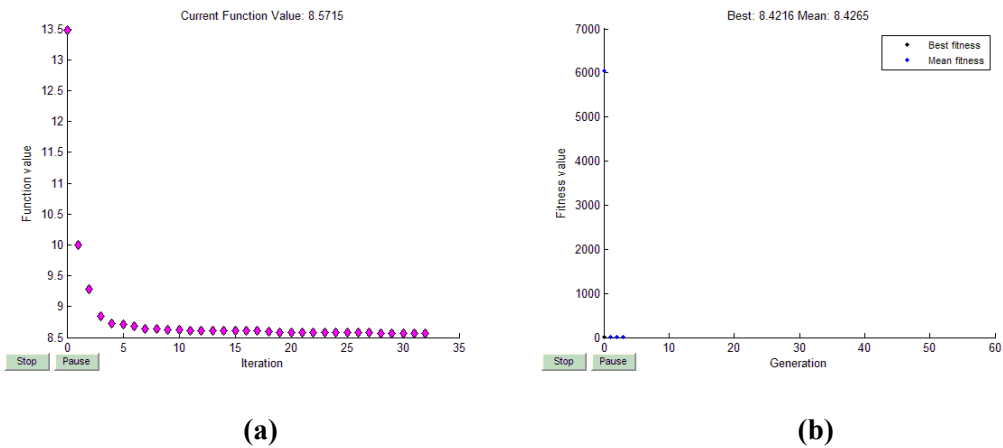
Figure 3.20: Behavior of the Objective Function (a) SQP (b) GA

GA results for the objective function are a slightly lower than the results of SQP. Moreover, the computed link lengths are almost equal in both optimization techniques. On the other hand, the coordinates of the operation path with respect to the base frame is somewhat different. The optimized coordinates of the base frame (X, Y, and Z in Table 3.5) for the robotic arm are still remained within dimensions of the platform where the robotic arm is attached near to the dentist chair. This result was achieved by the help of the constraints that is implemented to the optimization process. The "Z" coordinate requires lowering the base of the robot but that can also be accommodated in a real implementation since the platform attached near to the dentist chair can easily be moved up or down. The lower and upper bounds can be increased to get lower objective function values but this causes the base of the robot to move out of the platform and needs to be attached to the dentist chair even onto the patient which is not acceptable. The newly found base coordinates are illustrated using the 6R robotic simulator built using SimMechanics in the Figure 3.21. The "a_2" parameter is represented with green line, the "d_4" parameter is represented with blue line and the "d_6" parameter is represented with yellow line. Using the results of SQP, "a_2, d_4, d_6" are represented orange, pink and red, respectively. A part of the d_6 parameter of the initial configuration lies under the d_6 parameter of SQP because they both reach to same tip point.

| (a) | (b) |
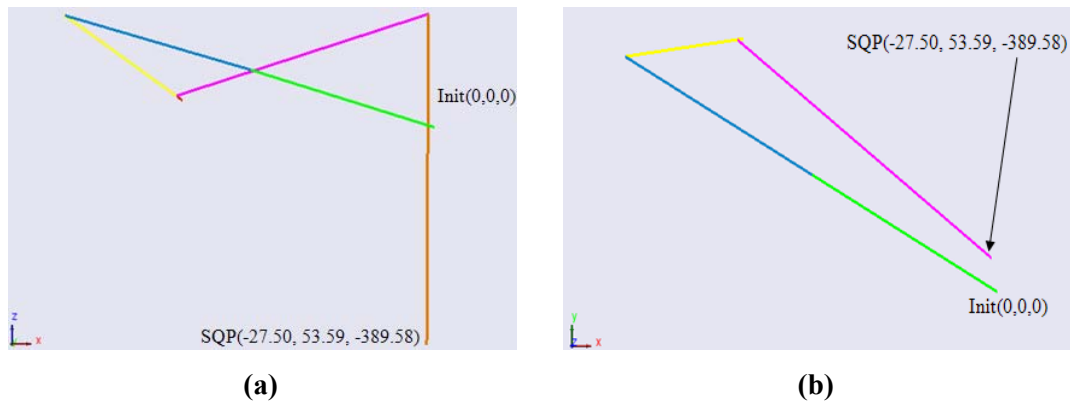
Figure 3.21: Base Coordinates for SQP Results (a) ZX View (b) YX View

53

The change in the base coordinates is also illustrated using the results of the GA in the Figure 3.22. The colors of the parameters are the same as in the initial configuration and SQP Figure 3.21.

| (a) | (b) |
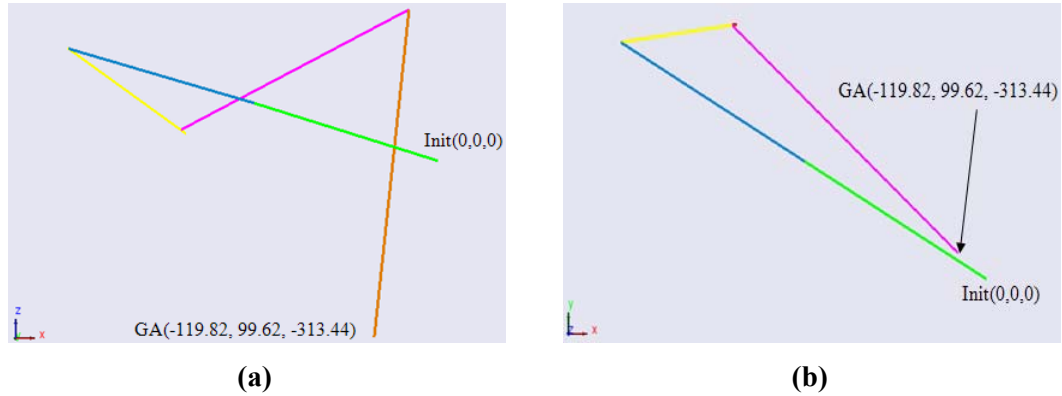
Figure 3.22: Base Coordinates for GA Results (a) ZX View (b) YX View

The optimized positions of base coordinates are demonstrated in the Figure 3.21 and Figure 3.22. From the figures it can be obtained that the links of the manipulator do not approach to the face of the patient and do not prevent the dentist to do the implant operation.

The parasitic torques and forces acting on the end effector is given in the Figure 3.23. From the figure, it is obvious that parasitic torques and forces are minimized significantly. The initial configuration causes too much parasitic torques and forces due to the singular position. After the optimization, the optimized link lengths and the tool path minimized the parasitic torque and forces noticeably.
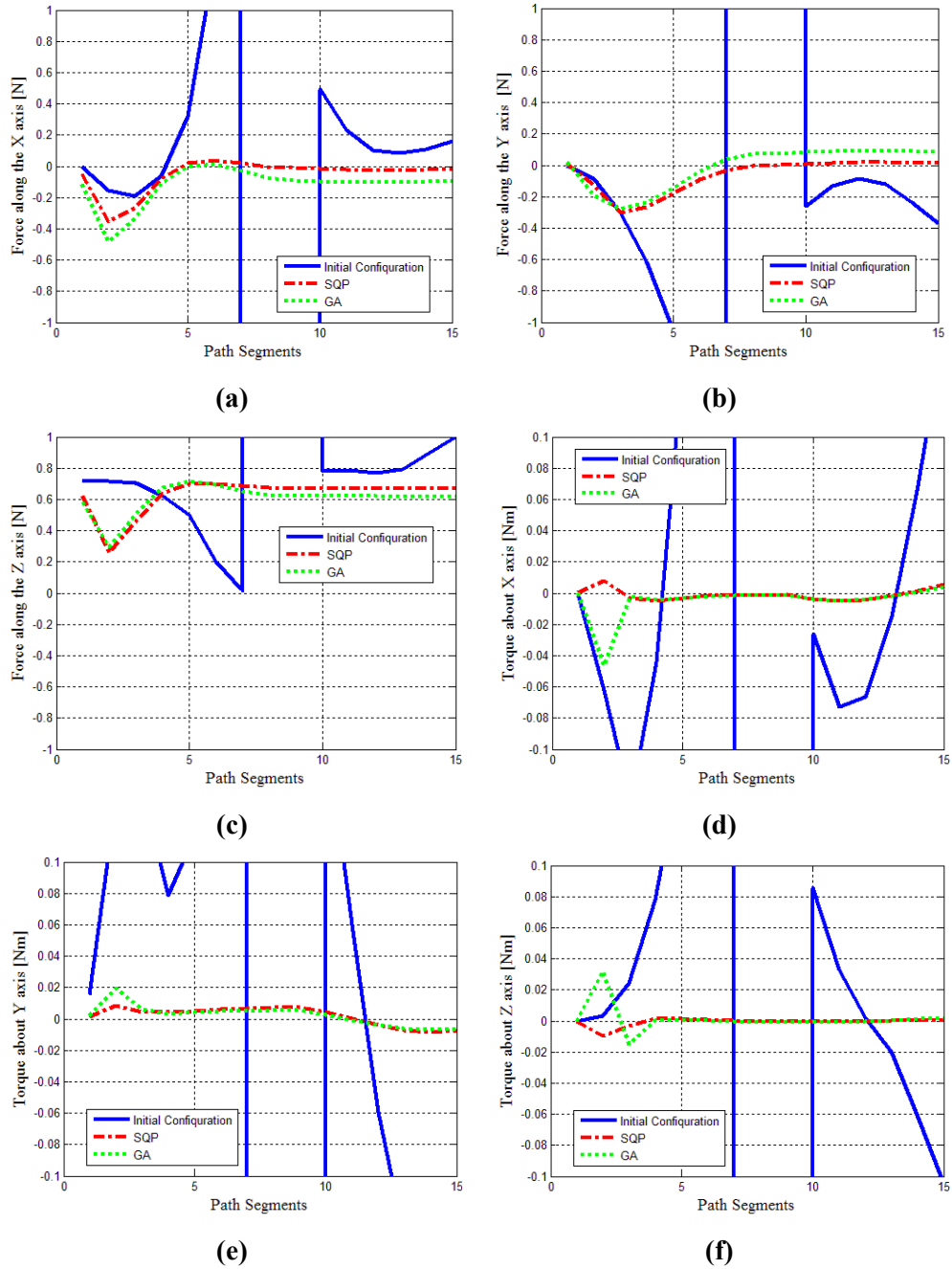
Figure 3.23: Parasitic Forces and Torques at the End-Effector

Finally, since the results from both algorithms are very close, it can be concluded that a global solution was found in the constrained search space. Also, required

computational time for the GA is nearly 10 times longer than that of SQP on the same computer.

3.8. DISCUSSION AND RESULTS

In order to show that the parasitic torques and forces felt by the user are reduced not only along the operation path but also over the entire control range, a deviation is added to the original operation path. The control system presented in the introduction chapter checks the position of the tip of the drilling tool when the dentist enters the control range. The control range is defined as cone navigation region where the larger base of the cone is attached to the initial position of original operation path and the tip point of the cone is placed to the implant hole. When the dentist approaches to the implant hole inside the cone navigation region, the passive guidance starts to navigate the dentist through the implant hole. The demonstration of the cone navigation region is achieved by adding a deviation to the implant operation path as shown in the Figure 3.24. The first 8 segments of the implant operation path are used to approach to the implant hole and the last 7 segments are taken to simulate the drilling operation with turning the tool around the implant hole. The cone navigation region is placed to first 8 segments. Also, a deviation is added to the implant operation. Thus, two different paths are obtained. The results of the optimization process are computed over these paths and the values of the objective function are given in the Figure 3.25.
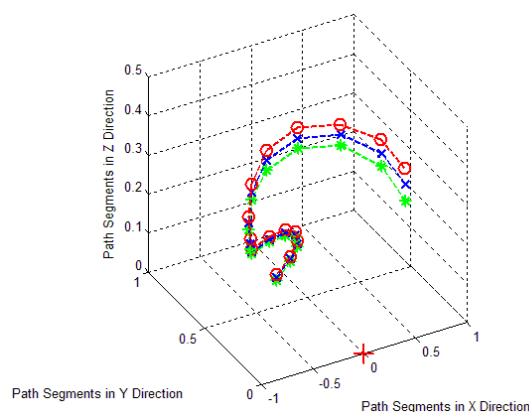
Figure 3.24: The Operation Path with Cone Navigation Region

56

(a)

(b)
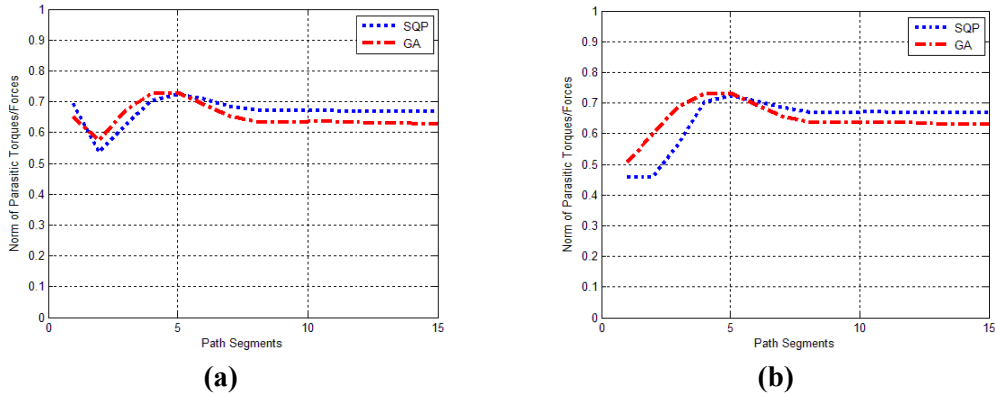
Figure 3.25: Optimization Results for Cone Navigation Region (a) Lower Path (b) Upper Path

The norm of the parasitic forces and torques along the lower and upper paths do not change too much. A little increase can be observed at the initial segments but the implant operation path still remains the same. This shows that the optimization results are applicable to the sample implant operation.

Another tooth is chosen to create a new operation path for computing the results of the optimization process along the new operation path. The tip point of the drilling tool is placed to a tooth in the CAD model and the orientation and position of the tip point is taken. Using the kinematic equations the same as in the path generation part, a new operation path is generated as shown in the Figure 3.26 (b).

(a)

(b)
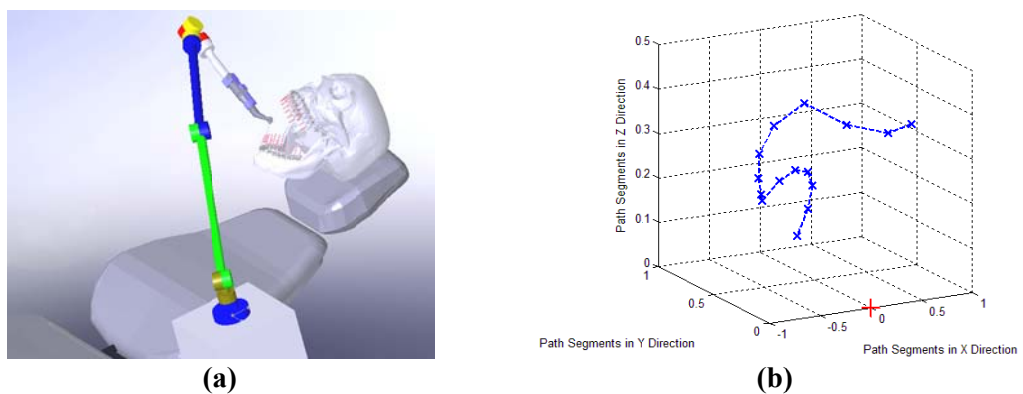
Figure 3.26: New Operation Path (a) The CAD Model (b) The Generated Path

The objective function is computed using the results of the optimization process over the new operation path. The norm of the parasitic forces and torques are calculated as shown in the Figure 3.27. The parasitic forces and torques are not increased while drilling other tooth using the optimized link lengths and the base coordinates. Furthest tooth is chosen to simulate the implant operation for the optimization process. Thus nearest teeth are reached easily.
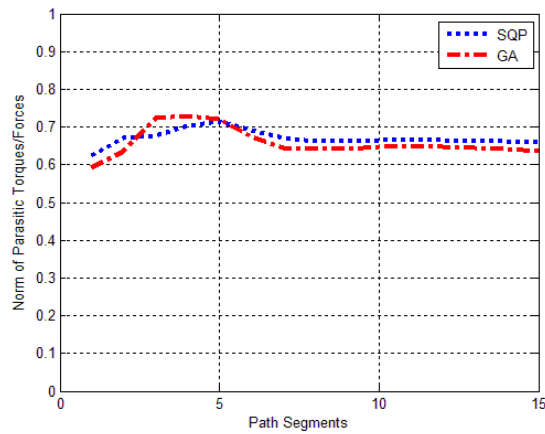
Figure 3.27: Result of the Objection Function for New Operation Path

Lastly, determination of the initial guess is very important to obtain global optimum results in the search space. After many trials, the initial guess is found which results to global optimum solution. Before finding the initial guess, the optimization algorithms are computed in many times and the results of the objective function and design parameters are observed. Here, in the Table 3.6, a branch of the initial guess is given. The values of the design parameters and the objective function at the left side of results show the outputs of SQP and the values at the right side of results show the outputs of GA.

Table 3.6: Initial Guesses and Results of the Design Parameters with Objective Function

Initial Guess	a_2 (mm)	d_4 (mm)	d_6 (mm)	X (mm)	Y (mm)	Z (mm)	Function Values
1	500	500	100	25	5	75	
Results	600/592.01	600/599.83	79.08/29.12	-120/-84.91	100/100	-192.80/-331.50	8.8399/8.502
2	400	500	200	100	50	200	
Results	600/507.71	600/495.02	20.96/139.3	-35.52/-114.1	58.6/100	-378.33/-243.72	8.6161/8.964
3	500	500	200	100	50	200	
Results	600 / 600	600/597.74	79.08/10.65	-120/-119.28	100/99.1	-192.79/-311.91	8.8399/8.424
4	500	400	100	100	50	50	
Results	600/599.28	600/598.54	45.34/19.81	-120/-112.65	0.0/99.23	-347.06/-318.64	8.7994/8.442
5	450	400	150	100	50	-50	
Results	600/563.21	600/497.34	17.70/156.6	-13.20/-103.8	59.6/100	-398.35/-336.94	8.5796/8.944

The results mostly show that the optimization algorithms are stuck to upper limits of the "a_2" and "d_4" and lower limits of the "X". The link lengths can be chosen higher than the upper limits but longer lengths cause bending problems. Also, the lower limit of "X" can be decreased but this results to place the base of the robotic arm onto the lap of the patient. The lower and upper values of the design parameters are chosen carefully to obtain physically realizable results. Moreover, the initial guess is found after many trials in order to obtain global optimum solution in the constrained search space.

3.9. OPTIMIZATION FOR A PATH IN THE CONE NAVIGATION REGION

The results obtained after the optimization process in the discussion section show that the optimum link lengths and the base coordinates produce lower parasitic forces and torques compared to the initial configuration even though a deviation is added to the implant operation path and another tooth is used to form a new operation path which is illustrated in the Figure 3.26 (b). The optimization results computed over the new operation path and deviated path indicate that the parasitic forces and torques do not change too much.

In this part, a new study is performed to show the change of the optimization results when a new path is generated using the control cone navigation. By using this new

path in the cone navigation region, the optimization is achieved once more and the changes in the design parameters are presented.
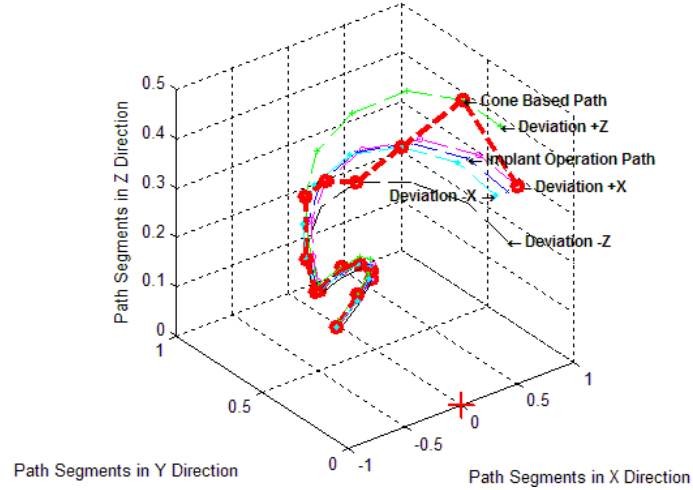
Figure 3.28: New Path in the Cone Navigation Region

In order to achieve the optimization process over a path in the cone navigation region, a new path is generated using the implant operation path used at the previous optimization process which is illustrated in the Figure 3.15. In the Figure 3.28, the blue path shows the implant operation path. Firstly, a deviation is added in the "+X" and "-X" directions. Then, the same deviation is added in the "+Z" and "-Z" directions. The deviation is added to the implant operation path to form a new path in the cone navigation region. As mentioned in the previous section, the implant operation path has 15 segments. The initial 8 segments are for approaching to the implant hole and the last 7 segments are for implant operation. Thus, the new path in the cone navigation region is formed at the initial 8 segments. The larger base of the cone, where the radius of the base is taken 10 cm, is placed to the first segment and then along the path the cone starts to get narrowed. The deviation for the implant operation segments is taken 1 cm. In the Figure 3.28, the pink path presents the deviated path in "+X" direction, the cyan path shows the deviated path in "-X" direction, the green path represents the deviated path in "+Z" direction, and the black path illustrates the deviated path in "-Z" direction. Finally, starting from

the first segment of the deviated path in "+X" direction, the new path in the cone navigation region is generated which takes the elements of each path in counterclockwise direction. The red path in the Figure 3.28 shows the new path in the cone navigation region.

The previous optimization results found for the implant operation path at the optimization results section are calculated over the new path in the cone navigation region. The results, as illustrated in the Figure 3.29, show that the parasitic forces and torques increase highly. It is observed that the robotic arm extends to the boundary of its workspace at the second segment of the deviated path in "+Z" direction. Thus, the deviation causes very high parasitic forces and torques. In order to reduce parasitic forces and torques over the new path in the cone navigation region, the optimization process is performed again.
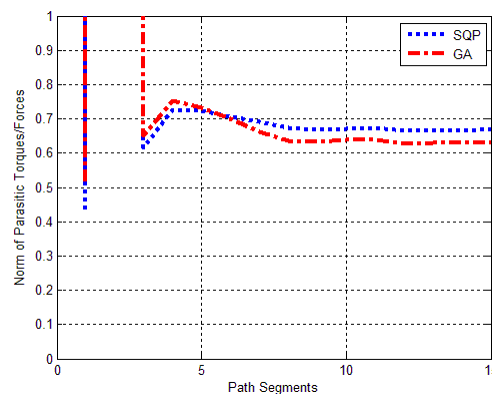
Figure 3.29: Previous Optimization Results Computed over New Path in the Cone Navigation Region

The initial guess and the upper and lower limits of the design parameters are presented in the Table 3.7. Differently from the lower and upper bounds of the first optimization process, this time, the lower bound of "d_6" is taken 20 mm and the lower bound of the "Z" coordinate is chosen 250 mm. When the lower bound of the "Z" is taken lower than this one, the lengths of the robotic arm needs to be longer and that is an unacceptable criteria.

61

Table 3.7: Lower and Upper Bounds of Design Parameters for New Path

Parameter	a_2 (mm)	d_4 (mm)	d_6 (mm)	X (mm)	Y (mm)	Z (mm)
Lower Bound	100	100	20	-120	-150	-250
Upper Bound	600	600	250	150	100	500

The optimization process is achieved once more and the results of SQP and GA are tabulated in the Table 3.8. The SQP gives the upper limit of the design parameters because the robotic arm reaches to the boundary at some segments of the new path in the cone navigation region. The results of the GA are slightly lower than the results of the SQP but the difference between the results is not much as in the results of the previous optimization. It is also observed that the results of the both algorithm is nearly the same. Again it is important to emphasize that the lengths of the link can be taken longer but this results to bending problems and it is not taken into consideration. Also, the coordinate of base in the "Z" direction is found a bit lower than the results of the implant operation path in order to reach the initial segments of the new path in the cone navigation region. The initial guess is changed in new optimization process, but this time the changes in the initial guess do not affect the results too much. The value of the objective function is nearly the same for both optimization algorithms.

Table 3.8: Optimization Results for New Path in the Cone Navigation Region

Optimization Results	a_2(mm)	d_4(mm)	d_6(mm)	X(mm)	Y(mm)	Z (mm)	Function Value
Initial Guess	500	400	150	25	5	75	
SQP	600	600	50.46	-120	100	-250	8.6747
GA	599.77	599.06	50.27	-119.86	99.92	-254.51	8.6828

The behavior of the objective function during the optimization process is shown in the Figure 3.30 for both algorithms.

(a)   **(b)**
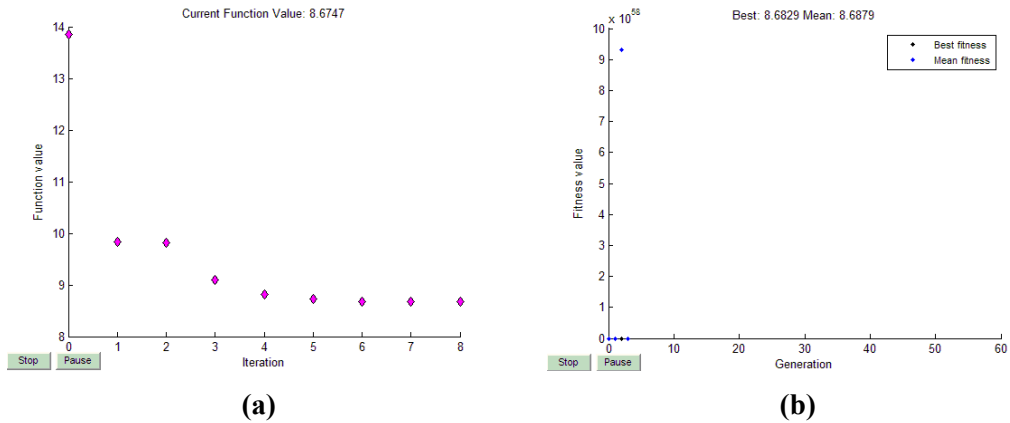
Figure 3.30: Behavior of the Objective Function (a) SQP (b) GA
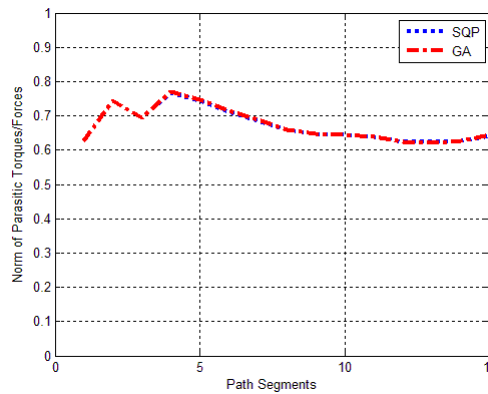
Figure 3.31: Objective Function for Optimization Results over the New Path in the Cone Navigation Region

The norm of the parasitic forces and torques are computed along the new path in the cone navigation region and the output is illustrated in the Figure 3.31. It is observed from the figure that the norm of the parasitic forces and torques are a bit increased in the 8 initial segments. The main reason of this rise is that the robotic arm is extending to reach some positions and these positions are getting closer to the singular positions. On the other hand, even though a deviation is added to the implant operation segments, the norm of the parasitic forces and torques are not increased too much. It is concluded from these results that the robotic arm is

approaching to the implant hole from the boundary of the workspace. Thus, within the workspace, the dentist can reach other teeth without encountering an increase at the parasitic forces and torques.

Finally, the objective function is computed over the deviated paths using the new optimized link lengths and the base frame coordinates. In the Figure 3.32, the norm of the parasitic forces and torques over the deviated paths is illustrated. From Figure 3.32 (c), it is observed that the effect of the deviation in the "+Z" direction is higher than the deviations in the other directions which causes from expending the robotic arm to the boundary of its workspace. Thus, in order to reach that position the robotic arm gets closer to the singular position and parasitic forces and torques increase. The deviation in the "+Z" direction only expands the boundary of the workspace. Therefore, "Z" coordinate of the base frame is calculated lower than the previous optimization results.
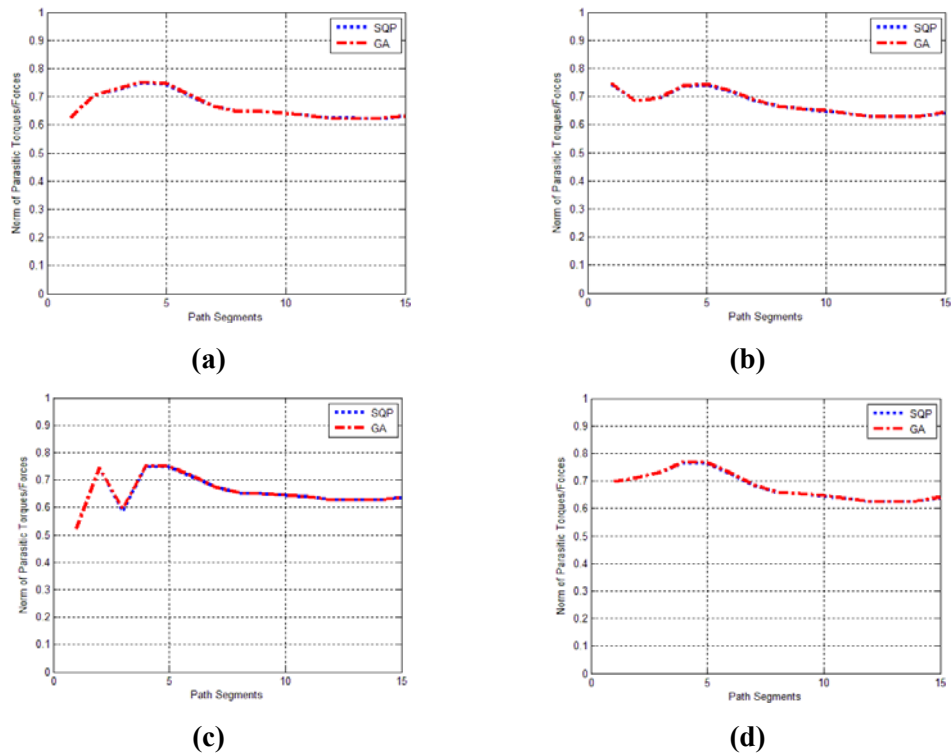
Figure 3.32: Objective Function Computed over Deviated Paths (a) "+X" (b) "-X" (c) "+Z" (d)"-Z"

The results of the new optimization process also showed that the optimization results of the implant operation path are enough to reach every tooth in any orientation. Finally, it can be concluded that a control system in the cone navigation region can be implemented to the implant operation path.

CHAPTER 4

MECHANICAL BRAKE DESIGN

4.1. INTRODUCTION

In this part of the thesis, the actuation of the passive haptic robotic arm is discussed. The most important part of a robotic system is the actuator which actually does the main task. There are actuators like electric, electro-mechanic, hydraulic or pneumatic that both mainly convert the energy into some kind of motion and apply it to the system. One of the most popular actuation systems, electric motors are generally divide into two main groups which are AC motors and DC motors. AC induction motors are the most common motors that are used in the industrial applications although they have difficulties in controlling the motor compared to DC motors. AC motors are not acceptable for servo applications but DC motors are [62]. Instead of using AC induction motors, brushless or brush DC motors are more suitable for servo applications since they are easily implemented to the control applications that require feedback control. Also, DC motors supply higher power relative to their smaller size. DC motors can be easily controlled with analog or digital feedback signals using the appropriate driver for the motor.

Figure 4.1: A Sample DC Motor [63]

Stepper motors are also available brushless electric motors which can be used to control the position of the motor accurately without using any feedback loop. But in high speed applications, required torque decreases due to the increase in the stepper motor's speed. Thus the stepper motors are not suitable for torque control applications.

A hydraulic actuator uses pressurized hydraulic fluid to actuate the hydraulic cylinders. A typical hydraulic system generally includes three parts: A hydraulic cylinder to drive the machinery using the pressurized hydraulic fluid, a hydraulic pump which is driven mostly by an electric motor and finally the valves, piping etc. to complete the system. Hydraulic actuators use the Pascal's Law to drive the system. By using a simple hydraulic cylinder, very high forces can be obtained. In spite of obtaining high force values, it is hard to implement the hydraulic system to a robotic system compared to a DC motor which is very small in size and easily controllable.

Figure 4.2: A Sample Hydraulic Actuator [64]

In pneumatic actuators, pressurized air is used instead of hydraulic fluid. Just like in the hydraulic actuator, the pneumatic actuators consist of a cylinder, a piston and valves. With small input force to a successfully designed pneumatic system, a small car can be lifted. Larger forces require larger pistons, valves and piping system. Therefore, the pneumatic systems are also not preferred for the robotic systems.

4.2. ACTUATION TYPES

Today, in a large scale of different spheres from industrial manipulators to a small robotic arm, the actuation of the robotic devices are generally provided using electric motors. The main aim of these robotic arms is to complete the given task actively such as carrying a load, spraying an automobile, drilling a hole onto an engine block etc. using the electric motors or other actuation systems mentioned above. On the other hand, with the widespread usage of the haptic devices in medical training, virtual reality applications, and educational purposes, it is noticed that the motion of the haptic devices is given directly by the user and by using a virtual environment the movement of the haptic device can be restricted [65]. Also, the safety issues of the haptic devices, which are used in surgical operations, rehabilitation, and interaction between humans and the robotic arms, are more important than the industrial robots. The actuators that supply power to move the system can cause undesirable results even though complicated control schemes are implemented. Therefore, especially in haptic devices, the passive actuators which are only used to restrict the motion applied by a human user can be preferred instead of active actuators as mentioned in the introduction part of this chapter to provide motion to the joints [66].

As introduced it the first chapter, the main goal of this research is to develop a passive haptic robotic arm as a part of dental surgical aid system. With the help of the haptic feedback, the dependence to the dentist skills will be reduced and the accuracy of positioning in the implant operation will be increased. Thus, the overall safety of the implant operation will be raised. The proposed system will guide the dentist during the implant operation with haptic feedback. Consequently, instead of using active feedback which carries the dental tool directly to the desired implant position, the movement of the dental tool is left to the dentist and the passive feedback is preferred as the actuators in the robotic arm to guide the dentist during the overall operation. In the passive feedback, the passive actuators start to apply braking torques to the joints to prevent the user go away from target position, when

the tip point of the dental gets closer to this position. Main aim of the passive feedback is to keep the dentist on the operation path while the manipulator is moved by the help of the dentist. As examples of the passive actuators, brakes that include electrorheological (ER) or magnetorheological (MR) fluid are introduced.

4.3. ER AND MR BRAKES

The brakes including the ER or the MR fluids are a good choice for a passively actuated system, because they do not supply energy to the system, but they only dissipate it.

Magnetorheological (MR) fluid is a type of smart fluids which can be controlled when subjected to a magnetic field because the viscosity of the MR fluid increases seriously. Another controllable fluid like the MR fluid is electrorheological (ER) which is affected from electric field. Both the MR and the ER fluids include micrometer scaled iron particles that are usually in a carrier fluid such as oil or water based solution [67] as in the Figure 4.3 (a).

(a)

(b)
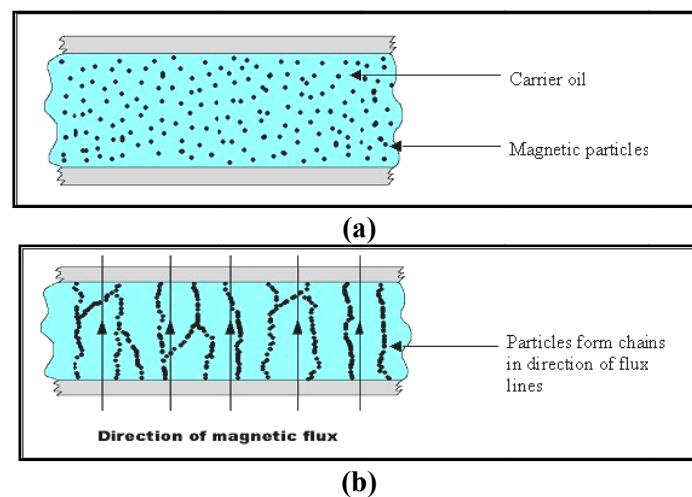
Figure 4.3: Behavior of the MR Fluid under Magnetic Flux (a) Off State (b) On State [68]

The micrometer scaled iron particles become polarized when the magnetic or electric field is applied to the fluid. The iron particles start to align along the direction of the applied field due to the polarization as shown in the Figure 4.3 (b). This alignment causes to form chain like structures and these structures increase the viscosity of the fluid. In "off-state", the fluid flows like low viscosity oil but in "on-state" it changes to viscoelastic solid. The main advantage of these controllable fluids is their quick responses to the magnetic or electrical flux. The ER fluids generate 3 to 5 kPa yield strengths due to an electric field of 3 to 5 kV/mm. On the other hand, the MR fluids produce 50 to 100 kPa yield strengths for a magnetic field of 150 to 250 kA/m [67, 69]. The difference between the values of the yield strengths makes the MR fluids advantageous for the force and torque requirements for a passive actuator design of a haptic device. The MR fluid can be implemented as a passive actuator either by limiting the flow of the fluid or restricting the motion of the plates which are moving parallel relative to the fixed one as shown in the Figure 4.4 [70].
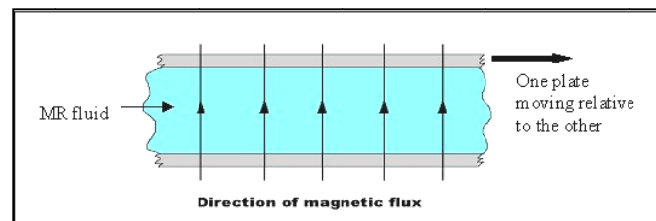
Figure 4.4: MR Fluid between Parallel Plates [68]

When the magnetic flux is applied to the MR fluid, the viscosity of the MR fluid increases and thus the flow of the MR fluid decreases. The MR brakes and clutches are designed using two parallel plates or two concentric cylinders that include MR fluid between them. The increase in shear stress between the cylinders or plates starts to restrict the motion of the MR brake.

In the literature, there are many applications of the ER and MR fluids available. By using the MR fluid, a small MR brake was designed to be used in force feedback

glove for virtual environments as in the Figure 4.5 (a) [71]. The designed MR brake is about 25 mm in diameter, has a weight of 84 g and gives an output torque of 899 Nmm. The main design advantage of this MR brake is an increase at serpentine flux path that pass through the MR fluid using steel and aluminum rings. Six brakes are produced to implement to the haptic glove which is called the MR glove as in the Figure 4.5 (b). The results showed that the produced MR glove can easily be used for pick and place operations of the virtual objects [72].

(a)

(b)
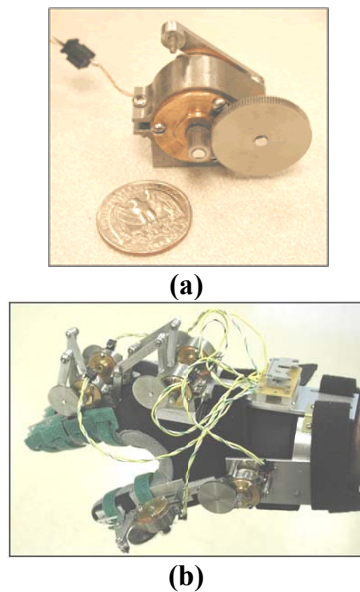
Figure 4.5: (a) MR Brake and (b) MR Glove [72]

Another research has been conducted to increase the output torque values. The main aim of this research is to increase the interaction between magnetic flux and MR fluid as shown in the Figure 4.6. The new shape of the flux path results to more compact and powerful MR Brake. The output torque of the new MR Brake is approximately 10.9 Nm. The brake is about 65 mm in diameter. The MR brake is put in a simple 1 DOF haptic device to apply virtual wall collision experiments. The results showed that the new design gives more output torque values than the available designs [73, 74].
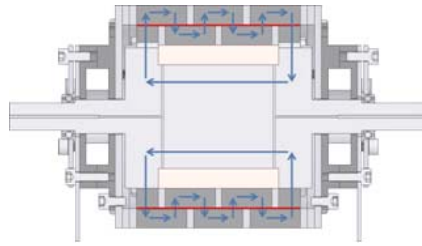
Figure 4.6: Rotary MR Brake with Serpentine Flux Path [73]

Just like the MR brakes, the ER brakes are also developed by using ER fluids. The ER brake is designed to implement a passive haptic display as shown in the Figure 4.7. The brake is 156 mm in diameter, 135 mm in width and has a weight of 2.6 kg. The output torque produced by ER brake is approximately 1.3 Nm [75]. Beside the size and the output torque of the MR brakes, the ER brakes are not suitable to use in lightweight haptic devices.

Figure 4.7: Developed ER Brake [75]

The application of the MR brake to a haptic device is shown in the Figure 4.8. The test results showed that the MR brakes are very suitable for the virtual reality applications. Applying different currents, the forces are generated using control signals for the user to feel these forces [76].

Figure 4.8: MR Brake with Test Setup [76]

A passive haptic interface which will be used in dental implant surgery using MR brakes are designed and manufactured by Senkal et. al. in [77]. The produced MR brakes with an output torque of 10.9 Nm are mounted to the first three axes of a 6 DOF robotic arm as shown in the Figure 4.9. Using the implemented control system, the hole drilling experiments for an implant operation are carried out and the errors at the X, Y, and Z axes are reported. The results of this system also showed that the passive actuation can be used as an alternative to the active actuation.

Figure 4.9: Passive Haptic Interface [77]

The main disadvantage of passive haptic interfaces including ER/MR brakes is that there is no pull back action for the manipulator if the tip point of the manipulator goes inside the virtual walls [77]. Although the passive actuators are safer devices

73

than the electric motors, they have serious limitations about generating forces when the virtual tool touches the objects with different shape and stiffness in the simulation environment. The mentioned problem is investigated in detail in [65] and a new actuation approach is demonstrated.

In the light of this information, a new brake design which is working mechanically is conducted instead of the ER and the MR brakes. At the proposed design the braking will be held using the advantage of the friction of the mechanical components. The mechanical components are driven by a DC motor but the braking action is achieved by the help of the braking pads which interact with a rotating surface which is caused to stop. The main purpose of this design is to prevent pull back problems that occurs when the tip point of the manipulator touches to different objects with variable stiffness and sizes. The new design consists of a new approach that allows the control system to understand if the tip point is going inside or outside of the virtual wall. This new approach lets the user to take the manipulator away from inside of the virtual wall. The proposed system is expected to produce 5 Nm torque output using the friction element. The new design is supposed to have a size about 90 mm in diameter and 100 mm in width and a weight of nearly 1 kg. The details of the new design, the calculations of the mechanical components and the implementation of the new design are presented. Also, the developments that are applied to the new design are introduced. Finally, a developed design of the mechanical brake is presented.

4.4. MECHANICAL BRAKES

Generally mechanical brakes store the rotation energy with the help of the friction element. The opposite version of the brakes is the clutch. The clutches use the friction element to transfer the rotation energy. Brakes are commonly applied to the rotating part of the mechanism. To analyze the brakes simply, two cylindrical parts rotating with angular velocities ω_1 and ω_2 are considered. In order to bring the parts to the same speed, a clutch or brake between them has to be engaged. With the help of the friction element, the kinetic energy is converted into heat energy. The

value of transmitted torque depends on coefficient of the friction element, the actuation force, and, size and shape of the brake/clutch. In order to design a mechanical brake, an introduction to the types of the frictional brakes has primary importance.

The most common version of the mechanical brakes use friction elements which are generally called "shoe" or pad" with a plain wear surface. In this type of brakes, friction elements are always stationary and the rotating part has a wear surface. Due to the interaction between them, the torque can be transmitted. The internal pivoted shoe brakes, shown in the Figure 4.10 (a), are the one of the common configurations with an operation mechanism that actuates the pivoted shoes outward and stops the rotating part. Another version of the pivoted shoe brakes acts externally as shown in the Figure 4.10 (b) with the help of a lever system driven by an actuation system [78].

(a)   (b)
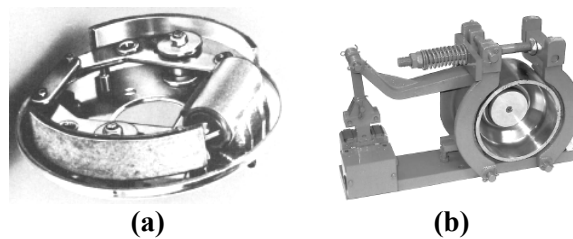
Figure 4.10: (a) An Internal Pivoted Shoe Brake (b) Externally Pivoted Shoe Brake [78]

Another version of the brakes is the band type brakes which is the simplest and less expensive one than the other shoe brakes. As shown in the Figure 4.11, a band with frictional element inside of the band is wrapped around the rotating drum. If forces applied to the ends of the braking band with different values, the restraining torque can be obtained [78].

75

Figure 4.11: A Band Type Brake [79]

Most popular version of the frictional brakes is the disk type brakes which are used on automobiles, aircrafts, industrial applications, bicycles and motorcycles as illustrated in the Figure 4.12. Their main advantage is their great heat dissipation due to their open structure. On the other hand, they require larger activation force than the other braking devices [78, 81].

Figure 4.12: Disc Type Brake [80]

The last type of the frictional brakes is the cone type brakes as shown in the Figure 4.13. Instead of two disks as in the disc type brake, the cone brake uses two conical surfaces with friction element between them to transmit the torque. The cone brakes produce greater torque with a smaller activation force relative to the disk brakes due to their wedging action and enlarged contact area. While designing a cone type brakes, the value of the cone angle has to be chosen carefully since small cone angles cause the inner and outer cones to be wedged.
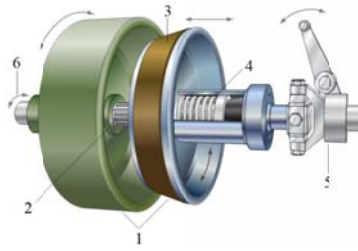
Figure 4.13: The Cone Brake [82]

In the Figure 4.13, the outer cone is green part and the inner cone is blue part where both of them are numbered as 1. The shaft is numbered as 2 where the inner cone slides on it. Number 3 shows the frictional element attached to the inner cone. The spring, numbered as 4, pulls the inner cone after the activation force is taken off. The number 5 is the actuation mechanism of the cone brake and the number 6 shows the direction of the rotation.

Up to now, types of the frictional brakes are introduced. All of the brakes mentioned above need an actuation mechanism to activate the brake to restrain the rotation torque. Depending on the operation areas, actuation mechanisms can be categorized as expanding, centrifugal, magnetic, hydraulic, pneumatic, and electrical [81]. Internally pivoted shoe brakes can be actuated with the help of centrifugal effect. Disc brakes attached to a bicycle rim are started to be used commonly in modern mountain bicycles which are actuated with hydraulic system as shown in the Figure 4.14.

Figure 4.14: Disc Type Brake with Hydraulic Actuation [83]

77

Electromagnetic (EM) brakes as shown in the Figure 4.15 are actuated by electric current, but mainly they transmit torque mechanically. The EM brakes have three parts; an armature, a coil in a shell, and a hub. The coil is energized when the electric circuit is given to the system. The energized coil generates a magnetic flux and this causes the armature to compress the friction material connected to the hub [84]. The rotating shaft is connected to the hub. When the electric circuit is activated, the torque is transmitted. The EM brakes can be used as a passive actuator at the haptic device but they are generally used to stop the rotor after the power of the DC or AC motor is cut off. It is not possible to transmit the different braking torques even if different electric current input is applied. The EM brakes work as on-off systems and are not suitable for the systems that require the control of the braking torque.

Figure 4.15: Anatomy of an Electromagnetic Brake [84]

4.5. DESIGN OF THE FIRST MECHANICAL BRAKE

In the previous section, the types of the frictional mechanical brakes are briefly introduced. In order to design a frictional brake as a passive actuator, the type of the frictional brakes has to be chosen carefully. The cone type brakes produce great amounts of torque for a small amount of axial force. In reveal of the fact that design

78

process starts with choosing the type of the mechanical brake which is chosen as the cone type brakes.

A very common use of the cone brakes is encountered in the braking systems of mountain bikes as shown in the Figure 4.16 (a), called as the coaster brake. The coaster brake simply works when the pedals of the bicycle are turned backward. Then the coaster brake is activated and the bicycle stops. Hence, they are also called back pedal brakes or foot brakes.

(a)

(b)
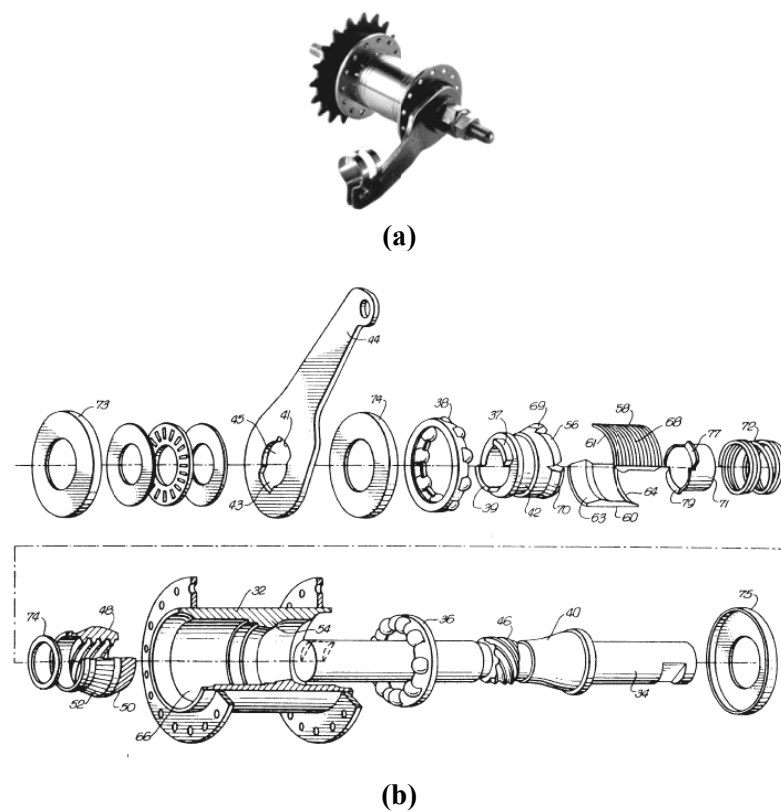
Figure 4.16: (a) The Coaster Brake [85] (b) An Exploded View of the Coaster Brake [86]

In order to understand the main working principle of the coaster brake, the parts of the brake have to be introduced in detail. The coaster brake has both clutch and braking action inside a hub, numbered as 32 in the Figure 4.16 (b), which is

connected to freewheel. When the bicycle is pedaled forward, the sprocket, numbered 5 in the Figure 4.17, drives the screw, numbered as 46 in the Figure 4.16 (b), with the help of the key hole numbered as 34 in the Figure 4.16 (b). The screw drives the double action driver, numbered 6 in the Figure 4.17, along the shaft. Thus the double action driver undertakes the clutch role to transmit the input torque to the hub. When the pedaling is reversed, the double action driver starts to move in the opposite direction and pushes the braking pads, numbered as 7 in the Figure 4.17, which are pressing against the hub to produce braking torque. The material of the inside surface of the hub is generally steel yet the material of frictional braking element can be selected as brass or steel. The spring between double action driver and the stabilizing arm, numbered as 2 in the Figure 4.17, separates the double action driver from stabilizing arm when the activation force is removed.
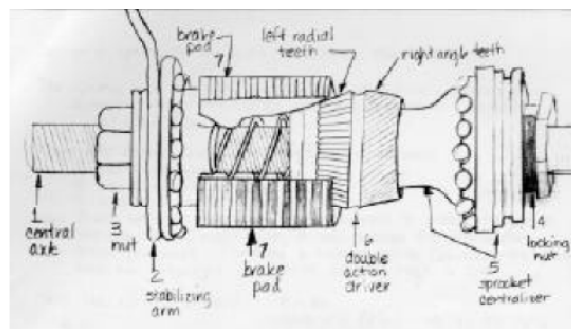
Figure 4.17: Hand Drawn Sketch of the Coaster Brake [87]

As stated above, the important parts of the coaster brake are the shaft, which carries all the parts on it, the double action driver, which does the clutch and braking action, the braking pad, which produces braking torque against the hub, the hub, which combines all parts together and does the braking action, and the sprocket, which gives motion to the double action driver.

The design of the first mechanical brake (FMB) is inspired from the working principle of the coaster brake. The parts mentioned above are redesigned using the

same working principles and are implemented to the first mechanical brake. The brake is modeled using the Solidworks® software.
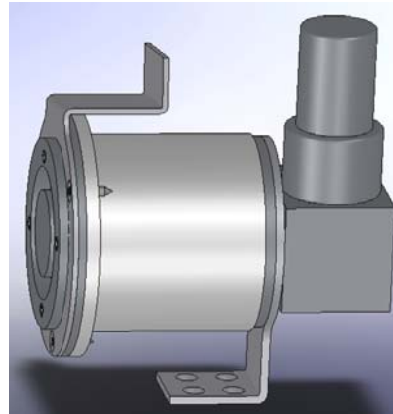
(a)
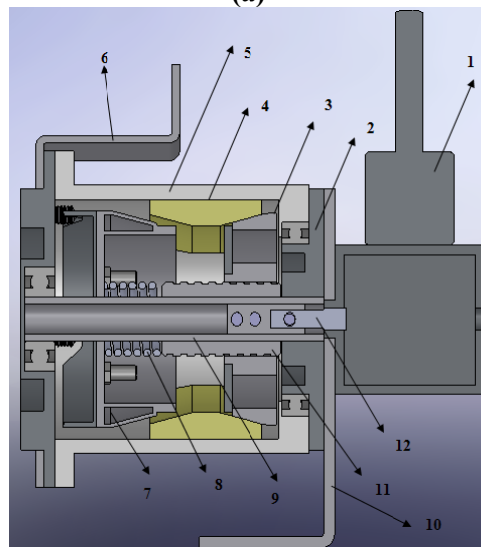
(b)

Figure 4.18: (a) The CAD Model of the FMB (b) Section View of the FMB

The actuation of the FMB is provided using DC motor, numbered as 1 in the Figure 4.18 (b). The system and the DC motor are fixed to ground with the help of the part numbered as 10 in the same figure. Instead of giving the motion by turning the shaft as in the coaster brake, the shaft, numbered as 9, is mounted to part 2 with interference fit and part 2 is fixed to the ground using the part 10. The activation force for the brakes is given via power screw, numbered as 11, which is actuated by

the DC motor using part 12. There is a gap on the shaft, as shown in the Figure 4.19, which allows the DC motor to turn only 90 degrees when activated. The pins are used to transmit the motion from DC motor to the power screw.
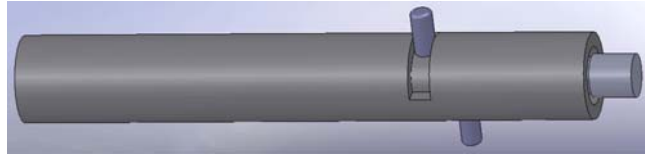
Figure 4.19: Details of the Shaft and the Actuation

After the DC motor is activated, the power screw drives the motor side conical surface, numbered as 3, to activate the brake pads which is numbered as 4. There is also user side conical surface, numbered as 7, which helps the brake pads to move upwards. The conical surfaces force the brake pads to press against the outer cap, numbered as 5, which generates braking torque. The part 8 is the spring which is used to disengage the brake when the power screw is driven reverse.

The major difference of this design from the coaster brake is to utilize the user as force supplier. Instead of using a double action driver as in the coaster brake, the conical surfaces are divided into two different parts in the FMB. One of these parts, numbered as 3, is driven by the DC motor and the other part, numbered as 7, is moved by the help of the user. A properly designed shape, which is demonstrated in the Figure 4.20, is used to transfer the force applied using the arm, numbered as 6, to the user side conical surface.

Figure 4.20: "V" Shape Connected to User Side Conical Surface

82

The system is activated by the DC motor and motor side conical surface starts to move in the direction 1 as shown in the Figure 4.21. The motor side conical surface pushes the braking pad upwards and the initial braking action starts. When the user continues to apply force to the arm, the set screw with a ball attached to one end of the screw which is demonstrated in red circle in the Figure 4.21, starts to slide on the "V" and pushes the user side conical surface towards the braking pads in the direction 3. Thus, the braking action is completed with the user supplied force.
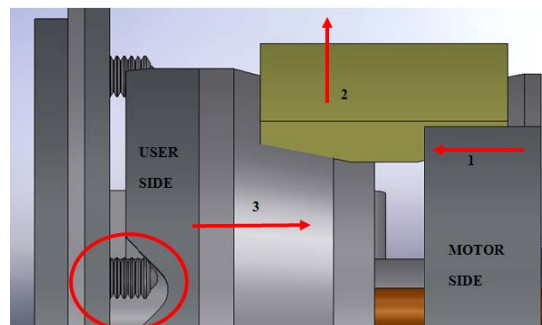
Figure 4.21: Working Principle of User Side Conical Surface

Using this new approach, one can be utilized from the force applied by the user in the braking action. It is supposed that at the end of one side of the "V" shape, the brake is locked and the user cannot rotate the arm anymore. Also, using a potentiometer or similar device, the position of the user's hand can be determined and control of the brake can be achieved as fully functional. Using the position of the arm and the "V" shape effectively, the control system can determine where the user is going. In the virtual environment, the user rotates the "V" shape until one side of the "V" shape reaches to virtual wall. After that, the motor side conical surface is activated and the initial braking is achieved. The initial braking prevents the user side conical surface to rotate and initializes it to slide along the shaft. Thus, the set screw starts to climb the "V" shape and pushes the user side conical surface towards the braking pads using applied force from the user. When the set screw reaches to the end of one side of the "V" shape, the maximum braking torque is produced and the user feels the virtual wall. While the user starts to rotate in reverse

direction, the DC motor holds the motor side conical surface at the initial braking position until the set screw reaches to the other side of the "V" shape. Thus, the movement between the sides of the "V" shape provides the control algorithm to understand where the user is going. Consequently, this new design prevents the pulling back problem encountered in the MR brakes.
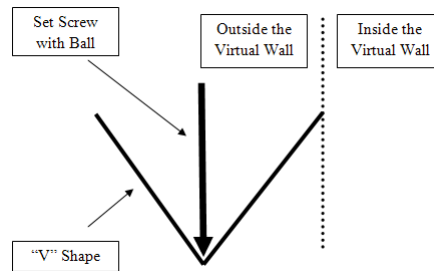
Figure 4.22: Working Principle of "V" Shape

4.6. CALCULATIONS OF THE FMB

The size of conical surfaces and the braking pads has to be calculated carefully to design a properly working brake. At first, calculations of the activation force for conical surface are introduced.
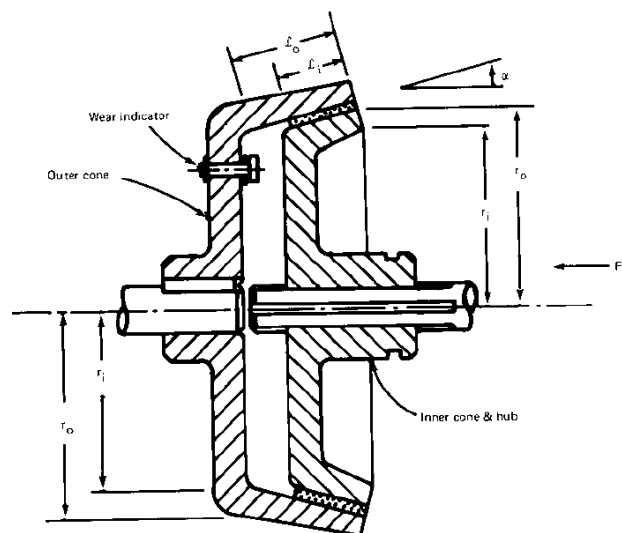
Figure 4.23: Geometry of the Cone Brake [78]

84

The geometry of the cone brake is presented in the Figure 4.23. The derivation of the equations for calculation of conical surface is adapted from [78] and [81]. The inner and the outer cones are assumed to be as concentric and rigid. Then, the amount of worn occurred during the engagement of the brakes is taken as,

$$\delta = kpr \tag{4.1}$$

where "p" is the applied pressure, "r" is radius of the point where the pressure "p" acts and "k" is the proportionality constant. The maximum pressure at the minimum radius is written as,

$$\delta = kp_{max}r_i \tag{4.2}$$

Equating the equations 4.1 and 4.2 gives the following as,

$$p = p_{max}\frac{r_i}{r} \tag{4.3}$$

Thus, the activation force can be calculated by taking the integral from the inner cone to the outer cone and putting the equation 4.3 into it as,

$$F_{act} = \int_A (p \sin \alpha + \mu_{cone} p \cos \alpha) da \tag{4.4}$$

where the area from inner surface to the outer cone is taken as,

$$da = 2\pi r dl = 2\pi r \frac{dr}{\sin \alpha} \tag{4.5}$$

The result of the integration is found as,

$$F_{act} = 2\pi p_{max} \left(1 + \frac{\mu_{cone}}{\tan \alpha}\right) r_i(r_o - r_i) \tag{4.6}$$

The equation for activation force of the conical surfaces is derived. Now, the torques exerted by the braking pads and the contact length of the braking pads are to be calculated. The calculations of the braking pads are adapted from [88].
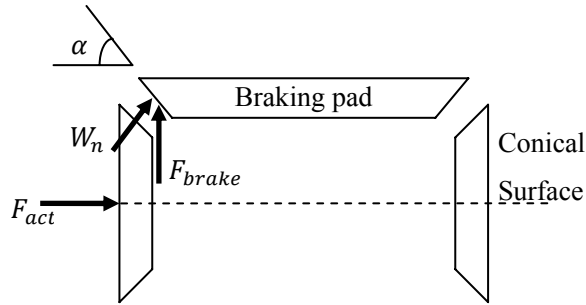
Figure 4.24: Forces on the Braking Pad

The forces that are used in the calculations of the braking pads are shown in the Figure 4.24. The activation force applied to the conical surfaces to the braking pads causes a frictional force on the braking pads as,

$$W_n = \mu_{brake} F_{act} \sin \alpha \tag{4.7}$$

where "μ_{brake}" is the coefficient of the friction element. Then the force pushing the braking pads upwards to generate braking torque is calculated as,

$$F_{brake} = \mu_{brake} F_{act} \sin \alpha \cos \alpha \, N_f \tag{4.8}$$

where "N_f" is the number of the forces acting on the braking pad. After that, the torques produced by the braking pads can be found as,

$$T = F_{brake} R_{pad} N_p \tag{4.9}$$

where "N_p" shows the number of the braking pads and "R_{pad}" is the radius of the contact point to the hub. The contact length of the braking pad is given as,

$$L_{pad} = \frac{\pi}{4} R_{dim} \tag{4.10}$$

The power screw that transmits the supplied force by the DC motor to the motor side conical surface is calculated. The necessary formulations for the power screw are taken from [81].
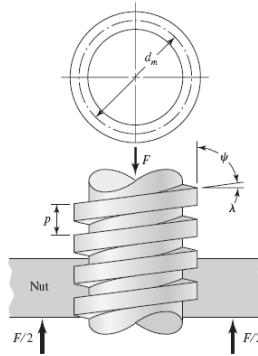
Figure 4.25: Portion of a Power Screw [81]

In the Figure 4.25, a portion of a square threaded power screw with a single thread is shown. Here, "p" is the pitch, "d_m" is the mean diameter, "λ" is the lead angle, and "ψ" is the helix angle. A compressive force "F" is acting on the screw axially.
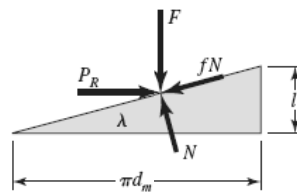
Figure 4.26: Force Diagram When Lifting the Load [81]

When raising the load, the force equilibrium of a single threaded of screw, as shown in the Figure 4.26, can be written as,

$$P_{rise} = \frac{F(\sin \lambda + \mu_{screw} \cos \lambda)}{\cos \lambda + \mu_{screw} \sin \lambda} \tag{4.11}$$

Then, after the equation 4.11 is divided by $\cos \lambda$ and the relation $\lambda = l/\pi d_m$ is put into it, the required torque to lift the load can be calculated by multiplying the equation 4.11 with the mean radius as,

$$T_{screw} = \frac{F d_m}{2} \left(\frac{\pi \mu_{screw} \, d_m + l}{\pi d_m - \mu_{screw} l} \right) \tag{4.12}$$

The equations are derived to calculate the important parts of the FMB. The calculations of equations are done easily by using the engineering calculation tool, MATHCAD®. Starting from the force provided by the user, the necessary values are computed. It is assumed that the user is applying a torque of 12 Nm to the arm, numbered as 6 in the Figure 4.18 (b). Then the activation force for the user side conical surface produced by the user can be calculated using the power screw equations by reversing the equation 4.12 as,

$$F_{user} = \frac{2T}{d_m} \left(\frac{1 - \mu_{screw} \tan \lambda}{\mu_{screw} + \tan \lambda} \right) N_{user} \tag{4.13}$$

where "N_{user}" is the number of forces acting from the user side which can be seen in the Figure 4.20 (b). The lead angle is taken "$\lambda = \pi/4$" for not a self-locking screw as seen in the Figure 4.27. The main aim of the choosing the lead angle as "$\pi/4$" is to create a surface on where the set screw with ball slips easily. Also, it is clear that the conical surface at the user side moves as same distance as the set screw climbs the inclined surface. The coefficient of the friction is taken from [81] as $\mu_{screw} = 0.25$ where both parts are made of steel, the mean diameter is chosen as "$d_m = 70 \, mm$", and, then the activation force applied by the user is calculated using equation 4.13 as,

$$F_{user} = 51.4 \, N$$
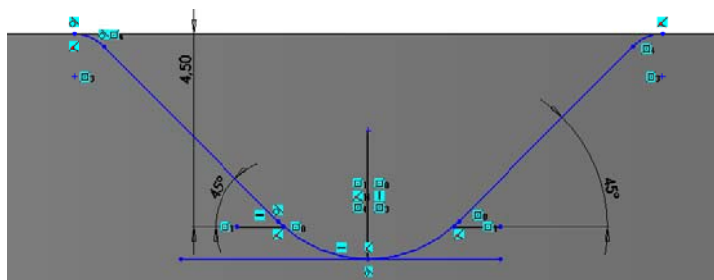
Figure 4.27: Details of the "V" Shape

Now, the activation force for the conical surface is calculated. The force is calculated using the equation 4.6. Recall the equation 4.6,

$$F_{act} = 2\pi p_{max} \left(1 + \frac{\mu_{cone}}{\tan \alpha} \right) r_i(r_o - r_i)$$

Here, the most important parameters of this equation are the values of the "μ_{cone}" and "α". The figure taken from [78] is used in the determination of these parameters. From the figure, it is obtained that if "μ_{cone}" and "α" are taken from the regions 2 and 4, then a retraction force is required to disengage the cone brake. The regions 3 and 5 have a greater torque to activation ratio and should be eliminated in the design of the brakes. The values of the "μ_{cone}" and "α" are taken from the region 1 where no retraction force is required [78].
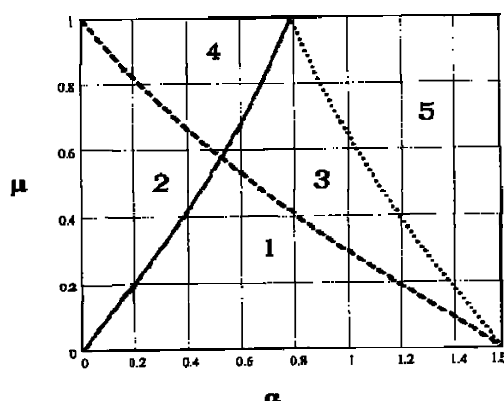
Figure 4.28: Design Region in μ, α Plane for the Cone Brake [78]

The angle of the conical surface, "α", is taken as 15 degrees and the corresponding coefficient of the friction is found from the Figure 4.28 as $\mu_{cone} = 0.2$. The maximum pressure is taken as "$p_{max} = 0.7\ MPa$" when the material is chosen as sintered metal [81]. The radiuses of the outer cone and the inner cone are $28\ mm$ and $25\ mm$, respectively. Thus, the activation force required for the conical surface is computed using the equation 4.6 as,

$$F_{act} = 576\ N$$

In order to acquire the necessary input torque from the DC motor, the size of the power screw has to be determined carefully. Thus, a square-threaded screw with 4 threads and a pitch of 8 mm is chosen. Recalling from the Figure 4.19, the shaft only lets a 90 degrees of rotation, thus when the DC motor activated, the power screw drives the conical face 8 mm forward. The mean diameter is taken as $d_m = 20\ mm$ and the coefficient of friction is chosen as "$\mu_{screw} = 0.08$". Then, using the equation 4.12 the torque supplied by the DC motor is calculated as,

$$T_{screw} = 0.776\ Nm$$

In the calculation of the torque value, the net force is found by subtracting the applied force by the user "F_{user}" from the activation force of the conical surfaces "F_{act}" as,

$$F_{net} = F_{act} - F_{user}.4$$

where "$N_{user} = 4$" is taken which is introduced in the equation 4.13 as the number of the forces acting by the user. As seen from the Figure 4.20, the force applied by the user acts from 4 points. It is chosen as "4" to move the conical face directly on the shaft.

The braking torque exerted to the hub is calculated using the equation 4.9 as,

$$T = 5.6 \, Nm$$

where "$R_{dim} = 32 \, mm$" is taken. Thus, the contact length of the braking pad is found as,

$$L_{pad} = 25 \, mm$$

The contact length is shared between conical surfaces of the user side and the motor side equally as 12.5 mm. The 8 mm of this length is driven by power screw and 4.5 mm of it is supplied by the user. Therefore, a special square-threaded screw with 4 threads and a pitch of 8 mm is designed to acquire the necessary motion from the DC motor.

The sizes of the necessary parts are determined. The parts are designed using the results above and they are used in the CAD model as shown in the Figure 4.18 (b).

4.7. THE PRODUCTION AND IMPLEMENTATION OF THE FMB

In the calculations, materials of the some parts are introduced but it is worth to give more details about the materials of the important parts. The shaft is holding all system on it though it has to have enough stiffness. The power screw and the user side conical surface are sliding on the shaft therefore the surface quality is very important. Also, the position of the gap is important to transmit torque efficiently to power screw from the DC motor. Thus, it is produced from steel with increased surface quality. The conical surfaces with the braking elements are manufactured from steel as used in the calculations. In order to reduce the weight of the outer cap, it is produced using two different materials. The outer cap is made of derlin and a steel ring with 1 mm thickness is located into it with interference fit to produce necessary friction for braking torque. The remaining parts are made of aluminum to decrease the weight of the system. The technical drawings of the each part are prepared. An exploded view of the FMB is given in the Appendix D.1. The parts mentioned up to now are manufactured using CNC machines. In the Figure 4.29,

the CAD model and the assembled brake are demonstrated. The FMB has a weight of 1022 g without the DC motor.
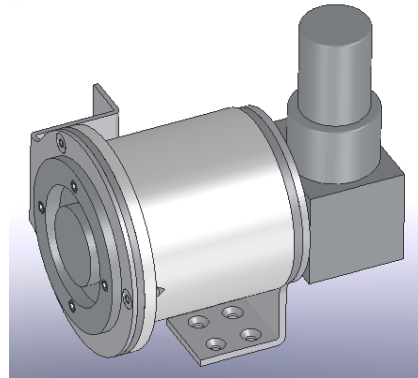
(a)

(b)

Figure 4.29: First Mechanical Brake (a) The CAD model (b) The Manufactured System

The actuation of the motor side conical surface is supplied by using a DC motor as shown in the Figure 4.30. A custom built DC motor is produced which works within 0-24 V range to overcome the torque requirements. Before using the custom built DC motor, when the user applies force to the user side conical surface along the shaft, the braking pads transmit the force directly to the motor side conical surface. For the power screw with four threads is not self locking, the applied force is corresponded by the DC motor. Therefore, a custom made gearbox, using bevel gears which are self locking, is implemented to the DC motor with a ratio of 22:1. A high precision potentiometer is attached to the output shaft of the gearbox which is a product of the Bourns Inc. [89]. The model number of the potentiometer is 6637S-

1-102 with a resistance of 1 kohms. The potentiometer gives an output which varies from 0 to 5 V.

Figure 4.30: The DC Motor of FMB

In order to control the motion of the DC motor, a board including PIC16F877A microchip is used as shown in the Figure 4.31 (a). Another board with L298 speed control chip on it is manufactured and connected to main control board as shown in the Figure 4.31 (b). The signal of the potentiometer is connected to main control board and using a program developed at the PC, they are read successfully.

(a)   (b)
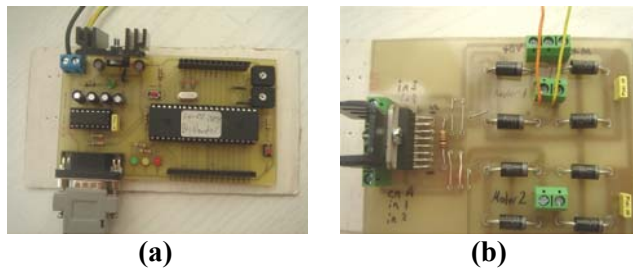
Figure 4.31: (a) Main Control Board with PIC 16F877A (b) Motion Control Card with L298

4.8. THE EXPERIMENTS, THE PROBLEMS, THE SUGGESTIONS AND THE RESULT OF THE FMB

A test setup is constructed to measure the output torque of the FMB as shown in the Figure 4.32 with CAD model. The brake is connected to a torque sensor from the

Sensor Technology [90]. The model of the torque sensor is RWT 310 which measures torques up to ±30 Nm [90]. The output of the torque sensor is analog voltage within ±5 V range. The output voltage of the torque sensor changes linearly based on measured torque.
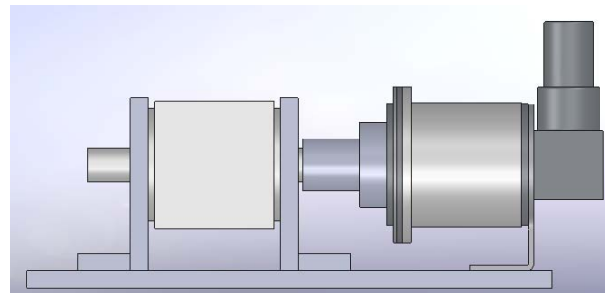
(a)
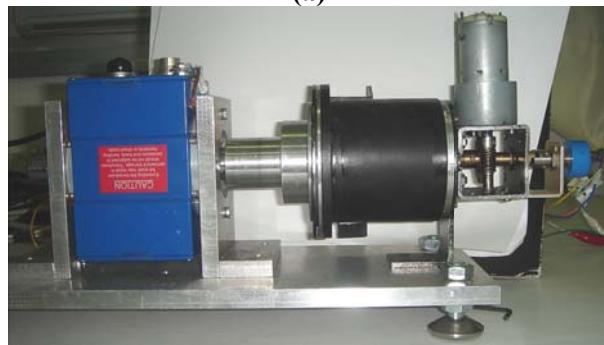
(b)

Figure 4.32: Test Setup (a) The CAD model (b) The Manufactured One

At first, the DC motor is tried to be driven by using the PWM of the PIC16F877A. By regulating the output voltage, speed of the DC motor is tried to be controlled using motion control card including L298 but L298 cannot supply these voltages to the DC motor. Thus, the motion control card is changed with a motor driver which is Faulhaber MCDC-3003/06S [91]. The motor driver has input voltage of 24 V. The motor driver mainly regulates the voltage supplied to the DC motor using the signal given from PIC 16F877A using PWM module. The control system simply works as shown in the Figure 4.33
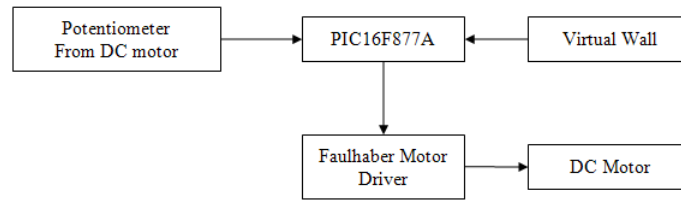
Figure 4.33: Control System of FMB

The working principle of the expected system can be explained starting from the user side. The user starts to freely rotate the arm until it reaches to the virtual wall. Then, the PIC16F877 activates the Faulhaber Motor Driver to drive DC motor. The DC motor drives the power screw and the motor side conical surface to create the initial braking torque. The user continues to apply force to push the conical surface at the user side to increase the braking torque. The user pushes the arm until the system is locked when the user touches virtual wall. Here, the aim is to make the user feel the inclined surface and understand position of the virtual wall, but the FMB is never worked like as expected.

At initial attempts, the system was locked by the DC motor which caused the braking pads to apply the maximum braking torque. Then, it was decided to control the position of the DC motor and thereby the position of the motor side conical surface. At first, it was expected that the DC motor drives the power screw with a turn of 90 degrees. This rotation angle was decreased to move the motor side conical surface less than 8 mm and create a space for the user side conical surface. The aim was to let the set screw at the user side to climb the "V" shape. However, the braking action completely lost and the outer cap started to slip over the braking pad. At the end, half of the outer cap was manufactured and it is understood that the conical surface at the user side is squeezed if the motor side conical surface is driven 8 mm. If it is driven less than 8 mm, the set screw forces the "V" shape to rotate instead of slipping along the shaft. The squeezed position of the user side conical surface is shown below in the Figure 4.34.

95

Figure 4.34: Braking Pads Squeezed the User Side Conical Surface

In case of applying less activation force by the DC motor, the rotation of the "V" shape occurs. In order to overcome this problem, the connection of the user side conical surface to linear sliders, is discussed. The linear sliders, numbered as 4 in the Figure 4.35, are used to move the motor side conical surface, numbered as 6, along the shaft, numbered as 3. There are more than 4 "V"s in the modified "V" shape as shown in the Figure 4.35. In the modified design, instead of rotation of the user side conical surface, it just slides on the linear sliders. When the user rotates the arm, the set screws climb up one side of the "V" shape and then climb down from the side of the adjacent "V" shape. However, the accuracy of "V"s at the virtual wall collision is to be decreased. The set screw can be located between two "V"s, when the one side of the "V" reaches to the virtual wall. In this circumstance, the set screw travels all the surface of "V" instead of climbing one of side the "V". So, the production of this design is discarded because of getting decreased accuracy. It is also noticed that the braking pads, numbered as 1 in the Figure 4.35, moves freely in the outer cap. The motor side conical surface pushes them forward but there is nothing available to pull them back.
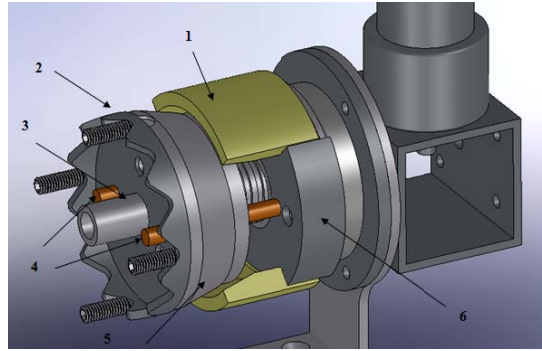
Figure 4.35: Modified "V" Shape

The friction on the "V" shape prevents the FMB to work as expected. It is considered that the angle of the "V" shape may be lowered and some parts, which slip easier than the set screws, may be used to overcome this problem. However, these solutions are not corresponded the expectations from the brake and the design is decided to be modified.

4.9. MODIFIED DESIGN OF THE FMB

The FMB has not worked as expected from the problems of the "V" shape. Nevertheless, during the trials of the FMB, it has been realized that the FMB produces great amount of braking torque. Thus, a part which takes the job of the "V" shape has to be added to the FMB. In the second mechanical brake (SMB), a leaf spring is used to serve like the function of "V" shape. It is more comprehensive to indicate the job of the leaf spring using the Figure 4.37 (a). A leaf spring, numbered as 1 in the Figure 4.36, is fixed to the outer cap. Part 2 is used to transmit the force to the leaf spring. Another job of the part 2 is to change the coefficient of the leaf spring by sliding up and down. The force is applied by the user using the arm attached to part 3. The part 3 is also connected to part 4 which freely rotates on the outer cap. When the brake is at off-state, the conical surfaces are in the home position; the user can freely rotate the arm without encountering any reaction force. While moving the arm, the outer cap and part 4 rotates together with the help of the leaf spring. When the DC motor drives the power screw and activates the brake, the

97

outer cap becomes immobile due to the braking torque but the part 4 continues to rotate because of the force applied by the user. At this time, the leaf spring starts to bend which behaves like the one side of the "V" as shown in the Figure 4.37 (a). Thus, the user can feel the virtual wall. A potentiometer, numbered as 5, is connected to the part 4 using the part 6. The aim of the potentiometer is to measure the position of the user. Therefore, it is possible to find out whether the user approaches to the virtual wall or not. Also, the braking pads are staying coupled with the user side conical surface after the braking for nothing pulls them back. Hence, a hole, which is shown in the Figure 4.37 (b), is drilled to the motor side of the braking pads which pulls the braking pads backward with the help of the DC motor when the brake is deactivated.
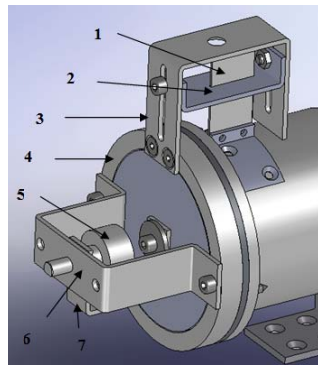
Figure 4.36: New Parts of SMB

| (a) | (b) |

Figure 4.37: (a) The Leaf Spring (b) The Braking Pads

4.10. THE PRODUCTION AND IMPLEMENTATION OF SMB

In the SMB, the part 4 is made of aluminum. The other parts are cut from sheet steel with a thickness of 2 mm using laser cutting and bended using CNC machine. The CAD model and the assembled brake after production are shown in the Figure 4.38. The technical drawings of new parts are given as exploded view in the Appendix D.2. The new parts increase the weight of the brake nearly 200 g.
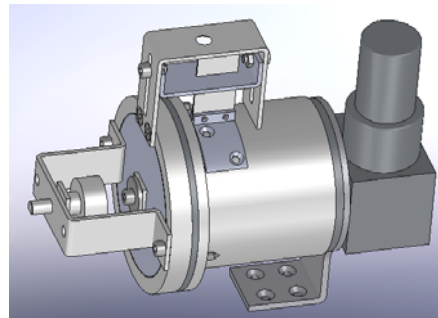
(a)

(b)

Figure 4.38: Second Mechanical Brake (a) The CAD model (b) The Manufactured System

The position of the arm is detected using a high precision potentiometer. The potentiometer is chosen from the products of the Bourns [89]. The model number of the potentiometer is 3590S-2-102 with a resistance of 1 kohms. The potentiometer has 3 legs as shown in the Figure 4.39. One of the legs, numbered as 3, is grounded and 5 V is applied to the leg numbered as 1. The potentiometer gives an output

which varies from 0 to 5 V. The output can be read from the last leg, numbered as 2.

Figure 4.39: High Precision Potentiometer

This time, the SMB is connected to PC using Data Acquisition (DAQ) card instead of using PIC16F877A to control the system. The DAQ used in the system is manufactured by Humusoft MF624 [93]. The same motor of the FMB is driven using Faulhaber MCDC-3003/06S motor driver which regulates the voltage supplied to the DC motor using the signal given from the DAQ card. Using the DAQ, the output of the potentiometers at the user side and the DC motor side are read successfully. The DAQ also produces the output voltage for the motor driver. The maximum output voltage of the DAQ is 10 V which corresponds to maximum 24 V in Faulhaber motor driver. The corresponding voltage at the Faulhaber motor driver changes proportionally due to the output of DAQ.

4.11. THE EXPERIMENTS OF THE SMB

In order to test the braking performance of the SMB a setup is constructed which is similar to the one at the FMB as shown in the Figure 4.40. The SMB, numbered as 7, is connected to torque sensor of Sensor Technology, numbered as 2, using the coupling, numbered as 4. All the parts are mounted on an aluminum table, numbered as 3. The DC motor is numbered as 8. The potentiometers at the user side and at the motor side are numbered as 5 and 9, respectively. The force is applied by the user to measure the braking torque with the help of the lever arm numbered as 1. The leaf spring is denoted with the number 6.
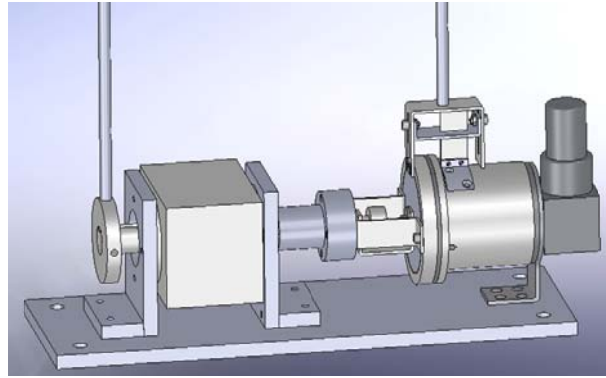
(a)

(b)

Figure 4.40: Test Setup (a) The CAD Model (b) The Manufactured One

The control system is implemented in the Simulink using the Humusoft DAQ. The block diagram of the control system is given in the Figure 4.41. The important parameters of the control system are the reference inputs. The potentiometer gives an output of 0 to 5 V. Thus, the position of the DC motor where the braking action is completed is taken from the potentiometer at the motor side. Also, the initial position of the DC motor is determined from the potentiometer and put into the "reference inputs" box. Moreover, the reference inputs box includes the output voltages for the DAQ to send the Faulhaber motor driver through the main control unit while driving the DC motor forward and backward. The user side position controller box is loaded the position data of the user by the potentiometer at the user side. The position of the virtual wall is given to the user control box as input. The user control box compares it with the position of the user and activates the brake if

the user reaches to the virtual wall. The user side position controller send the activation signal to the main control unit.
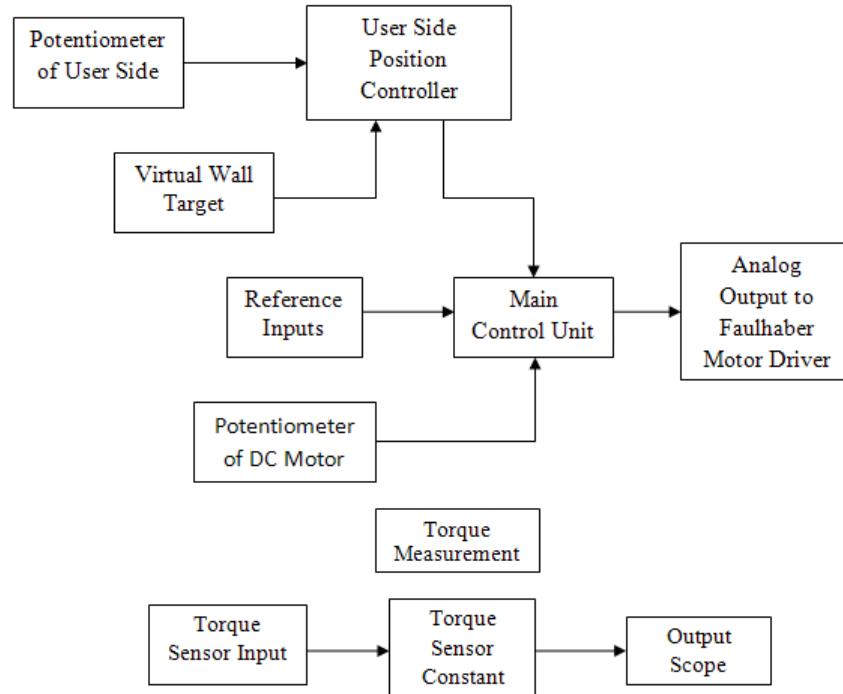
Figure 4.41: Block Diagram of the Control System of SMB

The main control unit principally activates or deactivates the brake due to signal from the user side position controller box. When the user reaches to the wall, the main control unit activates the brake. The DC motor drives the conical surfaces to press the braking pads towards the outer cap until the position of the DC motor from the potentiometer reaches to reference value of the braking position. When the user goes away from the virtual wall, the DC motor, this time, tries to pull the conical surfaces with the braking pads to remove the braking force. All of the analog inputs of the control system are passed through Low-pass filter to suppress the noise of the signal.

In the experiments, it is assumed that a virtual wall exists at the 90 degrees. The user takes the lever arm from the position at 0 degree and moves it until he/she

reaches to the virtual wall. When the user arrives to the virtual wall, the brake is activated to produce braking torque. It is known that the leaf bends no more than 5 degrees; hence the system activates the brake when the user is at 85 degrees. When the brake is activated, the user starts to feel the virtual wall. After that, the user tries to go away from the virtual wall and the DC motor is reversed to remove the braking torque. In the Figure 4.42, the torque values are shown with respect to the position of the user.
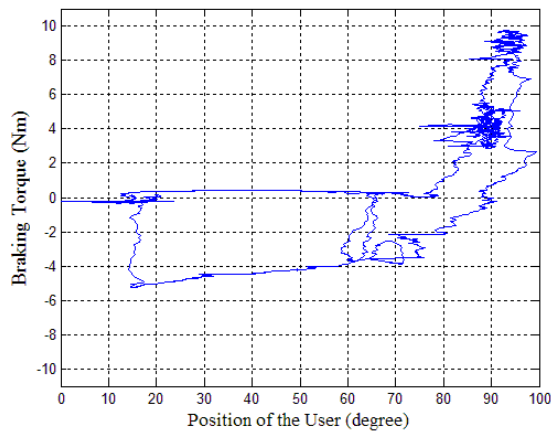
Figure 4.42: Applied Torque Values with respect to the Position of the User

It is obtained from the above figure that the user feels an output torque of up to 10 Nm. Thus, it is noticed that the virtual wall applies a reaction force to the user when the user "pushes" the wall. On the other hand, when the user tries to move away from the virtual, he/she cannot do this action easily. The braking pads stay locked even the DC motor is reversed and tries to pull them back. Thus, the user has to apply force to take the hand away from the virtual wall. The squeeze problem of the braking pads is also seen in the Figure 4.42. The user applies a torque of nearly 5 Nm to go away from the virtual wall. Moreover, it can be indicated that the friction affects the performance of the brake due to a torque about 1 Nm is exerted to the user in the free rotation of the user.
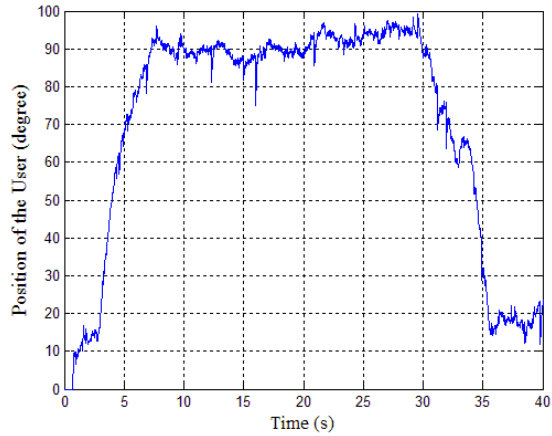
Figure 4.43: Position of the User

When the user reaches to the virtual wall, the braking action is completed. The user pushes towards the virtual wall at 90 degrees as shown in the Figure 4.43. The braking system tries to hold the user at 90 degrees. An increase in the applied force by the user causes a penetration into the wall.

Finally, the position of the DC motor is given in the Figure 4.44 (a). The position of the DC motor is taken from the potentiometer and used as analogue voltage. The activation time of the brake can be determined from the Figure 4.44 (b) as 300 ms.

(a)

(b)
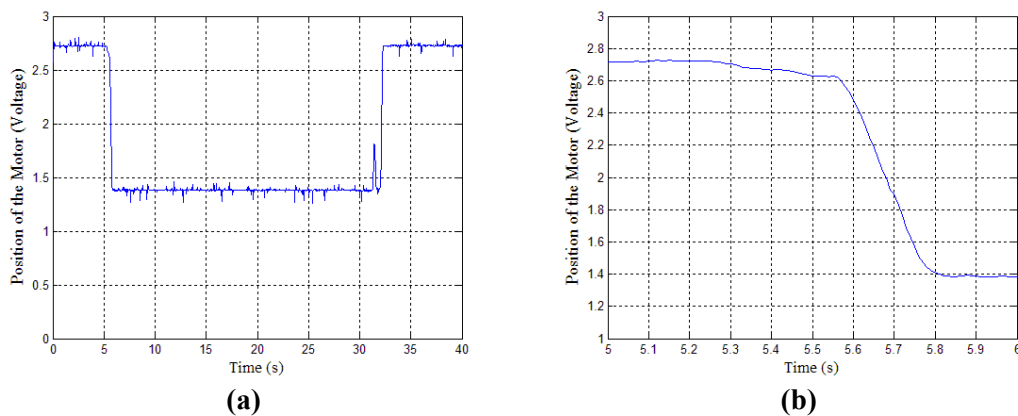
Figure 4.44: (a) Position of the DC Motor (b) Activation of the Brake

104

In conclusion, the SMB produce the feeling of virtual wall and resists against the force applied by the user with high amount of torque. On the other hand, release action from the wall remains a confusing problem. The DC motor tries to pull the braking pads backward but they still stayed stuck until the user supplies a force to release from the wall. The friction is the main design principle of this system but it results to unexpected behavior of the mechanical brake. In this condition, the SMB cannot be used as a passive actuator in a haptic device.

4.12. THE DEVELOPED MECHANICAL BRAKE DESIGN

FMB has not worked as expected, and some improvements have been applied on it which has resulted in SMB. SMB has worked as expected. Here the expectation is accepted as the feeling of the virtual wall, but some problems still exist. Also, the manufactured brakes are bigger and heavier than the expected brake. The modifications implemented on the FMB increase the length of the brake. The results and the manufactured brakes have encouraged making a new brake design.

First, the encountered problems in the FMB and SMB are determined. Then, by using the working principle of the SMB, an improved mechanical design is achieved once more. The problems in manufacturing, assembling and working stages of the previous versions are listed below:

- The main and probably the most compulsive problem has been encountered in the assembling stage. The exploded view of the CAD model of the FMB has been obtained and parts have been designed taking the assembling order into consideration, but it has been very hard to put the system together. In the exploded view, the parts driven by the DC motor have been mounted first together with the user side conical surface and the braking pads. Then the outer cap has been established on these parts; but after production, it has been observed that the flange which was designed to hold the ball bearing at the outer cap has made this part to be mounted before the conical surfaces and the braking pads. The detailed views of the flange from the CAD model and the produced model are shown in the Figure 4.45. Assembling the parts inside the outer cap

has made the mounting process more challenging. Also, the thin sheet metal used in the production of the outer cap has affected the performance of the brake and it is accepted as the one of the reason of the squeeze problem occurred at the braking pads.

(a)   (b)
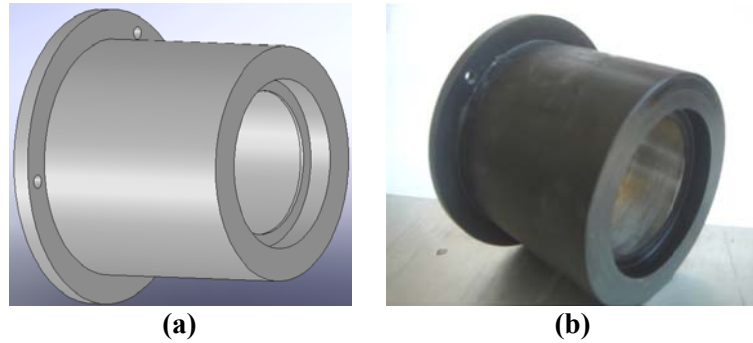
Figure 4.45: Detailed View of the Outer Cap (a) The CAD Model (b) The Produced Part

- In order to acquire the necessary motion from the DC motor, a special power screw has been designed. Production of this part was difficult. Also, the power screw was not self-locking which resulted to the production of a custom gearbox to be used in the DC motor. The alignment of the bevel gears and the output shaft of gears have caused the system to be locked. When the DC motor was intended to move backward to release the braking pads, it stayed still locked because of the problems arising from production of the gearbox.

- Other problem encountered at the DC motor side was that the output shaft of the DC motor was going inside the main shaft and the power screw has been mounted on it. Also, the main shaft was assembled with interference fitted to the ground. This has resulted to the alignment problems and caused a decrease at the power supplied by the DC motor. Moreover, to separate the DC motor from the brake, all the parts have to be removed before the DC motor. In addition, the gap, which lets the DC motor to drive only 90 degrees, causes

difficulties on the control of the motor. The detail of the shaft assembly is shown in the Figure 4.46.

(a)   **(b)**
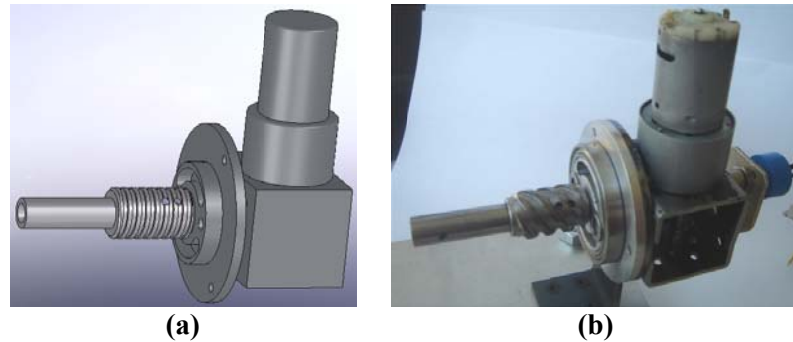
Figure 4.46: Assembly of the Shaft (a) The CAD Model (b) The Manufactured Parts

- The braking pads have caused the system to be locked as mentioned in the problems of the FMB. In the SMB, the braking pads are doing their jobs but when the DC motor is reversed, the system is still stay locked even the braking pads are pulled back via DC motor.

- The size and weight of the brake is over the expectations.

- Moreover, the problems of the "V" shape, which is discussed in detail above, are taken into consideration and removed from the new design.

The problems listed above are kept in mind while designing the enhanced system. The expectations are changed in the new system. It is expected that the new brake produces 1 Nm torque with a minimal design in weight and size relative to the existing designs.

The calculations of new brake are performed using the equations derived at the FMB section. In the developed mechanical brake (DMB), the user does not supply

any force, therefore it is removed from the calculations. First, the activation force is calculated using the equation 4.6. Recall the equation 4.6,

$$F_{act} = 2\pi p_{max}\left(1 + \frac{\mu_{cone}}{\tan\alpha}\right)r_i(r_o - r_i)$$

Just like in the design of the FMB, the angle of the conical surface, "α", the coefficient of the friction, "μ_{cone}", the maximum pressure, "p_{max}" are taken 15 degrees, 0.2, 0.7 MPa, respectively. The radiuses of the outer and the inner cone are chosen 16 mm and 14 mm, respectively to reduce the size of the new brake. Thus, the activation force required for the conical face is computed using the equation 4.6 as,

$$F_{cone} = 215\ N$$

The necessary torque for the DC motor is calculated using equation 4.12. Instead of using a special screw as in the FMB, this time, a standard M6 screw with one thread and a pitch of 1 mm is chosen. The mean diameter is taken as $d_m = 6\ mm$ and the coefficient of friction is chosen as "$\mu_{screw} = 0.08$". Then, using the equation 4.12 the torque supplied by the DC motor is calculated as,

$$T_{screw} = 0.264\ Nm$$

Finally, the torque exerted to the hub is calculated using the equation 4.9 as,

$$T_{BRAKE} = 0.86\ Nm$$

where "$R_{dim} = 18\ mm$" is taken. Thus, the contact length of the braking pad is found as,

$$L_{pad} = 8.5\ mm$$

At the end, sizes of parts are determined successfully. The parts are designed using the results and applied to the CAD model as shown in the Figure 4.47.

The actuation of the DMB provided by a DC motor, numbered as 1, is shown in the Figure 4.47 (b). The DC motor is connected to part 12 using the part 13 to fix it to ground. Instead of fixing the shaft as in the FMB and SMB, the shaft, numbered as 2, is mounted to part 3 using a ball bearing and part 3 is fixed to the ground using the part 12. Also, a coupling, which numbered as 14 and details of which are shown in the Figure 4.48, is designed to align the DC motor and the shaft properly and to prevent the squeeze problem between the DC motor and the shaft. Distinctively from the FMB and SMB, the activation force is provided by the shaft which has screw thread on it. Thus, the DC motor drives the shaft more than 90 degrees. Also, the DC motor can be easily detached from the system without touching other parts.

(a)

(b)
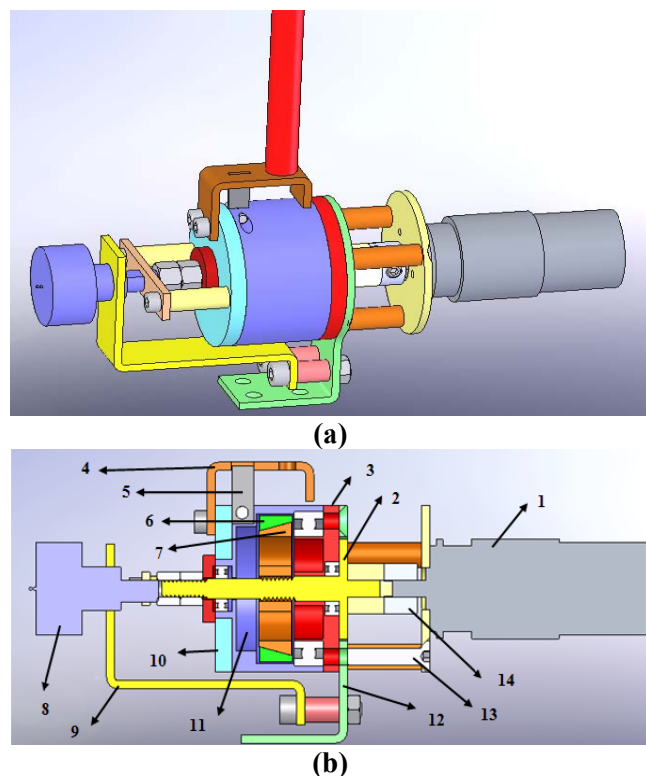
Figure 4.47: (a) The CAD Model of the DMB (b) Section View of the DMB
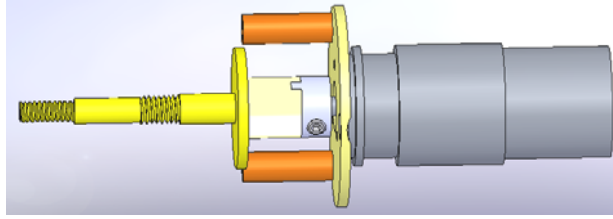
Figure 4.48: The Coupling

The shaft drives the conical surface, numbered as 7, to activate the brake pads which is numbered as 6. The conical surface pushes the brake pads to press to the outer cap, numbered as 11, and to obtain braking torque. Here, the arm, the bar in the Figure 4.47 (a), is connected to the system using the part 4. Part 4 is connected to the outer cap using the leaf spring, numbered as 5, which has the same working principle as of the SMB. Part 4 is also connected to part 10 which freely rotates on the outer cap. The potentiometer, numbered as 8, is connected to the part 10 which is also driven by the user with the help of the leaf spring. The potentiometer is mounted to ground using the part 9.

4.13. THE MANUFACTURING AND IMPLEMENTATION OF THE DMB

The technical drawings of each part are prepared and given to the machine workshop. The technical drawings of the parts are given as an exploded view in the Appendix D.3 as well. The shaft which carries all the parts is made of steel. The braking elements, the conical surface and the braking pads are also produced from steel to acquire the necessary friction. The outer cap is completely made of steel because of the problems encountered from the outer cap of the FMB and SMB. The remaining parts, expect parts 4, 9, and 12, are made of aluminum to decrease the weight of the system. The parts mentioned up to now are manufactured using the lathe and the milling machine. The parts 4, 9 and 12 are cut from sheet steel with a thickness of 2 mm using laser cutting and bended using CNC machine. The leaf spring is prepared by hand. In the Figure 4.49, the CAD model and the assembled

brake after production are shown. The DMB has a weight of 203 g without the DC motor which weighs nearly 150 g.

(a)

(b)
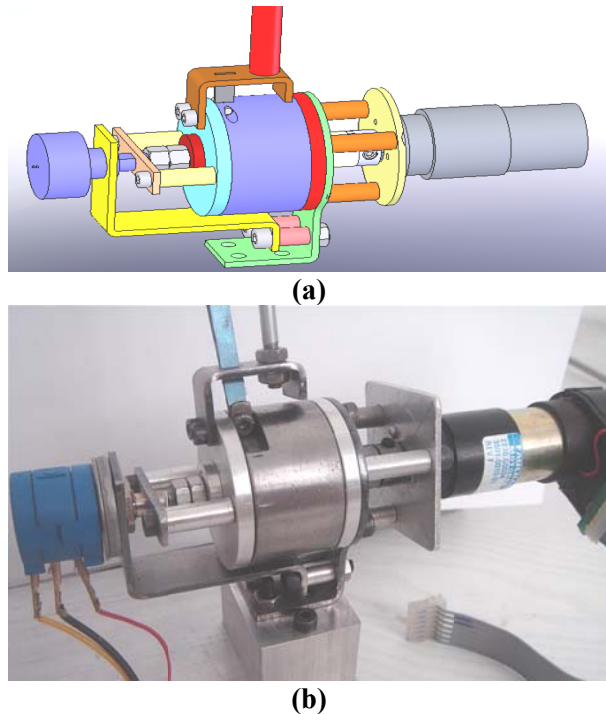
Figure 4.49: Developed Mechanical Brake (a) The CAD model (b) The Produced One

The system is actuated by using a DC motor which is a product of the Faulhaber [91] as shown in the Figure 4.50. The DC motor is working within 0-24 V range. The gearbox implemented to the motor has a ratio of 41:1. The encoder attached to the output of the rotor is the product of the Hewlett Packard which is HP QEDS-5923. It has 512 output pulses per revolution. The encoder has two channel quadrature which has an input voltage of 5 V and gives the output signals at the TTL levels. The motor has no load speed of 219 rpm under the current of 0.05 A. With a load of 0.85 kg, the output speed becomes 90 rpm under the current of 0.65 A [92].

Figure 4.50: DC Motor of DMB

The movement of the arm is sensed using a high precision potentiometer as in the SMB. The potentiometer is chosen from the products of the Bourns again [89]. The model number of the potentiometer is 3590S-2-102 with a resistance of 1 kohms.

The DC motor is driven by Faulhaber MCDC-3003/06S motor driver as in the FMB and SMB. The motor driver mainly regulates the voltage supplied to the DC motor using the signal given from the DAQ card which is Humusoft MF624 again. Using the DAQ, the output of the potentiometer and the encoder of the DC motor are read successfully. The DAQ also produce the appropriate voltage for the motor driver.

Figure 4.51: System Connected to the Boards of DAQ

4.14. THE EXPERIMENTS OF THE DMB

In order to test the performance of the DMB, a setup is constructed. The produced brake is connected to same torque sensor as in FMB and SMB. The brake,

numbered as 2, and the torque sensor, numbered as 5, are established on an aluminum table, numbered as 3, as seen in the Figure 4.52. The DC motor for the activation force is numbered as 1 and the potentiometer to measure the position of the user is numbered as 4. The force is applied by the user with the help of the lever arm which is numbered as 6.

(a)

(b)
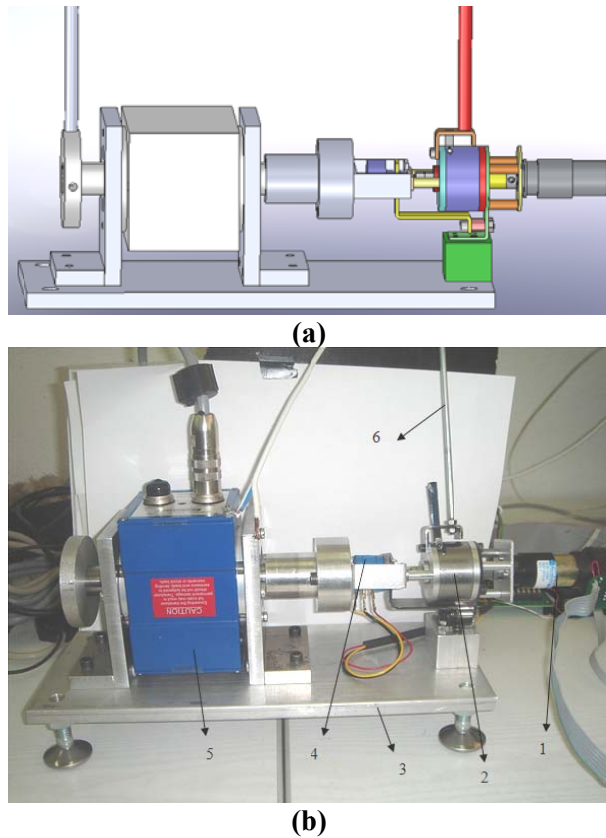
Figure 4.52: Test Setup (a) The CAD Model (b) The Manufactured One

The control system is implemented using the Humusoft DAQ which is connected to the Simulink®.
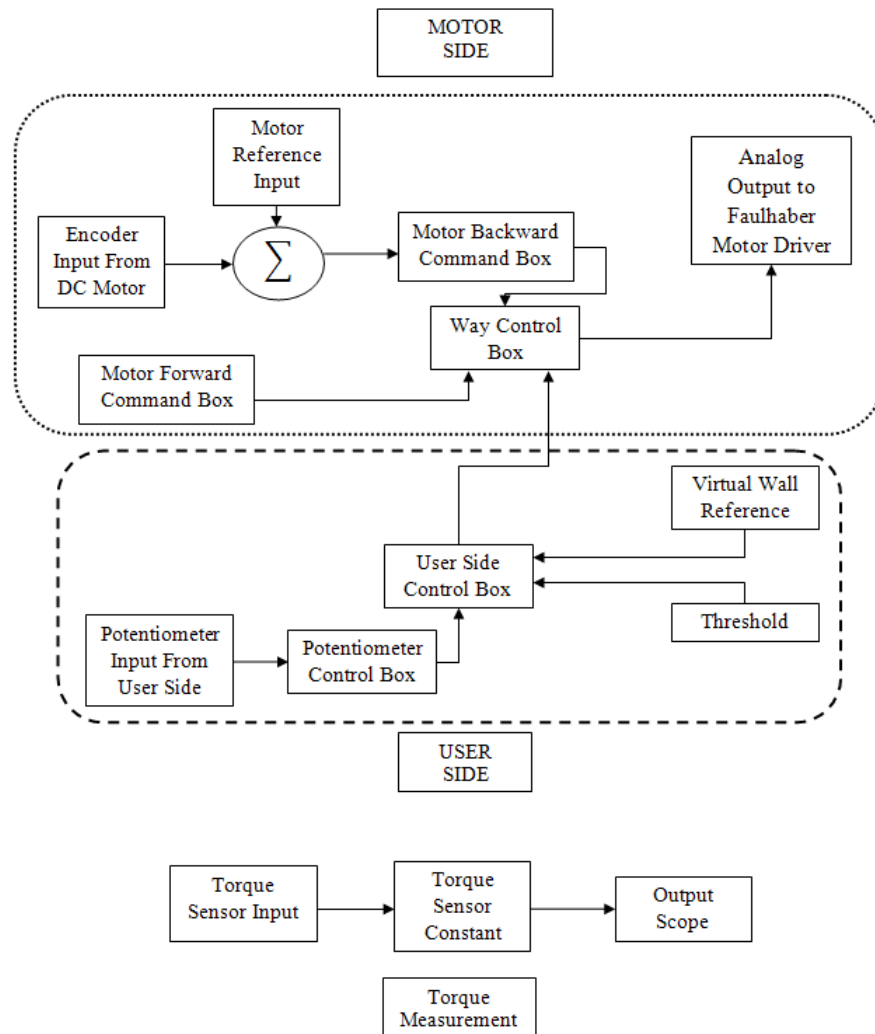
Figure 4.53: Block Diagram of the Control System of DMB

Starting from the user side to introduce the control system, the potentiometer connected to the lever arm supplies the position of the user as an analog voltage. In order to suppress the noise, the potentiometer's signal is passed through the "potentiometer control box" in which Low-Pass Filter is employed. In the test setup the connection between the torque sensor and the DMB only allows 90 degrees of rotation of the lever arm. So, the voltage input is multiplied by a constant to show the potentiometer's signal in 0-90 degrees range. The most important part of the control system is the "user side control box" because this box determines whether

the brake is on or off. It takes three inputs which are the signal of the potentiometer, the position of the virtual wall, and the threshold. The threshold here is the bending angle of the leaf spring which is taken in the experiments as 5 degrees. The position of the virtual wall has to be given to the system taking the threshold value of the leaf spring into consideration. To clarify this part, the values used in the experiments are explained. In the experiments, it is supposed that there is virtual wall at 50 degrees. Thus, the position of the virtual wall is given as 45 degrees taking the 5 degrees threshold into account. The "user control box" checks the position of the user and compares it with the virtual wall's position and decides whether the DC motor is activated or not. If the position of the user enters the threshold range, then the "user control box" sends the activation signal of the DC motor to the "way control box". The "way control box" mainly controls the way of the DC motor and passes the voltage constants provided by motor command boxes to the Faulhaber motor driver to produce analog voltage to drive the DC motor. When the "user control box" sends the activation signal, the "way control box" activates the "motor forward command box". The "motor forward command box" drives the DC motor until the necessary braking torque is produced. When the braking is achieved, the "motor forward command box" stops sending driving voltage constant of the DC motor to the "way control box". After the user starts to move away from the virtual wall, the "user control box" warns the "way control box" to release the brakes. The "way control box" activates the "motor backward command box" which drives the DC motor in the reverse direction using a PID controller which takes the home position of the DC motor as "motor reference input". The aim of the usage of the PID controller is to prevent the squeeze occurring at the shaft. After implementing the control system using the blocks in Simulink, the results are obtained.
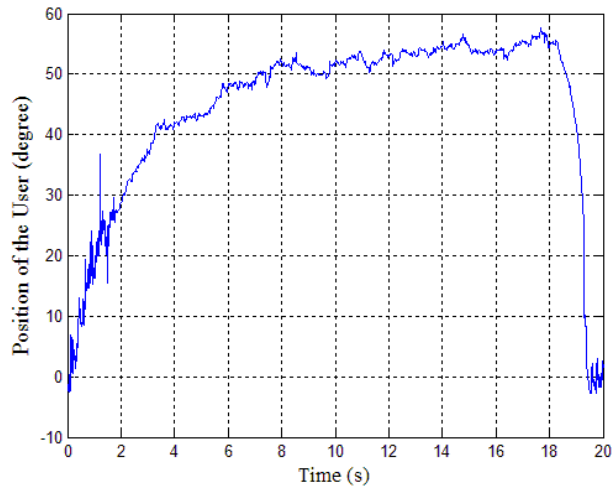
Figure 4.54: Position of the User

In the Figure 4.54, the user approaches to a virtual wall at 50 degrees. After the 6 seconds, the user starts to feel the virtual wall. It seems like a penetration occurring at the virtual wall but in spite of using Low-pass filter to reduce the noise of the signal of the potentiometer, the noise still exists and affects the results. The penetration, in fact, starts after the 12th second, where the user pushes harder.
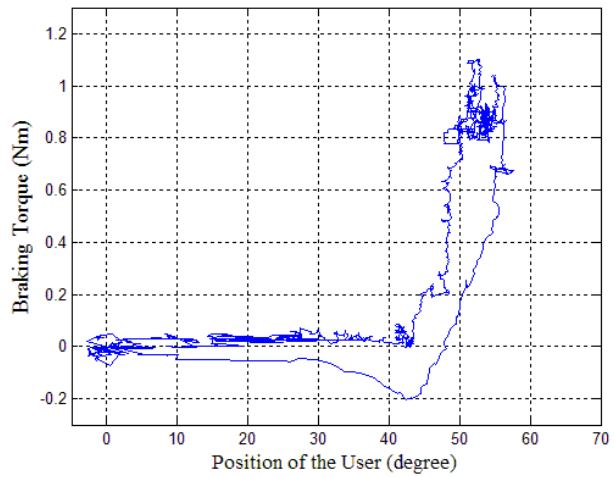
Figure 4.55: Braking Torque vs. the Position of the User

116

In the calculations the braking capacity is calculated as 0.86 Nm but the results of the experiment showed that the DMB can resist a torque of nearly 1.2 Nm as shown in the Figure 4.55. Actually, the braking torque is higher than 1.2 Nm but the leaf spring on the system is chosen with low stiffness. Thus, the penetration increases when the user applies higher forces. On the other hand, from the Figure 4.55, it can be obtained that the squeeze problem of the braking pads is solved. The user can freely move away from the virtual wall without applying a releasing force. This free release is obtained with a change in control system. After many experiments, it is recognized that the user exerts a higher torque than the one in the Figure 4.55 to move away from the virtual wall because the system only checks the position of the user to remove the braking torque. Thus, as stated in the [73], the output of the torque sensor is given to the control system to estimate the way of the user for removing the braking torque.

The output of the encoder of the DC motor is given in the Figure 4.56(a). The activation time of the brake can be determined from the Figure 4.56 (b) as 550 ms.
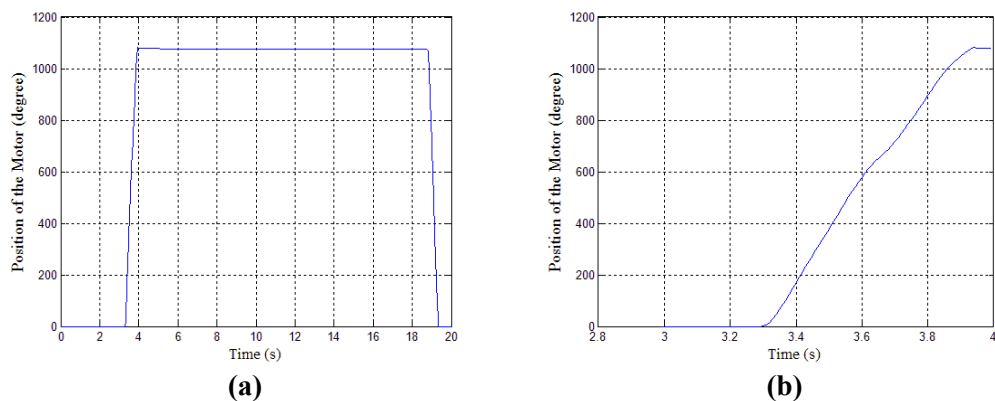
Figure 4.56: (a) Position of the DC Motor (b) Activation of the Brake

The only disadvantage of the DMB is that the response of the braking action is sensitive to the speed of the user. In the Figure 4.57, the user is rotating the arm and reaches to virtual wall at 26.5 seconds starting from 24 seconds. The slope of this

figure, which is 24 deg/s, gives us the speed of the potentiometer attached to the user side. To find the speed of the user, it is multiplied by the length of the lever arm. So, the speed of the user is calculated as 64mm/s. Up to a speed of 70 mm/s, the DMB can activate the brake before the user penetrates into the wall, but for the higher speeds, it is hard to stop the user before penetrating into the wall.
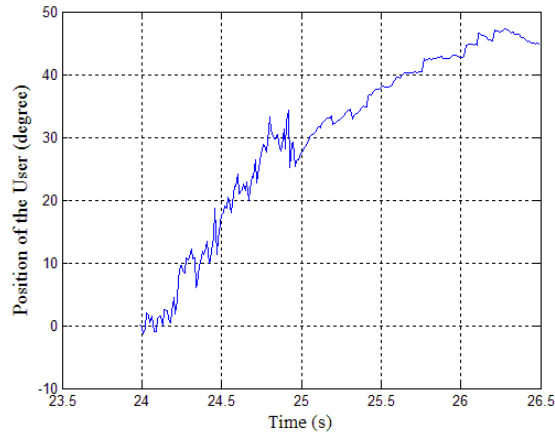
Figure 4.57: Position of the User

4.15. DISCUSSION AND COMMENTS

In this chapter, the design of a mechanical brake, which is used as a passive actuator, is discussed. The chapter starts with the introduction of the actuation systems and then states the actuation types. Examples of the passive actuators are introduced. The types of the mechanical brakes have been compared and the cone type has been decided to be used for transferring high torque values with a small activation force. The working principle of the cone brake is given in detail and the design process starts with the FMB which is adapted from coaster brake. The user has been tried to be used as a force supplier in the FMB, but the design approach for the transferring the user force to the braking action has not been worked as expected.

The solutions are discussed and then it is decided to improve the system by adding new parts. This has resulted to the design of the SMB. The SMB works simpler than the FMB. The experiments conducted by using the SMB show that the SMB applies a reaction force to the user to make him/her feel the virtual wall. In contrast, the problems of FMB are confronted at the SMB again. The braking pads has been stuck resulting to problems same in the deactivation of the brake. The problems of FMB and SMB are listed to overcome in a new design. The new design, DMB, meets the requirements of the mechanical brake. It is noticed that no more stacking problem exists. With the small size and less weight, the DMB can be used in the design of the haptic devices. The results of the experiments show that the user is encountered with enough amount of reaction force while pushing towards the wall. The response time of the DMB is a slightly high. Also, the sensitivity to the speed of the user is critical. The higher speeds of the user cause the user get inside the virtual wall. Both the high response time and the sensitivity to speed of the user are encountered from the DC motor. To supply the necessary activation force for the conical surfaces, the DC motor has to reach high speeds and this is time consuming. As a future work, instead of the DC motor used in the system, a new motor can be used which supplies nearly 1 Nm at higher speeds than the existing one. Thus, the braking torque capacity can be increased to higher values. To detect the position of the user accurately, an encoder with a high pulse per revolution ratio can be implemented to the lever arm instead of the high precision potentiometer. Thus, the penetration and the movements of the user can be noticed more accurately. In order to obtain the direction of the user, the output of the torque sensor is given to the control system. In real applications, a strain gage, instead of big torque sensor, can be attached to the leaf spring to measure the torque exerted by user and the "sticking" problems at the virtual wall can be eliminated.

In conclusion, a mechanical brake is designed to be used as a passive actuator. The brake can be used in the haptic devices in this condition. Further developments should result to a more effective brake. In this case, the DMB can be an alternative

of MR Brakes. A comparison table is given below for mechanical brake, MR Brakes, ER Brake and DC Motor.

Table 4.1: Comparison of the Passive Actuators

	MR Brake [73]	SMB	ER Brake [75]	MR Brake [71]	DMB	Maxon DC Motor [94]
Diameter (mm)	63	90	156	25	40	30
Length (mm)	89.7	120	135	26.5	32	108.7
Weight (g)	-	1200	2600	84	203	390
Max, Torque (Nm)	10.9	10.0	1.3	0.899	1.5	1.0

The output torque can vary from few Newton meters to higher amounts of torques due to requirements by changing the size of the brake in the new designs. Thus, the expectation for the actuators in variable sizes for the joint torques of the manipulator can be provided.

CHAPTER5

DISCUSSION AND CONCLUSION

The aim of this study was to design of the passive haptic robotic arm to be used in the dental implant surgery.

The dental implants mainly meet the aesthetic requirements of the patients, who have lost their teeth, as well as being a dental health care solution. The replaced tooth mostly duplicates the look and function of the lost tooth. However, despite the fact that the dental implants have already appeared to take the place of the conventional denture; the problems of the implant operations, especially in the positioning, still exist. Being a complex procedure with a sensitive operation, the implant operations still have to be applied under the supervision of an experienced dentist. Roughly, a hole needs to be drilled to the jaw of the patient and the implant screw is placed into it. After that, a crown is placed to take the place of the missing tooth. Consequently, the position of the implant hole is very important. Improper placement of the implant hole causes undesirable aesthetic problems and longer recuperation periods. While drilling of the implant hole, IAN can be damaged which leads to unexpected results such as paresthesia of the gum, lip and chin. Thus, the implant hole has to be located accurately.

In this study, the passive haptic robotic arm has been designed to guide the dentist during the dental implant surgery. In order to design the robotic arm properly, an optimization procedure has been followed. The methodology used in the optimization procedure has been aimed to maximize the transparency of the spatial 6R haptic robotic arm by eliminating the parasitic torque and force as felt by the

user. An objective function has been derived using the dynamic properties of spatial 6R robotic arm in the Cartesian space. The objective function has been computed over a path that has been generated to demonstrate a sample implant hole drilling operation. The constraints have been derived using the kinematic equations to limit the working space of the robotic arm. The optimization problem has been solved using GA and SQP. Link lengths and other parameters associated with link lengths including mass and inertia elements together with the position of the operation path with respect to the base position have been optimized. The optimization results have shown that the parasitic torques of the robotic arm has been minimized dramatically and thus, the maximization of the transparency of the robotic arm has been achieved. Also, the robotic arm has been stayed away from the singularities due to the results of the optimization. The results from both GA and SQP optimization techniques have led to very close solutions and thus it has been concluded that a global optimum solution has been found in the constrained search space.

After the optimization process, a mechanical brake has been introduced. The brake is proposed as an actuator for the passive haptic robotic arm to supply necessary braking torques to the joints. The design process has started with the determination of the type of the mechanical brake. It has been intended to design a mechanical brake inspired from the coaster brake. Then the calculations of braking torque and parts of the initial prototype have been explained. In the FMB, it has been expected that the force of the user could be used at the activation force of the conical surface and help the system to be locked. Unfortunately, the design did not yield the expected behavior. Thus, the brake was improved to the new SMB design.

In the experiments, the SMB has produced great amounts of torque with respect to the user against the virtual wall but the stacking problems have occurred when the user demanded to go further away from the virtual wall. The problems encountered at the design of the FMB and SMB have led us to a final mechanical design that works efficiently. The DMB has met all the requirements of the mechanical brake. The user could feel the virtual wall with enough amount of braking torque. Finally,

it has been concluded that the DMB can be used as passive actuators in the design of haptic devices. In this case, the DMB is taken as an alternative to the MR Brakes.

As a future study, further developments will probably result to a more effective brake. The braking torque is also expected to increase by using a new DC motor with high amount of torque at high speeds letting the user feel the virtual wall more rigidly. Positioning accuracy of the brake at the virtual wall will also be increased by using an encoder instead of a high precision potentiometer. Moreover, the brake can be manufactured in different sizes, producing different amounts of torque, to be placed to the joints of a passive haptic robotic arm.

REFERENCES

[1]   W. Korb, R. Marmulla, J. Raczkowsky, J. Muhling, and S. Hassfeld, "Robots in the operating theatre - chances and challenges", International Journal of Oral and Maxillofacial Surgery, Vol. 33, pp. 721–732, 2004.

[2]   D. B. Camarillo, T. M. Krummel, and J. K. Salisbury, Jr., "Robotic technology in surgery: past, present, and future", The American Journal of Surgery Vol. 188, pp.2–15, 2004.

[3]   R. D. Howe and Y. Matsuoka, "Robotics for Surgery", Annual Review of Biomedical Engineering, Vol. 01, pp. 211–240, 1999.

[4]   Intiutive Surgical, Available: [Online] http://www.intuitivesurgical.com Accessed: 23 August 2010.

[5]   Duren Family Dental, Available: [Online] http://www.durenfamilydental.com/ Accessed: 23 August 2010.

[6]   Dental Health Directory, Available: [Online] http://www.dental--health.com/basic_implant_procedure.html Accessed: 23 August 2010.

[7]   T. Fortin, M. Isidori, E. Blanchet, M. Perriat, H. Bouchet and J.L. Coudert., "An Image-Guided System-Drilled Surgical Template and Trephine Guide Pin to Make Treatment of Completely Edentulous Patients Easier: A Clinical Report on Immediate Loading", Clinical Implant Dentistry and Related Research, Vol. 6, No: 2, pp. 111-119.

[8]   R. Bartling, K. Freeman, and R. A. Kraut, "The incidence of altered sensation of the mental nerve after mandibular implant placement", Journal of Oral and Maxillofacial Surgery, Vol. 57, pp. 1408-1410, 1999.

[9]   L.G. Ellies and P.B. Hawker, "The prevalence of altered sensation associated with implant surgery", International Journal of Oral and Maxillofacial Surgery, Vol.9, No:2, 1994

[10]   C.B. Serhal, D. van Steenberghe, M. Quirynen and R. Jacobs, "Localization of the mandibular canal using conventional spiral tomography: a human cadaver study", Clinical Oral Implants Research, Vol. 12, No: 3, pp.230-236, 2001

[11]   O. Basa and Ozkan C. Dilek, "Assessment of the risk of perforation of the mandibular canal by implant drill using density and thickness parameters", Gerodontology, 2010

[12]   D. Buser, W. Martin, U.C. Besler, "Optimizing Esthetics for Implant Restorations in the Anterior Maxilla: Anatomic and Surgical Considerations", International Journal of Oral and Maxillofacial Implants, Vol. 19, No. 7, pp.43-61, 2004.

[13]   B. Leblebicioglu, S. Rawal, A. Mariotti, "A review of the functional and esthetic requirements for dental implants", Journal of American Dental Association, Vol. 138, No. 3, pp.321-329, 2007.

[14]   K. Lal, G. S. White, D. N. Moreand, R. F. Wright, "Use of Stereolithographic Templates for Surgical and Prostodontic Implant Planning and Placement, Part 1, The Concept" Journal of Prosthodontics, Vol. 15, No:1, pp. 51-58, 2006.

[15]   SurgiGuide, Materialize Medical, Available: [Online]
 http://www.materialize.com Accessed: 23 August 2010.

[16]   M. Klein and M. Abrams, "Computer Guided Surgery Utilizing a Computer-Milled Surgical Template", Practical Procedures and Aesthetic Dentistry, Vol. 13, No:2, pp. 165-169, 2001.

[17]   S. Hassfeld, J. Muhling, "Computer assisted oral and maxillofacial surgery – a review and an assessment of technology." International Journal of Oral and Maxillofacial Surgery, Vol. 30, pp. 2–13, 2001.

[18]   A. Wexler, S. Tzadok, N. Casap, "Computerized navigation surgery for the safe placement of palatal implants", American Journal of Orthodontics and Dentofacial Orthopedics Vol. 131, No: 4, Supplement 1, 100-105

[19]   N. Casap, A. Wexler, J. Lustmann, "Image-Guided Navigation System for Placing Dental Implants", Technology in Practice Vol.25 No. 10, 783-788, October 2004.

[20]   A.D. Nijmeh, N.M. Goodger, D. Hawkes, P.J. Edwards, M. McGurk, "Image-guided navigation in oral and maxillofacial surgery", British Journal of Oral and Maxillofacial Surgery, Vol. 43, pp. 294-302, 2005.

[21]   L. Shapira, ""Image Guided Implantology" – Real-Time Guidance of Dental Implant Surgery in the Operative Field using CT-scan image", DenX Support.

[22]   R. Ewers, M. Truppe, A. Reichwein, A. Wagner, "Computer-aided navigation in dental implantology: 7 years of clinical experience", Journal of Oral and Maxillofacial Surgery, Vol. 62, No: 3, pp.329-334

[23]   J. Brief, D. Edinger, S. Hassfeld, G. Eggers, "Accuracy of image-guided implantology", Clinical Oral Implantology, Vol. 16, 495–501, 2005.

[24]   T.C. Lueth,; A. Hein, J. Albrecht, M. Demirtas, S. Zachow, E. Heissler, M. Klein, H. Menneking, G. Hommel, J. Bier, "A surgical robot system for maxillofacial surgery," Industrial Electronics Society, 1998. IECON '98. Proceedings of the 24th Annual Conference of the IEEE, vol.4, pp.2470-2475, 1998.

[25]   Sensible Technologies, Inc. Available: [Online] http://www.sensable.com Accessed: 23 August 2010.

[26]   N. Kusumoto, T. Sohmura, S. Yamada , K. Wakabayashi, T. Nakamura, H. Yatani, "Application of virtual reality force feedback haptic device for oral implant surgery" , Clinical Oral Implantology, Vol. 17, pp.708–713, 2006.

[27]   S. Yilmaz, E. I. Konukseven, H. Gurocak, "Optimum Design of 6R Passive Haptic Robotic Arm for Implant Surgery", Lecture Notes in Computer Science, Haptics: Generating and Perceiving Tangible Sensations, Vol 6191, pp. 105-110, 2010.

[28]   K.   Vlachos   and   E.   Papadopoulos,   "Transparency   Maximization Methodology for Haptic Devices", IEEE/ASME Transactions on Mechatronics, Vol. 11, No. 3, pp. 249-255, June 2006.

[29]   R. Vijaykumar, M. J. Tsai, and K. J. Waldron, "Geometric optimization of serial chain manipulator structures for working volume and dexterity", The International. Journal of Robotics Research, Vol. 5, No. 2, pp. 91–103.

[30]   B. Paden and S. Sastry, "Optimal Kinematic Design of 6R Manipulators", The International Journal of Robotics Research, Vol. 7, No: 2, pp. 43-61, 1988

[31]   P.R. Bergamaschi, A.C. Nogueira, S.F.P. Saramago, "An Optimal Design of 3R Manipulators Taking into Account Regular Workspace Boundary", Proceedings of 18th International Congress of Mechanical Engineering, ABCM, São Paulo, Brasil, 2003.

[32]   P. R. Bergamaschi, S. F. P. Saramago, L. S. Coelho, "Comparative study of SQP and metaheuristics for robotic manipulator design", Applied Numerical Mathematics, Vol. 58, No. 9, pp. 1396-1412, 2008.

[33]   M. Ceccarelli and C. Lanni, "A Multi-Objective Optimum Design of General 3R Manipulators for Prescribed Workspace Limits", Mechanism and Machine Theory, Vol. 39, pp. 119–132, 2004.

[34]   G. Carbone, E. Ottaviano, and M. Ceccarelli, "An Optimum Design Procedure for Both Serial and Parallel Manipulators", Proceedings of the Institution of Mechanical Engineers, Part C: Journal of Mechanical Engineering Science, Vol. 221, pp. 829-843.

[35]   S. Mitsi, K.-D. Bouzakis, D. Sagris, G. Mansour, "Determination of Optimum Robot Base Location Considering Discrete End-effector positions by means of Hybrid Genetic Algorithm", Robotics and Computer-Integrated Manufacturing, Vol. 24, No. 1, pp. 50-59, 2008.

[36]   S. Kucuk and Z. Bingul, "Link Mass Optimization of Serial Robot Manipulators using Genetic Algorithms", Lecture Notes in Computer Science, Knowledge-Based Intelligent Information and Engineering Systems, Vol. 4251, pp. 138-144, 2006

[37]   P. Millman and E. Colgate, "Design of a Four Degree-of-Freedom Force Reflecting Manipulandum with a Specified Force/torque Workspace," in Proc. IEEE ICRA, Vol. 2, pp. 1488–1493, 1991.

[38]   O. Khatib and A. Bowling, "Optimization of the Inertial and Acceleration Characteristics of Manipulators", in Proc. IEEE ICRA, Vol. 4, pp. 2883–2889, 1996.

[39]   K. D. Papakostas, S.G. Mouroutsos and B. Porter,"Genetic Design of Dynamically Optimal Robotic Manipulators", Proc. Instn. Mech. Engrs. Vol. 212 Part I, pp. 423-436.

[40]   E. Papadopoulos, K. Vlachos, and D. Mitropoulos, "On the Design of a Low-force 5-dof Force - Feedback Haptic Mechanism", Proc. ASME 27th Biennial Mechanisms and Robotics Conference - 3rd Symposium on Medical Devices and Systems, 2002.

[41]   E. Papadopoulos, K. Vlachos, and D. Mitropoulos, "Design of a 5-dof Haptic Simulator for Urological Operations," Proc. IEEE International Conference on Robotics and Automation (ICRA' 02), 2002.

[42]   K. Vlachos, E. Papadopoulos, and D. Mitropoulos, "Design and Implementation of a Haptic Device for Urological Operations", IEEE Transactions on Robotics and Automation, Vol. 19, No. 5, pp. 801-809, 2003.

[43]   K. Vlachos, E. Papadopoulos, and D.N. Mitropoulos, "Mass/inertia and joint friction minimization for a low-force five-dof haptic device", Robotics and Automation, 2004. Proceedings. ICRA '04. 2004 IEEE International Conference, Vol.1, pp. 286- 291, 2004.

[44]   K. Vlachos and E. Papadopoulos, "Endpoint-Side Optimization of a Five Degree-of-Freedom Haptic Mechanism", Proc.13th IEEE Mediterranean Conference on Control and Automation, Cyprus, 2005.

[45] L. Sciavicco and B. Siciliano, Modelling and Control of Robot Manipulators, Advanced Textbooks in Control and Signal Processing, Springer, 2005

[46] J. Craig, Introduction to Robotics, Mechanics and Control, Third Edition, Printice Hall, 2005.

[47] J. Denavit and R.S. Hartenberg, "A Kinematic Notation for Lower-Pair Mechanisms Based on Matrices", Journal of Applied Mechanics, pp. 215-221, 1955.

[48] M.K. Özgören, "Application of Exponential Rotation Matrices to the Kinematic Analysis of Manipulators." in: Proceedings, Seventh World Congress on the Theory of Machines and Mechanisms, Seville, Spain, 1987.

[49] M.K. Özgören, "Topological analysis of 6-joint serial manipulators and their inverse kinematics solutions." Mechanism and Machine Theory 37, 511-547, 2002.

[50] M.K. Özgören, "Position and Velocity Related Singularity Analysis of Manipulators." in Proceedings, Nineth World Congress on the Theory of Machines and Mechanisms, Milan, Italy, 1995.

[51] A. Ellery, An Introduction to Space Robotics, Springer-Verlag Berlin, 2000.

[52] M. W. Spong, S. Hutchinson, M. Vidyasagar, Robot Modelling and Control, John Wiley and Sons, 2006.

[53] S. T. McJunkin. Transparency Improvement for Haptic Interfaces. PhD. Thesis, May 2007.

[54] R. P. Paul, Robot Manipulators: Mathematics, Programming, and Control, MIT Press, Cambridge Mass., 1981.

[55] J. Y. S. Luh, M. W. Walker, & R. P. C. Paul, "On-Line Computational Scheme for Mechanical Manipulators", Trans. ASME, J. Dynamic Systems, Measurement and Control, vol. 102, no. 2, pp. 69-76, 1980.

[56]   Optimization Toolbox™ User's Guide, The MathWorks Inc., 2008.

[57]   Genetic Algorithm and Direct Search Toolbox™ User's Guide, The MathWorks Inc., 2008.

[58]   O. Yeniay, "A Comparative Study on Optimization Methods for the Constrained Nonlinear Programming Problems", Vol. 2005, No: 2, pp.165-173, 2005.

[59]   P. T. Boggs and Jon W. Tolle (1995). Sequential Quadratic Programming. Acta Numerica, Vol. 4 , pp 1-51

[60]   D. Whitley, A Genetic Algorithm Tutorial, Colorado State Univ., pp. 1993.

[61]   G. Mastinu, M. Gobbi, C. Miano, Optimal design of complex mechanical systems : with applications to vehicle engineering, Springer, 2006.

[62]   R. Parekh, "Microchip AN887 AC Induction Motor Fundamentals", Microchip Technology. Inc., 2003.

[63]   Maxon Motor Inc., Available: [Online] http://www.maxonmotor.com/ Accessed: 17 August 2010.

[64]   Shubh Instruments Available: [Online] http://www.shubhinstruments.net/pneumatic-hydraulic-cylinders.html Accessed: August 2010.

[65]   F. Conti and O. Khatib, "A New Actuation Approach for Haptic Interface Design", The International Journal of Robotics Research, Vol.28, No. 6, pp. 834-848, June 2009.

[66]   H. Davis and W. Book, "Torque Control of a Redundantly Actuated Passive Manipulator", American Control Conference, 1997. Proceedings of the 1997, Vol.2, pp.959-963, Jun 1997

[67]   D. Carlson, D. M. Catanzarite, and K. A. St. Clair, "Commercial magnetorheological fluid devices", Int. J. Mod. Phys. B, Vol. 10, pp. 2857–2865, 1996.

[68]   Magnetorheological Fluid, Available [Online]: http://en.wikipedia.org/wiki/Magnetorheological_fluid Accessed: 17 August 2010

[69]   C. Mavroidis, et. al., "Controlled Compliance Haptic Interface Using Electro-rheological Fluids", Proceedings of the 2000 SPIE Conference on Electro-Active Polymer Actuators and Devices, Vol. 3987, p.300-310, 2000.

[70]   M.R. Jolly, J.W. Bender, and J. D. Carlson, "Properties and Applications of Commercial Magnetorheological Fluids", SPIE 5th Annual Int. Sym. On Smart Structıres and Materials", 1998.

[71]   J. Blake and H. Gurocak, "Magnetorheological Fluid Brake for a Force Feedback Glove for Virtual Environments", ASME Conf. Proc. 2005, pp. 1131-1138, 2005.

[72]   J. Blake and H. Gurocak, "Haptic Glove With MR Brakes for Virtual Reality", IEEE/ASME Transactions on Mechatronics, Vol.14, No.5, pp.606-615, Oct. 2009.

[73]   D. Senkal and H. Gurocak, "Compact MR-brake with Serpentine Flux Path for Haptics Applications", World Haptics 2009 - Third Joint EuroHaptics Conference and Symposium on Haptic Interfaces for Virtual Environment and Teleoperator Systems, pp.91-96, 2009

[74]   D. Senkal and H. Gurocak, "Serpentine Flux Path for High Torque MRF Brakes in Haptics Applications", Mechatronics, Vol. 20, pp. 377-383, February 2010

[75]   M. Sakaguchi, J. Furusho, and N. Takesue, "Passive force Display Using ER brakes and Its Control Experiments", Virtual Reality Proceedings, IEEE, pp.7-12, 17-17 March 2001.

[76]   B. Liu, W. H. Li, P. B. Kosasih and X. Z. Zhang, "Development of an MR-Brake-Based Haptic Device", Smart Materials and Structures, Vol. 15, No. 6, pp.1960-1966, 2006.

[77]   D. Senkal, H. Gurocak, and E. I. Konukseven, "Passive Haptic Interface with MR-Brakes for Dental Implant Surgery", Presence, MIT Press, (in review), 2010.

[78]   W.C. Orthwein, Clutches and Brakes Design and Selection, Second Edition, Marcel Dekker Inc., 2004

[79]   Northern Tool Inc. Available [Online]:
http://www.northerntool.com/shop/tools/product_334786_334786
Accessed: 17 August 2010

[80]   Disc Brake, Available [Online]: http://en.wikipedia.org/wiki/Disc_brake
Accessed: 17 August 2010

[81]   J. E. Shigley and C. R. Mischke, Mechanical Engineering Design, Seventh Edition, McGraw-Hill Inc., 2004.

[82]   Cone Clutch, Available [Online]: http://en.wikipedia.org/wiki/Cone_clutch
Accessed: 17 August 2010

[83]   Bicycle Brake Systems, Available [Online]:
 http://en.wikipedia.org/wiki/Bicycle_brake_systems
Accessed: 17 August 2010

[84]   F. Flemming and J. Shapiro, "Basics of Electromagnetic Clutches and Brakes", Machine Design, pp. 57–58, 2009.

[85]   Shimiano Inc., Available: [Online] http://www.shimano.com Accessed: 17 August 2010.

[86]   US Patent No: 5,027,930, Coaster Brake Assembly.

[87]   C.F. Egelhoff and E.M. Odom, "Machine Design: Where The Action Should Be", Frontiers in Education Conference, 1999. FIE '99. 29th Annual, vol.2, pp.12C5/13-12C5/18, 1999

[88]   R. S. Khurmi and J. K. Gupta, Theory of Machines, 14th Revised Edition, S. Chand & Co Ltd, 2000.

[89]   Bourns Inc., Available [Online]: http://www.bourns.com
Accessed: 17 August 2010.

[90]   ST, Sensor Technology, Available [Online]: http://www.sensors.co.uk
Accessed: 17 August 2010.

[91]   Faulhaber Group, Available [Online]: http://www.faulhaber.de
Accessed: 17 August 2010.

[92]   DC Motor Specifications, Available [Online]:
http://www.candhsurplus.com/2005catalog/2-dc-motors.pdf
Accessed: 17 August 2010.

[93]   Humusoft, Available, [Online]: http://www.humusoft.cz/
Accessed: 17 August 2010.

[94]   Maxon Motor, Available, [Online]: http://www.maxonmotor.com/
Accessed: 30 August 2010.

APPENDIX A

KINEMATICS OF THE PASSIVE HAPTIC ROBOTIC ARM

A.1. FORWARD KINEMATICS OF THE ROBOTIC ARM

The kinematic model of a robotic arm can be described using four quantities for each link with a convention called D-H notation [47]. The D-H parameters for a robotic arm with revolute joints describe the link itself and the link connections to the neighboring link [46]. In order to describe the kinematic configuration of a six-joint robotic arm with revolute joints, six set of three D-H parameters (α_i, a_i, d_i) are needed to be known. Before starting to forward kinematics, reference frames are needed to be attached to the links to determine the joint and link parameters due to the D-H convention [48 - 50].

In order to define the position of the link, a reference frame has to be assigned to each link. The reference frame attached to link *i* is defined as follows,

$$\mathcal{F}_i = \mathcal{F}_i \left\{ O_i;\ \vec{u}_1^{(i)}, \vec{u}_2^{(i)}, \vec{u}_3^{(i)} \right\} \tag{A.1}$$

In the Figure A.1, frames attached to links, unit vectors, joint and links parameters are shown. Here, $\vec{u}_3^{(i)}$ is the unit vector along the axis of joint (i+1) and $\vec{u}_1^{(i)}$ is the unit vector along the common normal drawn from joint (i) to joint (i +1). As a result, $\vec{u}_2^{(i)}$ can be defined as,

$$\vec{u}_2^{(i)} = \vec{u}_3^{(i)} \times \vec{u}_1^{(i)} \tag{A.2}$$

Reference frame, formed using unit vectors, has to be a right-handed reference frame. O_i is the origin of the frame $\mathcal{F}_i$ which is located at the intersection of the axis of joint $(i+1)$ and the common normal between joints (i) and $(i+1)$. A_i is the auxiliary point which is located at the intersection of the axis of joint (i) and the same common normal. The joint and link parameters are defined as:

-    $a_i = A_i O_i$ is the effective link length of the link (i) measured along $\vec{u}_1^{(i)}$.

-    $d_i = O_{i-1} A_i$ is the joint offset of the link (i) with respect to the link $(i-1)$ measured along $\vec{u}_3^{(i-1)}$.

-    α_i is the twist angle of the link (i) measured about $\vec{u}_1^{(i)}$ from $\vec{u}_3^{(i-1)}$ to $\vec{u}_3^{(i)}$.

-    θ_i is the rotation angle of the link (i) with respect to the link $(i-1)$ measured about $\vec{u}_3^{(i-1)}$ from $\vec{u}_1^{(i-1)}$ to $\vec{u}_1^{(i)}$.

The base frame $\mathcal{F}_0$ is fixed to base with an arbitrary orientation where $\vec{u}_3^{(0)}$ is along the axis of joint (1). The hand frame $\mathcal{F}_6$ is assigned to the last link where $A_6 = O_6$.
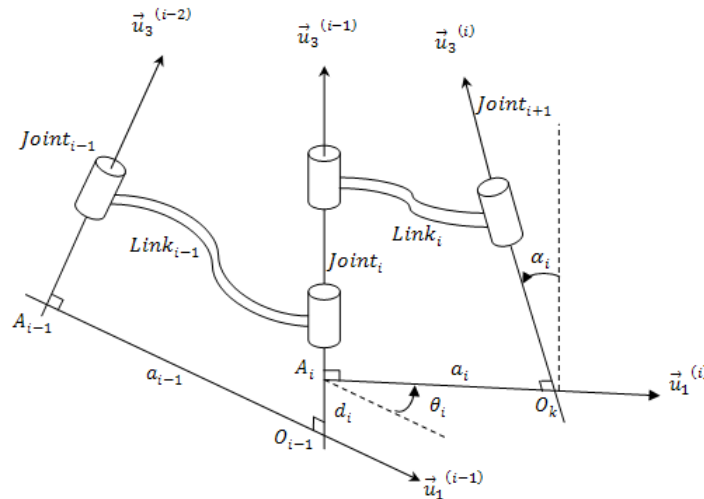
Figure A.1: Illustration of the D-H Convention [49]

135

The exponential rotation matrices are used to express kinematic equations due to their simplicity [48 - 50].The exponential rotation matrices for joint (i) around unit vectors $\vec{u}_1^{(i)}, \vec{u}_2^{(i)}, \vec{u}_3^{(i)}$ are defined as,

$$e^{\tilde{u}_1 \theta_i} = \begin{bmatrix} 1 & 0 & 0 \\ 0 & \cos(\theta_i) & -\sin(\theta_i) \\ 0 & \sin(\theta_i) & \cos(\theta_i) \end{bmatrix}$$

$$e^{\tilde{u}_2 \theta_i} = \begin{bmatrix} \cos(\theta_i) & 0 & \sin(\theta_i) \\ 0 & 1 & 0 \\ -\sin(\theta_i) & 0 & \cos(\theta_i) \end{bmatrix}$$

$$e^{\tilde{u}_3 \theta_i} = \begin{bmatrix} \cos(\theta_i) & -\sin(\theta_i) & 0 \\ \sin(\theta_i) & \cos(\theta_i) & 0 \\ 0 & 0 & 1 \end{bmatrix}$$

where,

$$\bar{u}_1 = \begin{bmatrix} 1 \\ 0 \\ 0 \end{bmatrix}, \bar{u}_2 = \begin{bmatrix} 0 \\ 1 \\ 0 \end{bmatrix}, \bar{u}_3 = \begin{bmatrix} 0 \\ 0 \\ 1 \end{bmatrix}.$$

After attaching the frames to the links and determining the joint and link parameters due to D-H convention, all parameters are listed in the Table 3.1. The kinematic model of the passive haptic robotic arm including the frame attachments with link parameters are given in the Figure 3.2.

Using rotation matrices for six links, the orientation of the tip point with respect to the base frame is given as,

$$\hat{C}^{(0,6)} = e^{\tilde{u}_3 \theta_1} e^{\tilde{u}_2 \theta_{23}} e^{\tilde{u}_3 \theta_4} e^{\tilde{u}_2 \theta_5} e^{\tilde{u}_3 \theta_6} \tag{A.3}$$

Using D-H parameters given in the Table 3.1, exponential matrices between two successive links can be written as,

$$\hat{C}^{(i-1,i)} = e^{\tilde{u}_3\theta_i}e^{\tilde{u}_1\alpha_i} \tag{A.4}$$

Then, rotation matrices for each link can be expressed as,

$$\hat{C}^{(0,1)} = e^{\tilde{u}_3\theta_1}e^{-\tilde{u}_1\pi/2} \tag{A.5a}$$

$$\hat{C}^{(1,2)} = e^{\tilde{u}_3\theta_2} \tag{A.5b}$$

$$\hat{C}^{(2,3)} = e^{\tilde{u}_3\theta_3}e^{\tilde{u}_1\pi/2} \tag{A.5c}$$

$$\hat{C}^{(3,4)} = e^{\tilde{u}_3\theta_4}e^{-\tilde{u}_1\pi/2} \tag{A.5d}$$

$$\hat{C}^{(4,5)} = e^{\tilde{u}_3\theta_5}e^{\tilde{u}_1\pi/2} \tag{A.5e}$$

$$\hat{C}^{(5,6)} = e^{\tilde{u}_3\theta_6} \tag{A.5f}$$

In order to obtain orientation of the end-effector's tip point, rotation matrices for each link are combined as,

$$\hat{C}^{(0,2)} = e^{\tilde{u}_3\theta_1}e^{-\tilde{u}_1\pi/2}e^{\tilde{u}_3\theta_2} \tag{A.6a}$$

$$\hat{C}^{(0,3)} = e^{\tilde{u}_3\theta_1}e^{-\tilde{u}_1\pi/2}e^{\tilde{u}_3\theta_2}e^{\tilde{u}_3\theta_3}e^{\tilde{u}_1\pi/2} = e^{\tilde{u}_3\theta_1}e^{\tilde{u}_2\theta_{23}} \tag{A.6b}$$

$$\hat{C}^{(0,4)} = e^{\tilde{u}_3\theta_1}e^{\tilde{u}_2\theta_{23}}e^{\tilde{u}_3\theta_4}e^{-\tilde{u}_1\pi/2} \tag{A.6c}$$

$$\hat{C}^{(0,5)} = e^{\tilde{u}_3\theta_1}e^{\tilde{u}_2\theta_{23}}e^{\tilde{u}_3\theta_4}e^{-\tilde{u}_1\pi/2}e^{\tilde{u}_3\theta_5}e^{\tilde{u}_1\pi/2} = e^{\tilde{u}_3\theta_1}e^{\tilde{u}_2\theta_{23}}e^{\tilde{u}_3\theta_4}e^{\tilde{u}_2\theta_5} \tag{A.6d}$$

$$\hat{C}^{(0,6)} = e^{\tilde{u}_3\theta_1}e^{\tilde{u}_2\theta_{23}}e^{\tilde{u}_3\theta_4}e^{\tilde{u}_2\theta_5}e^{\tilde{u}_3\theta_6} \tag{A.6e}$$

The position of the end-effector's tip point can be expressed as,

$$\vec{p} = a_2\vec{u}_1^{(2)} + d_4\vec{u}_3^{(3)} + d_6\vec{u}_1^{(6)} \tag{A.7a}$$

The position of the wrist point can be expressed in vector from as,

$$\vec{r} = a_2\vec{u}_1^{(2)} + d_4\vec{u}_3^{(3)} \tag{A.7b}$$

The position of the wrist point can be expressed in the terms of base frame using matrix representation of the unit vectors as,

$$\bar{r} = a_2 \hat{C}^{(0,2)} \bar{u}_1 + d_4 \hat{C}^{(0,3)} \bar{u}_3 \tag{A.8}$$

Taking necessary orientation matrices from the equation A.6 and putting into the equation A.8 gives the position of wrist point in terms of base frame as,

$$\bar{r} = e^{\tilde{u}_3 \theta_1}[(a_2 \cos \theta_2 + d_4 \sin \theta_{23})\bar{u}_1 + d_2 \bar{u}_2 + (-a_2 \sin \theta_2 + d_4 \cos \theta_{23})\bar{u}_3] \tag{A.9}$$

Finally, the position and orientation of the end-effector is obtained in the terms of the joint variables using forward kinematic equations based on D-H convention.

A.2. INVERSE KINEMATICS OF THE ROBOTIC ARM

First step of inverse kinematic solution is to transfer the position matrix from the end-effector's tip point to the wrist by using the orientation matrix defined at equation A.3;

$$\bar{r} = \bar{p} - d_6 \hat{C}^{(0,6)} \bar{u}_3 \tag{A.10}$$

Now, position and orientation of the wrist point is obtained. Recall the equations A.3 and A.9,

$$\bar{r} = e^{\tilde{u}_3 \theta_1}[r_1^* \bar{u}_1 + d_2 \bar{u}_2 + r_3 \bar{u}_3]$$
$$\hat{C}^{(0,6)} = e^{\tilde{u}_3 \theta_1} e^{\tilde{u}_2 \theta_{23}} e^{\tilde{u}_3 \theta_4} e^{\tilde{u}_2 \theta_5} e^{\tilde{u}_3 \theta_6}$$

where

$$r_1^* = a_2 \cos \theta_2 + d_4 \sin \theta_{23} \tag{A.11}$$
$$r_3 = -a_2 \sin \theta_2 + d_4 \cos \theta_{23} \tag{A.12}$$

Rewrite the wrist equation,

$$r_1^* \bar{u}_1 + d_2 \bar{u}_2 + r_3 \bar{u}_3 = e^{-\tilde{u}_3 \theta_1} \bar{r} \tag{A.13}$$

Premultiply equation A.13 by $\bar{u}_1^t$, $\bar{u}_2^t$, $\bar{u}_3^t$ results to,

$$r_1^* = a_2 \cos\theta_2 + d_4 \sin\theta_{23} = r_1 \cos\theta_1 + r_2 \sin\theta_1 \qquad (A.14)$$

$$d_2 = r_2 \cos\theta_1 - r_1 \sin\theta_1 \qquad (A.15)$$

$$r_3 = d_4 \cos\theta_{23} - a_2 \sin\theta_2 \qquad (A.16)$$

In the three equations above, r_1, r_2, r_3 and a_2, d_2, d_4 are known and $\theta_1, \theta_2, \theta_3$ are calculated using these equations. First variable, θ_1 can be computed as,

$$\theta_1 = atan_2(r_2, r_1) - atan_2(d_2, \sigma_1\sqrt{r_2^2 + r_1^2 - d_2^2}) \qquad (A.17)$$

Here σ_1 can be ± 1 which results left and right shouldered configurations. To find third variable, θ_3, squares of equations A.14 and A.16 is summed as,

$$r_1^{*2} + r_3^2 = d_4^2 + a_2^2 + 2d_4 a_2(\sin\theta_{23}\cos\theta_2 - \cos\theta_{23}\sin\theta_2) \qquad (A.18)$$

$$r_1^{*2} + r_3^2 = d_4^2 + a_2^2 + 2d_4 a_2 \sin(\theta_{23} - \theta_2) = d_4^2 + a_2^2 + 2d_4 a_2 \sin(\theta_3) \qquad (A.19)$$

Then, taking $\sin\theta_3$ from equation A.19 results to,

$$\sin\theta_3 = \frac{\left(r_1^{*2} + r_3^2\right) - (d_4^2 + a_2^2)}{2d_4 a_2} = \eta_3 \qquad (A.20)$$

and

$$\cos\theta_3 = \sigma_2\sqrt{1 - \eta_3} \qquad (A.21)$$

The third variable, θ_3 can be calculated as,

$$\theta_3 = atan_2(\eta_3, \sigma_2\sqrt{1 - \eta_3^2}) \qquad (A.22)$$

Here, $\sigma_2 = +1$ yields elbow down configuration and $\sigma_2 = -1$ yields elbow up configuration. The second joint variable θ_2 is needed to be found. Equation A.14 and A.16 can be written in matrix form as,

$$\begin{bmatrix} d_4 \cos \theta_3 & a_2 + d_4 \sin \theta_3 \\ -(a_2 + d_4 \sin \theta_3) & d_4 \cos \theta_3 \end{bmatrix} \begin{bmatrix} \sin \theta_2 \\ \cos \theta_2 \end{bmatrix} = \begin{bmatrix} r_1^* \\ r_3 \end{bmatrix} \tag{A.23}$$

Before putting necessary variables from equation A.14 and A.16 into the equation A.23, the determinant of the first matrix has to be checked for singularity analysis.

$$\det(\hat{A}) = a_2^2 + d_4^2 + 2d_4 a_2 \sin \theta_3 = \Delta_2 \tag{A.24}$$

If $\det(\hat{A}) \neq 0$ then $\hat{X} = \hat{A}^{-1} \hat{B}$,

$$\begin{bmatrix} \sin \theta_2 \\ \cos \theta_2 \end{bmatrix} = \frac{1}{\Delta_2} \begin{bmatrix} d_4 \cos \theta_3 & -(a_2 + d_4 \sin \theta_3) \\ a_2 + d_4 \sin \theta_3 & d_4 \cos \theta_3 \end{bmatrix} \begin{bmatrix} r_1^* \\ r_3 \end{bmatrix} \tag{A.25}$$

$$\sin \theta_2 = \frac{d_4 \cos \theta_3 r_1^* - r_3 (a_2 + d_4 \sin \theta_3)}{\Delta_2} \tag{A.26}$$

$$\cos \theta_2 = \frac{r_1^* (a_2 + d_4 \sin \theta_3) + r_3 d_4 \cos \theta_3}{\Delta_2} \tag{A.27}$$

Then θ_2 can be calculated as,

$$\theta_2 = \text{atan}_2(\sin \theta_2, \cos \theta_2) \tag{A.28}$$

If the determinant of the $\hat{A}$ matrix gives zero, then first singularity occurs. When a_2 and d_4 are same in length and θ_3 is $-\pi\backslash2$, the determinant is zero. When this occurs, θ_2 becomes arbitrary and has no effect on the position of the wrist point which is illustrated in the Figure A.2.

Singularities mainly disable the control of the manipulator. For any given joint variables, the end-effector may not reach to the target position. While moving within the workspace manipulator may need to change the configuration to reach the goal position and this cause very high joint forces and torques. Moreover, singularities have to be determined in the designing stage. The configuration of the robotic arm and the workspace has to be chosen carefully to avoid unexpected results while moving the designed robotic arm [52].
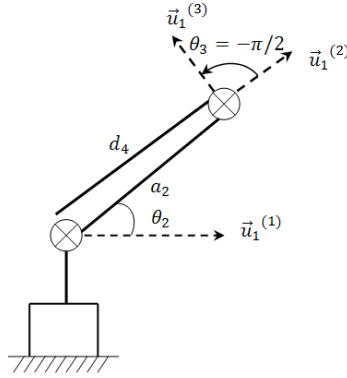
Figure A.2: Illustration of the First Singularity

The positioning stage of the 6R manipulator is found up to now and orientation stage is computed. The composition of spherical wrist is similar to 3-2-3 sequence of Euler. The 3-2-3 sequence of the Euler can be represent as,

$$\hat{C} = e^{\tilde{u}_3 \theta_1} e^{\tilde{u}_2 \theta_2} e^{\tilde{u}_3 \theta_3} = \begin{bmatrix} c_1 c_2 c_3 - s_1 s_3 & -c_1 c_2 s_3 - s_1 c_3 & c_1 s_2 \\ s_1 c_2 c_3 + c_1 s_3 & -s_1 c_2 s_3 + c_1 c_3 & s_1 s_2 \\ -s_2 c_3 & s_2 s_3 & c_2 \end{bmatrix} \qquad (A.29)$$

In this matrix, c_i and s_i represent *cosine* and *sine* of the joint variables and $i = 1,2,3$ represent the joint variables θ_1, θ_2, and θ_3, respectively. To use this matrix in the determination of the joint variables of the spherical wrist, the joint variables θ_1, θ_2, and θ_3 are substituted to θ_4, θ_5, and θ_6, respectively.

Using the orientation matrix at equation A.3 and multiplying both sides with inverse of the first two elements gives as,

$$e^{\tilde{u}_3\theta_4}e^{\tilde{u}_2\theta_5}e^{\tilde{u}_3\theta_6} = e^{-\tilde{u}_2\theta_{23}}e^{-\tilde{u}_3\theta_1}\hat{C}^{(0,6)} \tag{A.30}$$

The right side of the equation A.30 is known. The right side of the equation A.30 can be represented in matrix form as,

$$\hat{C} = e^{-\tilde{u}_2\theta_{23}}e^{-\tilde{u}_3\theta_1}\hat{C}^{(0,6)} = \begin{bmatrix} C_{11}^* & C_{12}^* & C_{13}^* \\ C_{21}^* & C_{22}^* & C_{23}^* \\ C_{31}^* & C_{32}^* & C_{33}^* \end{bmatrix} \tag{A.31}$$

Taking (3,3) element of the matrix results to,

$$C_{33}^* = \cos\theta_5 \tag{A.32}$$

and using the *cosine* of the θ_5, *sine* of the joint variable can be found as,

$$\sin\theta_5 = \sigma_5\sqrt{1 - {C_{33}^*}^2} \tag{A.33}$$

Then using equations 3.32 and 3.33, θ_5 can be computed as,

$$\theta_5 = \text{atan}_2(\sigma_5\sqrt{1 - {C_{33}^*}^2}, C_{33}^*) \tag{A.34}$$

Here, the change in sign of σ_5 causes flipping the wrist of the manipulator [46]. Now remaining variables can be determined by using the θ_5 as,

$$\cos\theta_4\sin\theta_5 = C_{13}^* \tag{A.35a}$$
$$\sin\theta_4\sin\theta_5 = C_{23}^* \tag{A.35b}$$

If $\sin\theta_5 \neq 0$, then,

$$\theta_4 = \mathrm{atan}_2(C_{23}^*, C_{13}^*) \tag{A.36}$$

In order to determine the last joint variable, again θ_5 is used as,

$$\sin\theta_6 \sin\theta_5 = C_{32}^* \tag{A.37a}$$
$$\cos\theta_6 \sin\theta_5 = -C_{31}^* \tag{A.37b}$$

Again, if $\sin\theta_5 \neq 0$, then,

$$\theta_6 = \mathrm{atan}_2(C_{32}^*, -C_{31}^*) \tag{A.38}$$

As seen in the above equations, two of the joint variables, both θ_4 and θ_6 are determined using the value of θ_5. This makes the value of the θ_5 very important in the calculation of the joint variables of the spherical wrist. If *sine* of θ_5 becomes zero, second singularity occurs, and $\vec{u}_3^{(3)}$ and $\vec{u}_3^{(5)}$ become parallel. Then calculation of θ_4 and θ_6 becomes impossible, and θ_4 and θ_6 cannot be found separately which is illustrated in the Figure A.3.
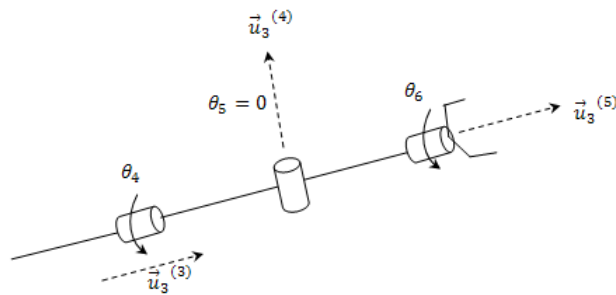
Figure A.3: Illustration of Second Singularity

APPENDIX B

CASE STUDIES FOR KINEMATIC EQUATIONS

B.1. CASE STUDY 1 FOR KINEMATIC EQUATIONS

The link lengths, link offsets and joint variables are given below; the model shows the manipulator as in the Figure B.1.

$a_2 = 0.5m, d_2 = 0, d_4 = 0.4m, d_6 = 0.3m,$

$\theta_1 = 45, \theta_2 = -60, \theta_3 = 50, \theta_4 = 60, \theta_5 = 45, \theta_6 = 120.$

Computed position and orientation matrix are put into transformation matrix form,

```
TRANSFORMATION_MATRIX =
    -0.77847     0.5649     -0.27363     0.12766
    -0.59911    -0.53865     0.59239     0.12766
     0.18725     0.62509     0.75776     0.82694
        0           0           0           1
```

Figure B.1: Transformation Matrix Obtained from MATLAB

The position and orientation is shown in the Figure B.2Figure B. where frame 1 is shown to demonstrate the change of angle θ_1 with respect to base frame attached to the left side of the figure.
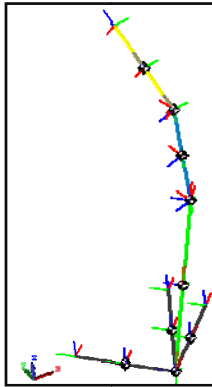
Figure B.2: Illustration of 6R for Given Parameters of Case Study – 1

The MATLAB program gives the joint variables using inverse kinematics as,

```
INVKIN =
        45        -60        50        60        45       120
```

Figure B.3: Inverse Kinematics Results from MATLAB

```
GIVEN_THETAS =
    45   -60   50   60   45   120
TRANSFORMATION_MATRIX =
    -0.77847      0.5649     -0.27363     0.12766
    -0.59911     -0.53865     0.59239     0.12766
     0.18725      0.62509     0.75776     0.82694
          0            0            0            1
INVKIN =
         45         -60          50          60          45         120
ORIENTATION_OF_WRIST =
    -0.77847      0.5649     -0.27363
    -0.59911     -0.53865     0.59239
     0.18725      0.62509     0.75776
>> ORIENT_FROM_SIMMECHANICS=[ORT6(1,2:4);ORT6(1,5:7);ORT6(1,8:10)]'
ORIENT_FROM_SIMMECHANICS =
    -0.77847      0.5649     -0.27363
    -0.59911     -0.53865     0.59239
     0.18725      0.62509     0.75776
>> WRIST_POSITION
WRIST_POSITION =
     0.12766
     0.12766
     0.82694
>> WRIST_POSITION_FROM_SIMMECHANICS=[POS_5_X(1,2);POS_5_Y(1,2);POS_5_Z(1,2)]
WRIST_POSITION_FROM_SIMMECHANICS =
     0.12766
     0.12766
     0.82694
>> TIP_POSITION=R+d6*CEX*u3
TIP_POSITION =
     0.045571
     0.30538
     1.0543
>> TIP_POSITION_FROM_SIMMECHANICS=[POS_6_X(1,2);POS_6_Y(1,2);POS_6_Z(1,2)]
TIP_POSITION_FROM_SIMMECHANICS =
     0.045571
     0.30538
     1.0543
```

Figure B.4: Output of the Kinematic Equations from MATLAB

145

All outputs of the MATLAB program are put together and shown in the Figure B.4. First, the given joint variables are displayed and the position and orientation of the manipulator are computed. The computed matrices are put into inverse kinematic equations and the given joint variables are acquired. Then orientation of the wrist point is calculated using the equation A.3 and compared with the one found using SimMechanics model and both are the same. This process is done for the position of the wrist point and thus, forward kinematic equations are verified. After that, the tip point is calculated using the equation A.10 and compared with the one taken from SimMechanics model. The results indicate that tip point can be calculated algebraically.

B.2. CASE STUDY 2 FOR KINEMATIC EQUATIONS

In this case study, error at the first singularity is performed using MATLAB program. Recall that from inverse kinematics section, if the lengths of the "a_2" and "d_4" is equal, then, when the value of the θ_3 reaches to $-\pi\backslash 2$, the θ_2 angle becomes arbitrary. In order to avoid this singularity a protection code is embedded into the MATLAB program. If the link lengths, link offsets and joint variables are taken as given below, the program gives an output as in the Figure B.5.

$$a_2 = 0.5m, d_2 = 0, d_4 = 0.5m, d_6 = 0.3m,$$
$$\theta_1 = 70, \theta_2 = -30, \theta_3 = -90, \theta_4 = 35, \theta_5 = 45, \theta_6 = 20.$$


```
a2 =
        0.5
d2 =
      0
d4 =
        0.5
d6 =
        0.3
GIVEN_THETAS =
    70    -30    -90    35    45    20
TRANSFORMATION_MATRIX =
    -0.48413    -0.53856    -0.68962         0
     0.60335     0.36533    -0.70887         0
     0.63371    -0.75926     0.14807   8.3267e-017
         0           0           0         1
??? Error using ==> PUMAInvKin at 74
The Determinat 2 is zero!!! First Singularity!!!
```

Figure B.5: Demonstration of the First Singularity

146

B.3. CASE STUDY 3 FOR KINEMATIC EQUATIONS

In this case study, error at the second singularity is performed using MATLAB program. Again recall from the inverse kinematics section that computation of the "θ_4" and "θ_6" is depend on the value of the "θ_5". If the value of the θ_5 becomes "0" or "$\pm\pi$, then "θ_4" and "θ_6" cannot be calculated separately. If the link lengths, link offsets and joint variables are taken as given below, the program gives an output as in the Figure B.6.

$a_2 = 0.5m, d_2 = 0, d_4 = 0.4m, d_6 = 0.3m,$

$\theta_1 = 70, \theta_2 = -30, \theta_3 = 95, \theta_4 = 35, \theta_5 = 0, \theta_6 = 20.$

```
a2 =
        0.5
d2 =
      0
d4 =
        0.4
d6 =
        0.3
GIVEN_THETAS =
    70    -30     90     35      0     20
TRANSFORMATION_MATRIX =
      -0.67166      -0.67907      0.2962      0.26658
       0.54966      -0.1887       0.8138      0.73242
      -0.49673       0.70941      0.5         0.45
             0             0      0           1
??? Error using ==> PUMAInvKin at 151
Second Singularity No 1!!!
```

Figure B.6: Demonstration of the Second Singularity

APPENDIX C

DYNAMIC EQUATIONS

C.1.ORIENTATION OF THE LINKS

Before starting to recursive kinematic formulation, the orientation matrices have to be determined to be able to be used in the derivation of the velocities and accelerations. In the recursive formulation, the equations start form the base of the manipulator and proceed until the last link. While moving from one link to other, reference frames attached to the joints have to be transferred using the appropriate orientation matrix. The orientation matrices derived at the forward kinematic section at the Appendix A (equation A.5) are used in the recursive formulation as,

$$\widehat{\Phi}_i = \widehat{\Phi}_{i-1} e^{\tilde{u}_3 \theta_i} e^{\tilde{u}_1 \alpha_i} \tag{C.1}$$

where $\widehat{\Phi}_0 = \hat{I}$ for $i = 1,2,\dots,n$. Here and at the following equations, "n" denotes the number of the joints

C.2.ANGULAR VELOCITIES OF THE LINKS

In order to reach the acceleration for the calculation of the forces, first, the velocities of the links have to be determined.
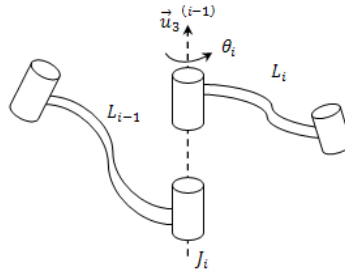
Figure C.1: Illustration of Angular Velocities of the Links

Here, in the Figure C.1, the angular velocity of the joint (i) is calculated using $\dot{\theta}$ which describes the direction and the speed of the rotation. The orientation matrix is taken from the equation C.1 and the angular velocity of the link is computed as,

$$\bar{\omega}_i = \bar{\omega}_{i-1} + \dot{\theta}_i \widehat{\Phi}_{i-1} \bar{u}_3 \tag{C.2}$$

for $i = 1,2,\dots,n$ where $\bar{\omega}_0 = 0$.

C.3. ANGULAR ACCELERATIONS OF THE LINKS

The angular acceleration of the links can easily be computed by taking the time derivate of the angular velocity of the links as,

$$\vec{\alpha}_i = d_0 \vec{\omega}/dt \tag{C.3}$$
$$\bar{\alpha}_i = \bar{\alpha}_{i-1} + \left(\ddot{\theta}_i \hat{I} + \dot{\theta}_i \widetilde{\omega}_{i-1} \right) \widehat{\Phi}_{i-1} \bar{u}_3 \tag{C.4}$$

for $i = 1,2,\dots,n$ where $\bar{\alpha}_0 = 0$.

C.4. POSITIONS OF THE LINK ORIGINS

The position of the link origin has to be determined to calculate the velocities of the link origins.
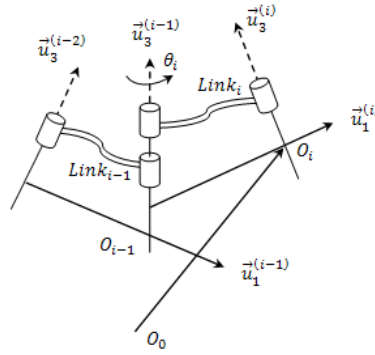
Figure C.2: Illustration of the Positions of the Link Origins

Here, in the Figure C.2, the position of the link origin is computed with respect to the inertial frame because differentiation of the vectors in the inertial frame is easier. The position of the link origin can be calculated as,

$$\bar{P}_i = \bar{P}_{i-1} + d_i \widehat{\Phi}_{i-1} \bar{u}_3 + a_i \widehat{\Phi}_i \bar{u}_1 \qquad (C.5)$$

for $i = 1,2, \dots , n$ where $\bar{P}_0 = 0$.

C.5. MASS CENTER POSITIONS OF THE LINKS

The mass center position is used to calculate the velocity and acceleration of the mass center.
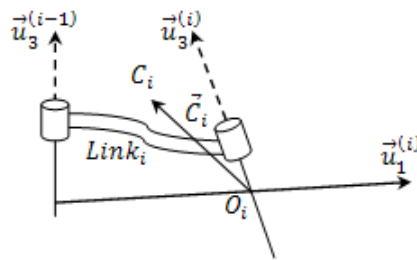
Figure C.3: Illustration of the Mass Center Position of the Links

Again, the position of the mass center is taken with respect to the base coordinates as in the position of the link origins. Here, in the Figure C.3, "$\vec{C}_i$" represents the position of the center of mass from the link's origin. For a rigid link, "$\vec{C}_i$" is constant and in the computations it is taken as the half of the link lengths. The position of center of mass is computed as,

$$\bar{P}_{ci} = \bar{P}_i + \widehat{\Phi}_i \bar{C}_i \tag{C.6}$$

for $i = 1, 2, \dots, n$.

C.6. VELOCITIES OF THE LINK ORIGINS

The linear velocity of the link origins can be easily computed by taking the time derivate of the position of the link origins as,

$$\vec{V}_i = d_0 \vec{P}_i / dt \tag{C.7}$$
$$\bar{V}_i = \bar{V}_{i-1} + a_i \widetilde{\omega}_i \widehat{\Phi}_i \bar{u}_1 + d_i \widetilde{\omega}_{i-1} \widehat{\Phi}_{i-1} \bar{u}_3 \tag{C.8}$$

for $i = 1, 2, \dots, n$ where $\bar{V}_0 = \bar{0}$.

C.7. ACCELERATIONS OF THE LINK ORIGINS

The linear acceleration of the link origins is obtained by taking the time derivate of the velocity of the link origins. Here, "a_i" represents the link length from D-H convention and "$\bar{a}_i$" represents the linear acceleration of the link origin in matrix form. The calculation is given in equation C.10 as,

$$\vec{a}_i = d_0 \vec{V}_i / dt \tag{C.9}$$
$$\bar{a}_i = \bar{a}_{i-1} + a_i(\widetilde{\alpha}_i + \widetilde{\omega}_i^2)\widehat{\Phi}_i \bar{u}_1 + d_i(\widetilde{\alpha}_{i-1} + \widetilde{\omega}_{i-1}^2)\widehat{\Phi}_{i-1}\bar{u}_3 \tag{C.10}$$

for $i = 1, 2, \dots, n$ where $\bar{a}_0 = \bar{0}$.

C.8.VELOCITIES OF THE MASS CENTERS

Using the equation C.10 and the "$\vec{C}_i$" mentioned at the mass center position of the links section, the velocities of the mass centers can be computed as,

$$\bar{V}_{ci} = \bar{V}_i + \widetilde{\omega}\widehat{\Phi}_i\bar{C}_i \tag{C.11}$$

for $i = 1,2, \dots ,n$.

C.9.ACCELERATIONS OF THE MASS CENTERS

Most of the calculations done up to now is to find the accelerations of the mass center which are used to calculate the inertial forces and moments acting on the links.

$$\bar{a}_{ci} = \bar{a}_i + (\widetilde{\alpha}_i + \widetilde{\omega}_i^2)\widehat{\Phi}_i\bar{C}_i \tag{C.12}$$

for $i = 1,2, \dots ,n$.

APPENDIX D

TECHNICAL DRAWINGS

D.1.TECHNICAL DRAWINGS OF FMB

Middle East Technical University Mechanical Eng. Dept.		
Part Name: First Mechanical Brake	Size: A4	
Designer	DWG No: Part 1	
Serter YILMAZ		
Approved	Mat:	
İlhan KONUKSEVEN	Mixed	

1 - Lever Arm
2 - Arm Connector
3 - Outer Cap
4 - "V" Shape
5 - Spring
6 - Braking Pads
7 - User Side Conical Surface
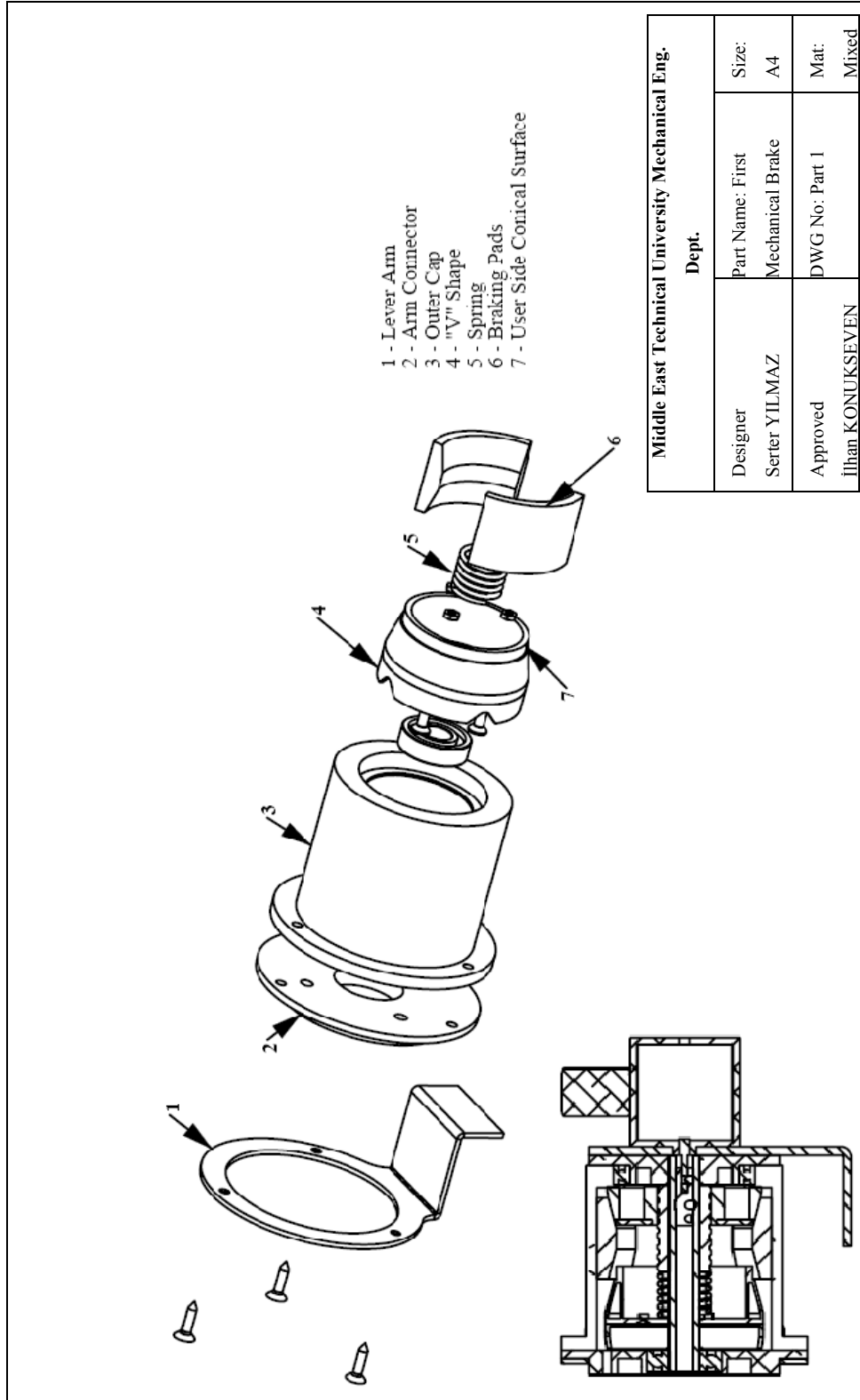
Figure D.1: Exploded View of FMB, Part 1

154

1 - Linear Sliders
2 - Shaft
3 - Pins
4 - DC Motor
5 - Ground Fixer
6 - Motor Side Fixer
7 - Coupling
8 - Power Screw
9 - Motor Side
    Conical Surface

Middle East Technical University Mechanical Eng. Dept.		
Part Name: First		Size:
Mechanical Brake		A4
Designer	DWG No: Part 2	Mat:
Serter YILMAZ		Mixed
Approved		
İlhan KONUKSEVEN		
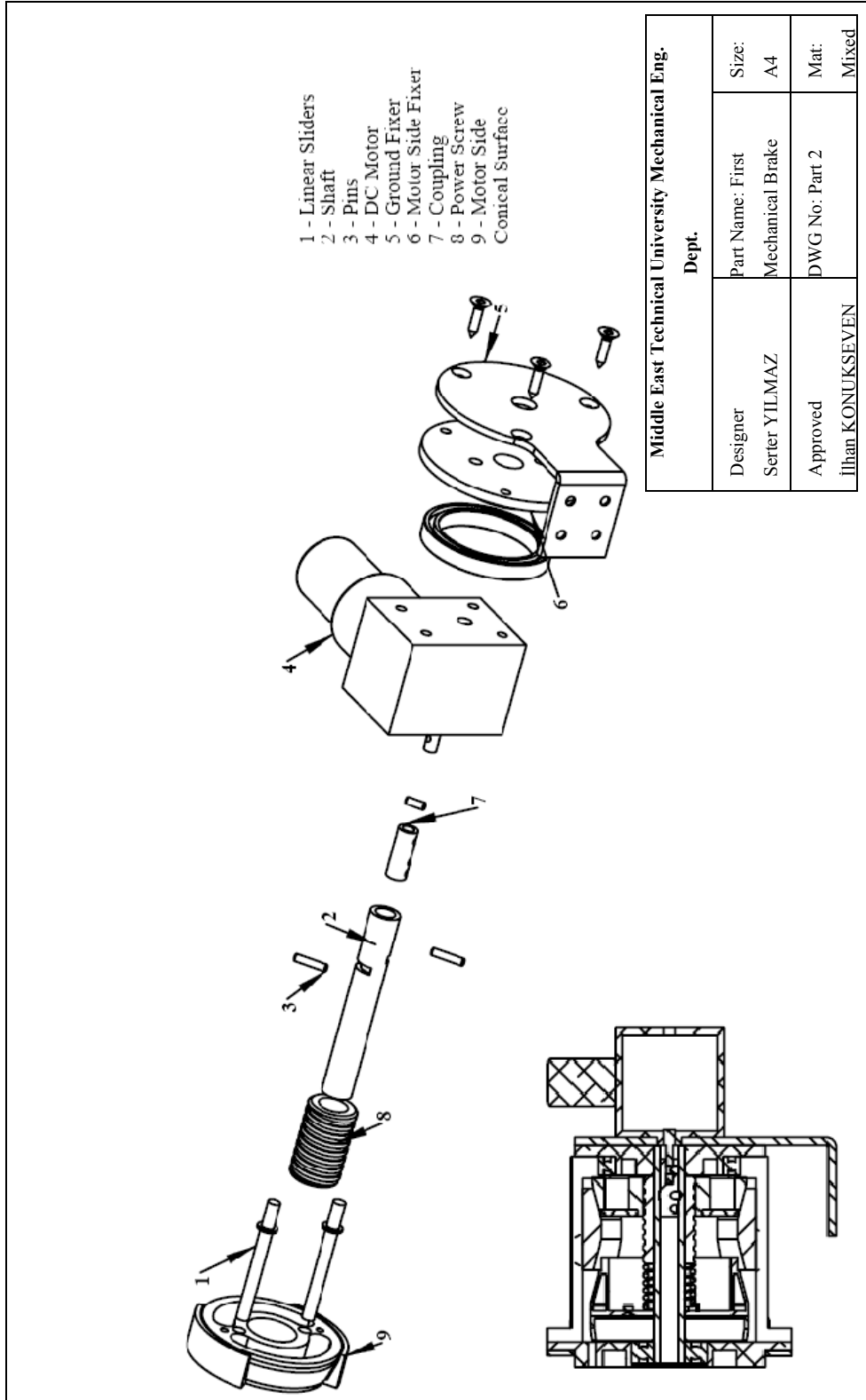
Figure D.2: Exploded View of FMB, Part 2

155

D.2.TECHNICAL DRAWINGS OF SMB

1 - Big Washer
2 - Ring for User Side
3 - Potentiometer Holder
4 - Potentiometer
  Connector

Middle East Technical University Mechanical Eng. Dept.		Size:
	Part Name: Second Mechanical Brake	A4
Designer		Mat:
Serter YILMAZ	DWG No: Part 1	Mixed
Approved		
İlhan KONUKSEVEN		
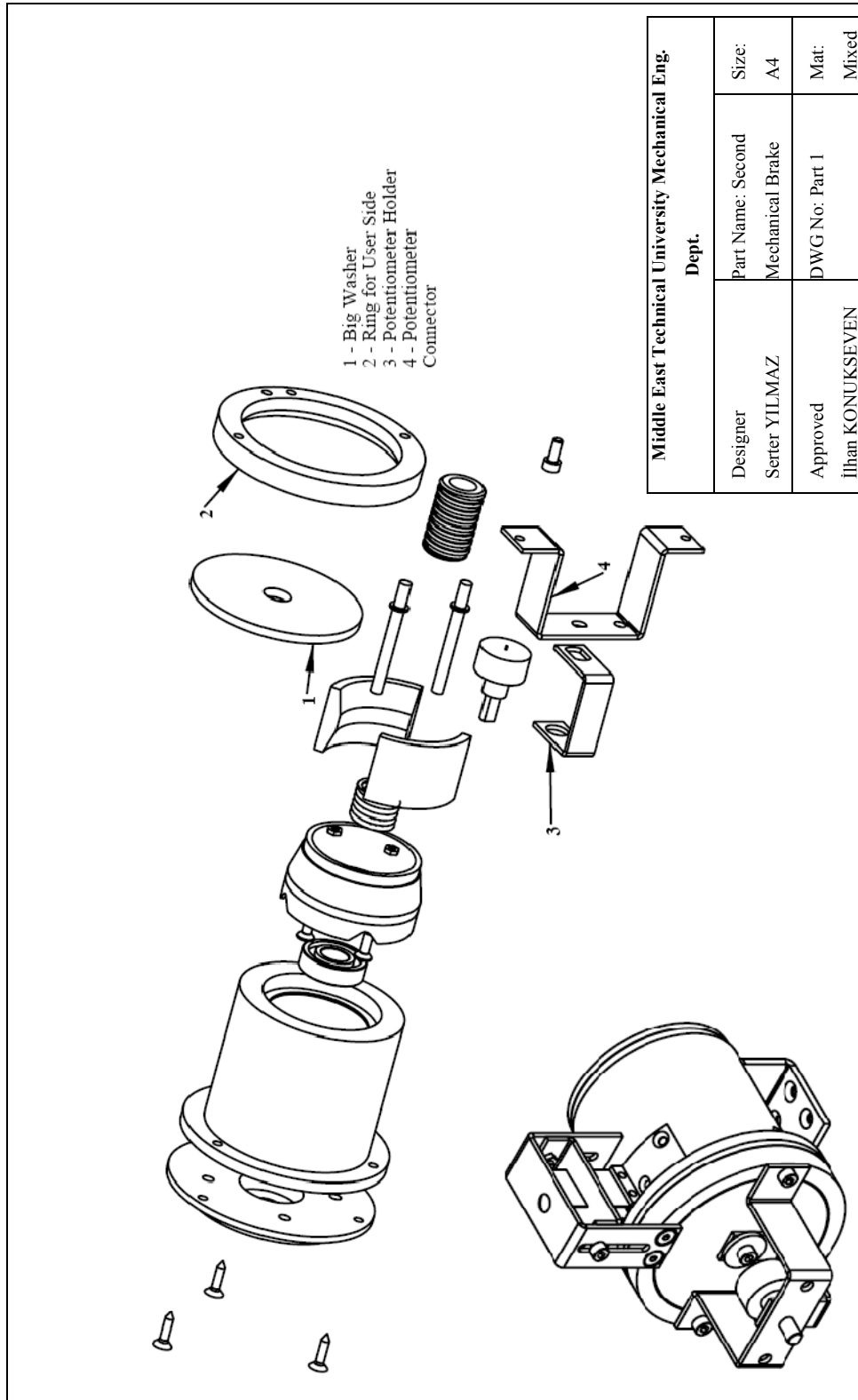
Figure D.3: Exploded View of SMB, Part 1

1 - Leaf Spring Arm Connector
2 - Leaf Spring Stiffness Adjuster
3 - Leaf Spring
4 - Leaf Spring Outer Cap
Connector
5 - Shaft Extender

Middle East Technical University Mechanical Eng. Dept.		
Designer	Part Name: Second	Size:
Serter YILMAZ	Mechanical Brake	A4
Approved	DWG No: Part 2	Mat:
İlhan KONUKSEVEN		Mixed
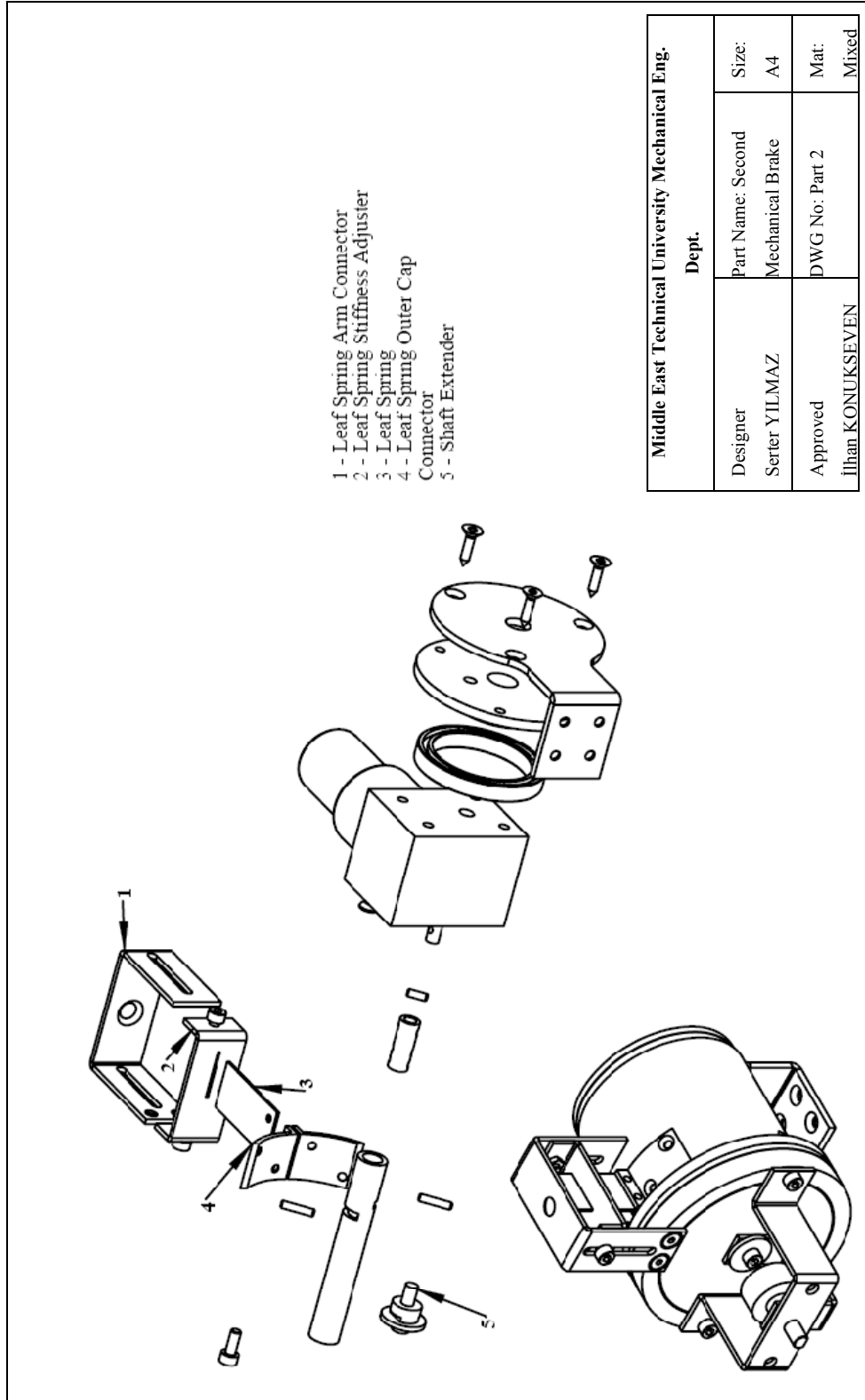
Figure D.4: Exploded View of SMB, Part 2

157

D.3.TECHNICAL DRAWINGS OF DMB

1 - Potentiometer
2 - Potentiometer Connector
3 - Potentiometer Extender
4 - Braking Pads
5 - Linear Sliders
6 - Motor Side Conical Surface
7 - The Outer Cap
8 - Ring
9 - Washer
10 - Potentiometer Holder Extender
11 - Potentiometer Holder

Middle East Technical University Mechanical Eng. Dept.		
	Part Name: Developed Mechanical Brake	Size: A4
Designer Serter YILMAZ	DWG No: Part 1	Mat: Mixed
Approved İlhan KONUKSEVEN		

Figure D.5: Exploded View of DMB, Part 1

Middle East Technical University Mechanical Eng. Dept.		Size:
	Part Name: Developed Mechanical Brake	A4
Designer Serter YILMAZ		Mat:
Approved İlhan KONUKSEVEN	DWG No: Part 2	Mixed

1 - Leaf Spring
2 - Leaf Spring Arm Connector
3 - Motor Side Fixer
4 - Ground Fixer
5 - Motor Holder
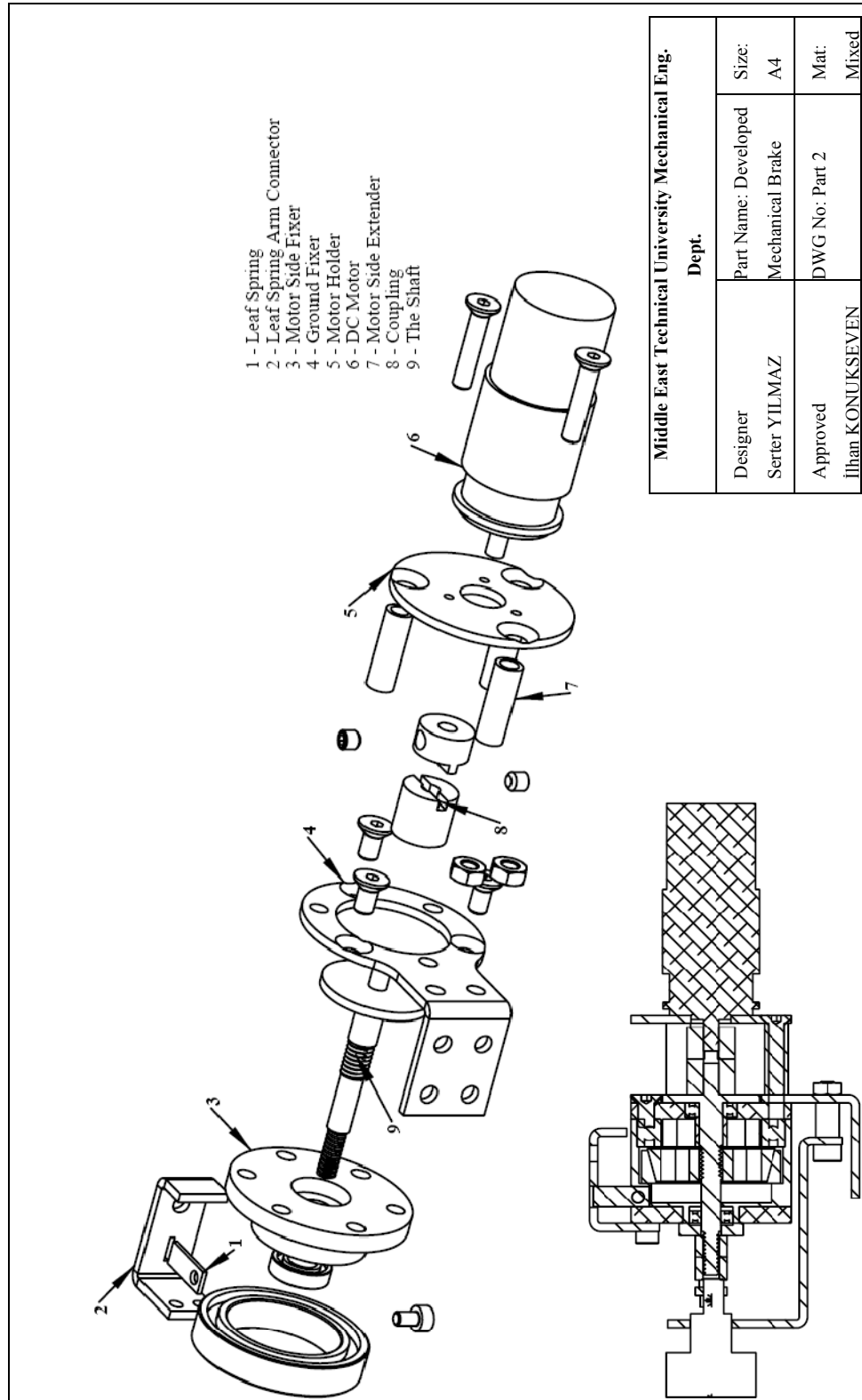6 - DC Motor
7 - Motor Side Extender
8 - Coupling
9 - The Shaft

Figure D.6: Exploded View of DMB, Part 2